

**ADMITTANCE AND IMPEDANCE HAPTIC CONTROL FOR
REALIZATION OF DIGITAL CLAY AS AN EFFECTIVE HUMAN
MACHINE INTERFACE (HMI) DEVICE**

A Thesis
Presented to
The Academic Faculty

by

Cheng Shu Ngoo

In Partial Fulfillment
of the Requirements for the Degree
Master of Science in the
George W. Woodruff School of Mechanical Engineering

Georgia Institute of Technology
December 2009

**ADMITTANCE AND IMPEDANCE HAPTIC CONTROL FOR
REALIZATION OF DIGITAL CLAY AS AN EFFECTIVE HUMAN
MACHINE INTERFACE (HMI) DEVICE**

Approved by:

Dr. Wayne J. Book, Advisor
School of Mechanical Engineering
Georgia Institute of Technology

Dr. Nader Sadegh
School of Mechanical Engineering
Georgia Institute of Technology

Dr. Ari Glezer
School of Mechanical Engineering
Georgia Institute of Technology

Date Approved: November 12, 2009

to princess Danielle,
“AMOR EST VITAE ESSENTIA”

ACKNOWLEDGEMENTS

I would like to first and foremost acknowledge and express my utmost gratitude to Dr. Wayne Book, my advisor for supporting me and giving me the opportunity to work on this project, which opened so many doors in my life as a student and as a person. His invaluable insights are my guiding light when countless research hours seemed fruitless and heading in the drain. I will also always remember the many inspirational conversations that we had. I am indebted to Dr. Haihong Zhu, the designer of the current Digital Clay prototype, for his assistance and suggestions even though he is always on the go. I would like to thank my thesis reading committee members Dr. Ari Glezer and Dr. Nader Sadeh for taking time off their busy schedules to review and provide feedback on my work. Also, a great many thanks to JD Huggins for his advice and helping hand when I needed it most.

I would like to thank all my family members who, though are far in distance but are always close to my heart. A great many thanks also to my roommates Mugi and Vik for keeping me in check and giving me their friendships. Also, to the new and old members of the Intelligent Machine Dynamics Lab (IMDL) at Georgia Tech; Aaron, Longke, Mark, Ryder, Heather, Brian, Hannes, and Ta, thank you all for being my friends and great resources when I needed it.

TABLE OF CONTENTS

| | Page |
|---|------|
| ACKNOWLEDGEMENTS | iv |
| LIST OF TABLES | viii |
| LIST OF FIGURES | ix |
| SUMMARY | xv |
| CHAPTER 1 INTRODUCTION | 1 |
| 1.1 Current 5x5 Digital Clay Prototype System Overview | 2 |
| 1.1.1 Fluid Driving System | 3 |
| 1.1.2 Actuator with Embedded Displacement Sensor | 7 |
| 1.1.3 Control Scheme | 9 |
| 1.1.4 Control Hardware | 11 |
| 1.2 Digital Clay as an Efficient Haptic HMI Device | 13 |
| 1.3 Objective and Scope of Research | 15 |
| CHAPTER 2 BACKGROUND AND LITERATURE REVIEW | 16 |
| 2.1 Importance of Shape Display and Applications in Virtual Reality | 16 |
| 2.2 Available Research on Haptic Devices, Tactile Stimulation, and Pin Array | 18 |
| 2.2.1 Force Feedback Haptic Devices | 19 |
| 2.2.2 Planar Array Tactile Devices | 22 |
| 2.2.3 Haptic Devices Combining Tactile and Force Feedback | 24 |
| CHAPTER 3 DIGITAL CLAY DISPLACEMENT AND VELOCITY CONTROL | 28 |
| 3.1 5x5 Prototype Actuator Array Locations and Naming Convention | 28 |
| 3.2 Displacement Sensor Accuracy and Repeatability Evaluation | 29 |
| 3.3 Obtaining Velocity from Displacement Measurements | 30 |
| 3.3.1 Finite Difference Approximation | 30 |
| 3.3.2 Alpha-Beta-Gamma Filtering | 33 |

| | | |
|---|---|-----|
| 3.3.3 | Low Velocity and Low Acceleration Estimator (LAE) | 35 |
| 3.4 | Digital Clay Actuator Displacement and Velocity Tracking Controller | 38 |
| 3.5 | Remarks and Discussion | 43 |
| CHAPTER 4 DIGITAL CLAY SINGLE ACTUATOR SYSTEM MODELING AND SIMULATION | | 44 |
| 4.1 | Digital Clay as an Electro-Hydraulic System | 45 |
| 4.2 | Frequency Response of a Single Actuator | 47 |
| 4.3 | Model of Digital Clay Single Actuator from Mathematical Equations | 49 |
| 4.4 | Remarks and Discussion | 65 |
| CHAPTER 5 MODEL BASED FORCE ESTIMATION | | 66 |
| 5.1 | Previous Work on Sensorless Force Estimation | 68 |
| 5.2 | Open Loop Force Estimation | 72 |
| 5.3 | Proportional Integral Observer | 76 |
| 5.3.1 | Design Procedure | 80 |
| 5.3.2 | Continuous Time Simulation of PIO | 83 |
| 5.3.3 | Discretization of PIO | 86 |
| 5.4 | Disturbance Observer | 95 |
| 5.5 | Implementation of Discrete-time Observer on Digital Controller | 102 |
| 5.6 | Remarks and Discussion | 105 |
| CHAPTER 6 SOURCE PRESSURE CONTROL BY FLOW CONTROL | | 107 |
| 6.1 | Two-valve Hydraulic Pressure Regulation/Control System | 108 |
| 6.1.1 | Derivation of System Equations | 109 |
| 6.1.2 | Simulation of Pressure Control Law | 111 |
| 6.1.3 | Flow-Duty Ratio Study of Inlet/Outlet Valves | 113 |
| 6.1.4 | Micro-miniature Valves for Pressure Control | 118 |
| 6.2 | Pressure Control Law Design | 125 |

| | | |
|--|-------------------------------------|-----|
| 6.3 | Remarks and Discussion | 130 |
| CHAPTER 7 DIGITAL CLAY HAPTIC CONTROL REALIZATION | | 132 |
| 7.1 | Overview of Haptic Modes | 133 |
| 7.1.1 | Admittance Mode Haptics | 133 |
| 7.1.2 | Impedance Mode Haptics | 134 |
| 7.2 | Digital Clay Single Actuator Case | 135 |
| 7.2.1 | Admittance Control | 135 |
| 7.2.2 | Impedance Control | 138 |
| 7.2.3 | Shaping Mode of Digital Clay | 143 |
| 7.3 | Digital Clay 5x5 Array Case | 147 |
| 7.3.1 | Surface Generation Algorithm | 147 |
| 7.3.2 | Hot Area Processor Concept | 151 |
| 7.4 | Remarks and Discussion | 154 |
| CHAPTER 8 CONCLUSIONS AND RECOMMENDATIONS | | 156 |
| 8.1 | Summary and Conclusions | 156 |
| 8.2 | Contributions | 161 |
| 8.3 | Recommendations for Future Research | 162 |
| APPENDIX A: Actuator Velocity vs. Input Duty Ratio | | 164 |
| APPENDIX B: Honeywell ASCX100DN Pressure Sensor Calibration | | 169 |
| APPENDIX C: PCB Electronics 209C12 Force Sensor Data Sheet | | 170 |
| APPENDIX D: TEKSCAN FlexiForce A201 Force Sensor Circuit | | 171 |
| APPENDIX E: TEKSCAN FlexiForce A201 Force Sensor Calibration | | 172 |
| REFERENCES | | 173 |

LIST OF TABLES

| | Page |
|--|------|
| Table 4.1 Single Actuator Experimental Frequency Response Data..... | 48 |
| Table 4.2 Digital Clay Single Actuator Parameters..... | 62 |
| Table 5.1 Average Dynamic Actuator Force Compared to Duty Ratio..... | 73 |

LIST OF FIGURES

| | Page |
|--|------|
| Figure 1.1 Concept of a HMI Moldable Clay: Digital Clay [1]..... | 1 |
| Figure 1.2 Current 5x5 Digital Clay Prototype [1]..... | 2 |
| Figure 1.3 Digital Clay Hydraulic Schematic..... | 3 |
| Figure 1.4 Control Adapter Closed (A) and Opened (B), [1]..... | 5 |
| Figure 1.5 Row Fluid Channel Block [1]..... | 6 |
| Figure 1.6 Column Fluid Channel Block [1]..... | 6 |
| Figure 1.7 Fluid Paths and Control Adapter Location [1]..... | 7 |
| Figure 1.8 Sensor Embedded Actuator Components [1]..... | 7 |
| Figure 1.9 Displacement Sensor Electrical Schematic [1]..... | 8 |
| Figure 1.10 Digital Clay Control Level [1]..... | 9 |
| Figure 1.11 Multiplexing Circuit for Sensor Signals [1]..... | 12 |
| Figure 1.12 Control Valves Spike and Hold Voltage [1]..... | 13 |
| Figure 1.13 Point on a Material Simulation for Digital Clay Single Actuator..... | 13 |
| Figure 2.1 PHANToM 6DOF Haptic Device [12]..... | 20 |
| Figure 2.2 Stiffness Display Device by Liu [14]..... | 20 |
| Figure 2.3 DigiHaptic Device by Casiez [15]..... | 21 |
| Figure 2.4 Touch and Force Display by Yoshikawa [16]..... | 22 |
| Figure 2.5 Dense 400-pin Array Tactile Stimuli by Killebrew [22]..... | 23 |
| Figure 2.6 Various Tactile Devices: Sarakoglu [27] (Left), Kwon [20] (Upper Right), and Wagner [26] (Lower Right)..... | 24 |
| Figure 2.7 TextureExplorer by Ikei and Shiratori [29]..... | 25 |
| Figure 2.8 FEELEX by Iwata [30]..... | 25 |

| | |
|---|----|
| Figure 2.9 Shape Memory Alloy (SMA) Planar Haptic Device by Nakatani [31]..... | 26 |
| Figure 2.10 Digital Clay Testbed 2 by Garth [32]..... | 27 |
| Figure 3.1 Digital Clay Pin Location and Naming Convention..... | 29 |
| Figure 3.2 Comparison between Sensor Data Count and LVDT Displacement Measurement..... | 30 |
| Figure 3.3 Measurement Signal First Derivative Approximation | 32 |
| Figure 3.4 2nd Order Filtered Signal First Derivative Approximation | 32 |
| Figure 3.5 Alpha-Beta-Gamma Filter Prediction of Velocity | 34 |
| Figure 3.6 Low Velocity and Low Acceleration Estimator Block Diagram | 35 |
| Figure 3.7 LAE Estimation of Actuator Velocity..... | 37 |
| Figure 3.8 Actuator Sine Wave Displacement Tracking | 38 |
| Figure 3.9 Actuator Square Wave Displacement Tracking | 39 |
| Figure 3.10 Velocity vs. PWM Duty Ratio Linear Curve Fit for (0,0)..... | 40 |
| Figure 3.11 Square Wave Velocity Tracking with Proportional Feedback ($K_v=0.5$) | 41 |
| Figure 3.12 Square Wave Velocity Tracking with Proportional Feedback ($K_v=1$) | 41 |
| Figure 3.13 Square Wave Velocity Tracking with Proportional Derivative Feedback ($K_v=0.1, K_D=5$) | 42 |
| Figure 4.1 Single Digital Clay Actuator Schematic..... | 46 |
| Figure 4.2 Frequency Response Magnitude Plot of Single Actuator..... | 49 |
| Figure 4.3 Digital Clay Single Actuator and Spring Force Experiment Schematic | 50 |
| Figure 4.4 Flow Rate vs. PWM Duty Ratio Experiment for Solenoid Valve..... | 58 |
| Figure 4.5 MATLAB Simulink Simulation Block Diagram | 59 |
| Figure 4.6 Experimental and Simulated (Initial Parameters) Sine Wave Velocity | 60 |
| Figure 4.7 Experimental and Simulated (Model) Sine Wave Velocity | 61 |
| Figure 4.8 Experimental and Simulated (Model) Sine Wave Displacement Tracking..... | 61 |
| Figure 4.9 Experimental and Simulated (Model) Square Wave Displacement Tracking. | 62 |

| | |
|---|----|
| Figure 5.1 Block Diagram of a Luenberger State Observer | 67 |
| Figure 5.2 Duty Ratio vs. Dynamic Force Experiment | 72 |
| Figure 5.3 Actuator Dynamic Force as a Function of Duty Ratio | 74 |
| Figure 5.4 Static Force Experiment With Respect to Duty Ratio..... | 75 |
| Figure 5.5 Relationship Between Actuator Static Force and Duty Ratio | 75 |
| Figure 5.6 Block Diagram of Plant and Proportional Integral Observer (PIO)..... | 77 |
| Figure 5.7 Continuous Time Simulation of PIO Simulink Block Diagram..... | 84 |
| Figure 5.8 Continuous Model Output with Disturbance and Input Applied..... | 85 |
| Figure 5.9 Comparison of Model and PI Observer Output and Disturbance..... | 85 |
| Figure 5.10 Output and Input from Sine Wave Force Experiment..... | 89 |
| Figure 5.11 Simulink Block Diagram of PIO | 90 |
| Figure 5.12 Comparison between Estimated and Measured Reaction Force (Sine Wave) | 91 |
| Figure 5.13 Output and Input Data from User Interaction 1..... | 92 |
| Figure 5.14 Comparison between Estimated and Measured Force from User Interaction 1 | 92 |
| Figure 5.15 Output and Input Data from User Interaction 2..... | 93 |
| Figure 5.16 Comparison between Estimated and Measured Force from User Interaction 2 | 93 |
| Figure 5.17 Output and Input Data from User Interaction 3..... | 94 |
| Figure 5.18 Comparison between Estimated and Measured Force from User Interaction 3 | 94 |
| Figure 5.19 Inverse Plant Dynamics Disturbance Observer..... | 95 |
| Figure 5.20 Plot of Q Filter with Various Cutoff Frequencies | 97 |
| Figure 5.21 Simulink Block Diagram for Disturbance Observer Simulation..... | 98 |
| Figure 5.22 Disturbance Observer with 100Hz Q Filter. Actual input (solid), filtered input (dots) and estimated input with disturbance (dashed)..... | 98 |

| | |
|---|-----|
| Figure 5.23 Disturbance Observer with 50Hz Q Filter. Actual input (solid), filtered input (dots) and estimated input with disturbance (dashed)..... | 99 |
| Figure 5.24 Disturbance Observer with 30Hz Q Filter. Actual input (solid), filtered input (dots) and estimated input with disturbance (dashed)..... | 99 |
| Figure 5.25 Disturbance Observer with 16Hz Q Filter. Actual input (solid), filtered input (dots) and estimated input with disturbance (dashed)..... | 100 |
| Figure 5.26 Estimated Spring Force Compared to Measured Force..... | 101 |
| Figure 5.27 Estimated User Interaction Force Compared to Measured Force | 102 |
| Figure 6.1 Pressure Source Selection System for Digital Clay | 108 |
| Figure 6.2 Simulink Block Diagram For Pressure Control Simulation..... | 112 |
| Figure 6.3 Simulation of System Pressure (.....) Tracking of a Step Command (—) | 112 |
| Figure 6.4 Simulation of Feedforward and Feedback Duty Cycle Input..... | 113 |
| Figure 6.5 Theoretical Valve Spool Position At Each Cycle..... | 114 |
| Figure 6.6 Flow Rate vs. PWM Duty Ratio for 50Hz Base Frequency..... | 114 |
| Figure 6.7 Flow Rate vs. PWM Duty Ratio for 40Hz Base Frequency..... | 115 |
| Figure 6.8 Flow Rate vs. PWM Duty Ratio for 20Hz Base Frequency..... | 115 |
| Figure 6.9 Line Pressure Spikes when Outlet Valves are pulse-width modulated | 116 |
| Figure 6.10 Line Pressure Spikes when Outlet Valves are pulse-width modulated (zoomed) | 117 |
| Figure 6.11 Actuator Force Subject to Inlet/Outlet Valves Under PWM..... | 118 |
| Figure 6.12 Micro-miniature Valves Placed in Parallel with Source Selection Valves . | 119 |
| Figure 6.13 Micro-miniature Valves in Parallel Acting as a Single Variable Flow Orifice | 120 |
| Figure 6.14 Transistor Switching Circuit for Micro-miniature Valves. Courtesy of LEE Company..... | 121 |
| Figure 6.15 Line Pressure when Micro-miniature Valves Used as Flow Restrictor | 122 |
| Figure 6.16 Bladder Type Pulse Damper (right) courtesy of HIDRACAR S.A. and Simple Air Pulse Damper (left) | 123 |

| | |
|--|-----|
| Figure 6.17 Ten Point Running Average to Smooth Pressure Feedback Signal | 124 |
| Figure 6.18 Line Pressure Build-up Before (Solid) and After (Dashed) Moving Average Filter | 124 |
| Figure 6.19 Closed-loop System Pressure Control with Proportional Feedback..... | 126 |
| Figure 6.20 Closed-loop System Pressure Control with Proportional-Integral Feedback | 127 |
| Figure 6.21 Closed-loop System Pressure Control for Various Desired Pressure (15psi, 18psi, 21psi and 23psi) | 128 |
| Figure 6.22 Closed-loop System Pressure Control for 1Hz Sine Wave Tracking..... | 129 |
| Figure 6.23 Closed Loop Pressure Control with Faster Settling Time but Unstable..... | 129 |
| Figure 6.24 Closed Loop Pressure Control 4Hz Sine Wave Tracking but Unstable..... | 130 |
| Figure 7.1 Admittance Haptic Control Simulation for Virtual Stiffness = 0.015N/mm | 136 |
| Figure 7.2 Admittance Haptic Control Simulation for Virtual Stiffness = 0.06N/mm .. | 137 |
| Figure 7.3 Measured Force on User Finger for both Stiffness Simulations (Zoomed In) | 138 |
| Figure 7.4 Sinusoidal Pressure Tracking Keeping Displacement Constant | 139 |
| Figure 7.5 Impedance Haptic Control for Actuator with Virtual Stiffness of 0.03N/mm (Slow Rate) | 141 |
| Figure 7.6 Impedance Haptic Control for Actuator with Virtual Stiffness of 0.03N/mm (Fast Rate)..... | 142 |
| Figure 7.7 Impedance Haptic Control for Actuator (Filtered Profile) | 143 |
| Figure 7.8 Digital Clay Actuator Shaping Algorithm..... | 144 |
| Figure 7.9 Actuator Displacement and Velocity Stages Before, During and After Shaping Mode | 146 |
| Figure 7.10 Locations of Row and Column Control Valves for Digital Clay Actuators Array | 147 |
| Figure 7.11 Surface Refresh Iteration 1. The first Column Control Valve is opened | 148 |
| Figure 7.12 Surface Refresh Iteration 2. The second Column Control Valve is opened | 149 |
| Figure 7.13 Surface Refresh Iteration 3. The third Column Control Valve is opened ... | 149 |

Figure 7.14 Surface Refresh Iteration 4. The fourth Column Control Valve is opened. 150

Figure 7.15 Last Surface Refresh Iteration. The fifth Column Control Valve is opened 150

Figure 7.16 Hot Area Processing Concept for Digital Clay Surface 152

Figure 7.17 Hot Area Processor in Operation Opening Single Column..... 153

Figure 7.18 Hot Area Processor in Operation Opening Multiple Columns..... 154

SUMMARY

Shape plays an important role in our everyday life to interpret information about the surroundings whether we are aware or not. Together with visual and auditory information, we are able to obtain and process information for different purposes. Output devices such as monitors and speakers convey visual and auditory information while input devices such as touch screen and microphones receive that information for human machine interaction. Such devices have become commonplace but there has yet to be a fitting input/output device utilizing our haptic perception.

Digital Clay is a next generation Human Machine Interface (HMI) device for 2.5D shape input/output via an array of hydraulic actuators. This device potentially has wide applications in the areas of engineering, sciences, medicine, military, entertainment etc. The user can perceive the shape of a computer programmed model in a tangible and concrete manner which means an added realism with the addition of the sense of touch. Conversely, the user can also use Digital Clay as an input device to the computer, by shaping and molding desired shapes on the device, no longer limited to drawing models with a mouse on CAD software.

Shape display has been achieved with the current 5x5 prototype at the Georgia Institute of Technology but this research seeks to expand its capability to include haptic feedback and consequently shaping mode. This thesis gives an overview of the current 5x5 prototype and implements 2 commonly used haptic control methods, the admittance control and the impedance control. For implementing the admittance control, actuator displacement and velocity controllers and a proportional integral observer (PIO) are

designed. The model-based unknown input observer is a solution for force estimation without added sensors in the actuators. For implementing the impedance control, a novel pressure control technique is designed to provide pressure feedback to the actuators array along with accurate and reliable displacement measurement. Both of the haptic control methods are evaluated, hardware and software limitations are outlined and possible future improvements are suggested.

CHAPTER 1 INTRODUCTION

Digital Clay [1] is a fluid-driven actuators array for shape input and output and possibly a haptic human machine interface (HMI) device that has wide potential application in the areas of engineering, sciences, medicine, military, entertainment etc. Haptic refers to the ability to sense the environment; whether actual or virtual, through touch [2]. The name Digital Clay is derived from combining the words “clay” and “digital”. Digital Clay will have the capability of an ordinary sculptor’s clay that can be molded and shaped as desired by the sculptor but at the same time, having the term ‘digital’ expands the device ability to be able to intelligently manipulate and communicate with the sculptor (or user) beyond ordinary clay for example, and by saving the shape as a CAD model. Conversely, Digital Clay could also receive a model from conventional CAD software and displaying a tangible shape and possibly material property simulation for added realism and improving visualization. In the future, the actuators array size could be anywhere from 100x100 to 1000x1000 and completely scalable depending on the resolution demand and application as shown in Figure 1.1.



Figure 1.1 Concept of a HMI Moldable Clay: Digital Clay [1]

However for proof of concept and research purposes, a 5x5 array prototype of this system was conceived, designed and completed in 2007 by Haihong Zhu and currently serves as a Test Bed in the Intelligent Machine Dynamics Laboratory (IMDL) at the Georgia Institute of Technology. Shape display and Editing Mode has been achieved by Zhu. This introduction chapter will present the overview of the current Digital Clay prototype and the objective of this research.

1.1 Current 5x5 Digital Clay Prototype System Overview

The Digital Clay prototype available at the Intelligent Machine Dynamics Laboratory is a hydraulic driven 5x5 array of actuators shown in Figure 1.2. The prototype consists of the following subsystems: hydraulic circuit, actuators with embedded sensor, control hardware and software/ control algorithm.

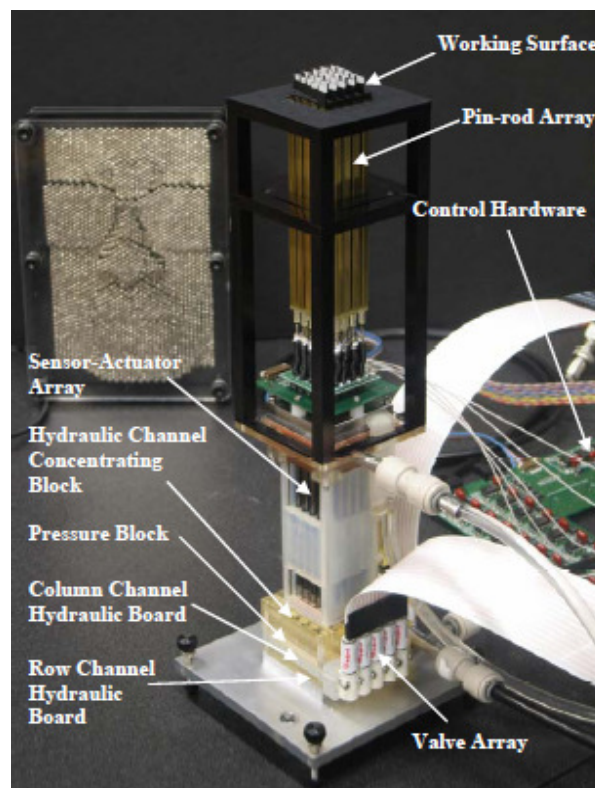


Figure 1.2 Current 5x5 Digital Clay Prototype [1]

1.1.1 Fluid Driving System

The main driving fluid of the system is pressurized *Dow Corning 200* silicon oil and pressurized air. Pressurized silicon oil is used to drive the pin up and down while pressurized air is used for actuation of the control adapter. A novel matrix drive system was developed by Zhu and controls individual pin using only $2 \times n$ valves instead of having $n \times n$ valves for an array having n rows and n columns of actuators [3]. The n -number of solenoid on/off valves actuates the actuators at each row and the n -number of similar valves actuates a control adapter for opening/closing of actuators at each column. A hydraulic schematic circuit of the system is shown in Figure 1.3 below.

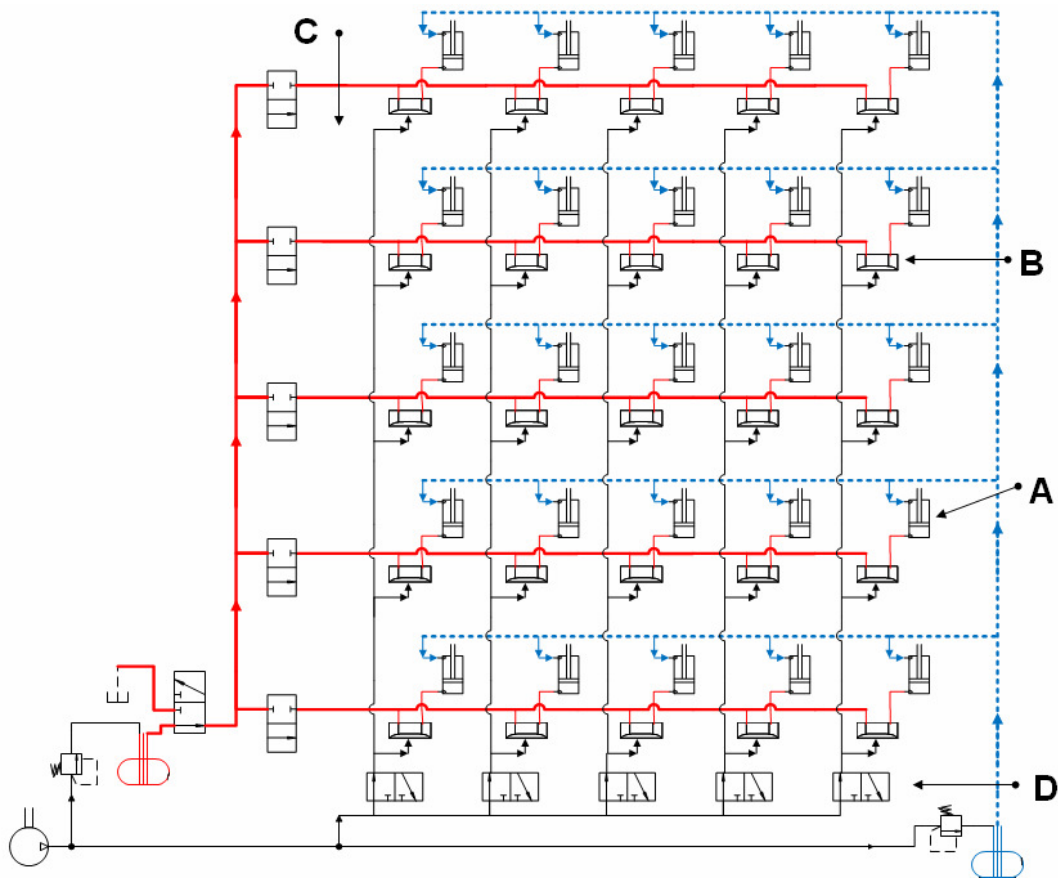


Figure 1.3 Digital Clay Hydraulic Schematic

The air from a main compressed air source is split into two pressure regulators and regulated to supply pressure to the fluid reservoirs and to the control adaptor respectively. The supply silicon oil reservoir is pressurized to 25 psi (Solid lines) while the return reservoir is pressurized to 10 psi (Dashed lines).

Each individual Digital Clay pin is a piston-cylinder hydraulic actuator with embedded displacement sensor. In the figure, there are 25 double acting cylinders (A) that individually have a control adapter (B) and the entire array is controlled by 5 row control valves (C) and 5 column control valves (D). The row control valves are responsible for high/low pressure into actuators while the column control valves are responsible for the column adaptors.

The flow of silicon oil into each row is controlled by miniature solenoid on/off valves by pulse width modulating (PWM) the orifice opening. These miniature valves from *LEE Company* have response time of about 1ms and are only 1.25” in length and 0.9” in diameter and operated by 12V power. There is also a sink associated with the silicon oil line when pin retraction is desired. 2 *Parker Hannifin* pulse valves are connected in parallel and one or the other is activated for selecting high or low pressure source.

A column control adapter (B) opens up path to each individual cylinder to complete the actuation process. The column adapter is driven by compressed air and the flow controlled by turning on and off another set of solenoid valves (D). Note that this line is not regulated and thus has pressure equal to the main compressed air. This pressure is always higher than the driving silicon oil pressure to ensure that sealing of the membrane is tight. From Figure 1.4, compressed air fills the control chamber and provides sealing power to the membrane, blocking the path of silicon fluid from the line to cylinder. When

the pressure of the silicon oil is greater than the pressure in the control chamber, i.e. valve vents compressed air into atmosphere, the silicon oil fills up the working chamber and drives the cylinder. Figure 1.5 shows the row fluid channeling block and Figure 1.6 shows the column channeling block. The two fluid channeling blocks are mated as in Figure 1.7 with a layer of rubber membrane in between that function as the membrane for the control adapter.

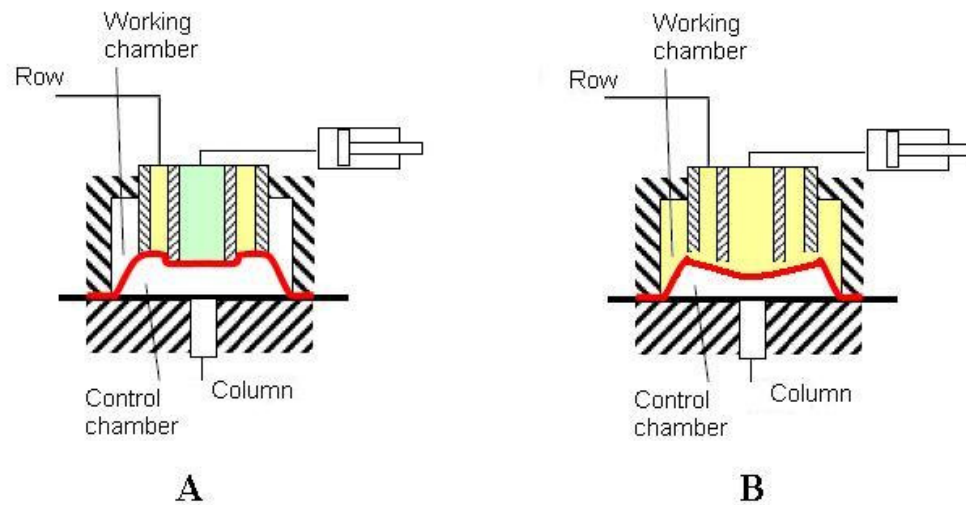


Figure 1.4 Control Adapter Closed (A) and Opened (B), [1]

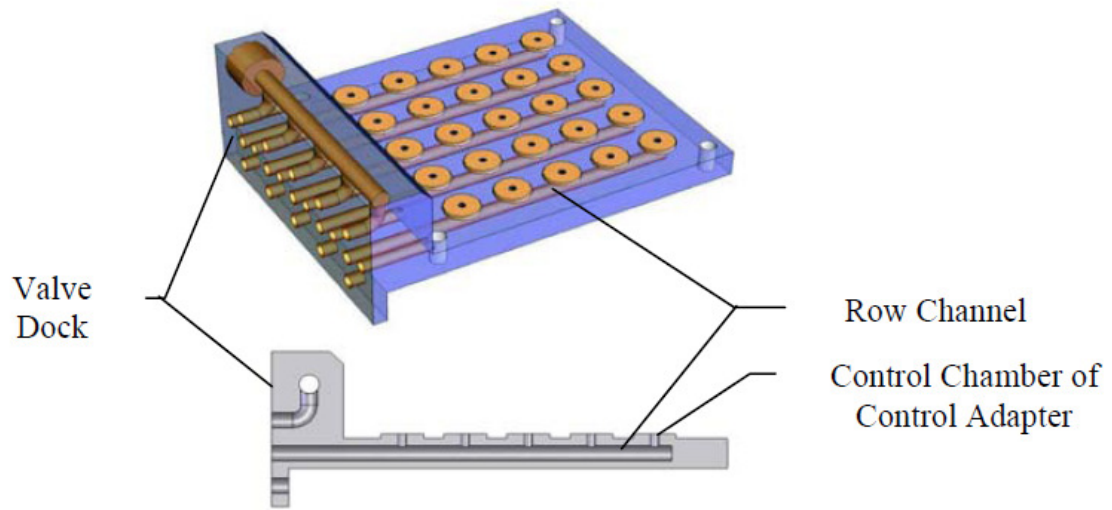


Figure 1.5 Row Fluid Channel Block [1]

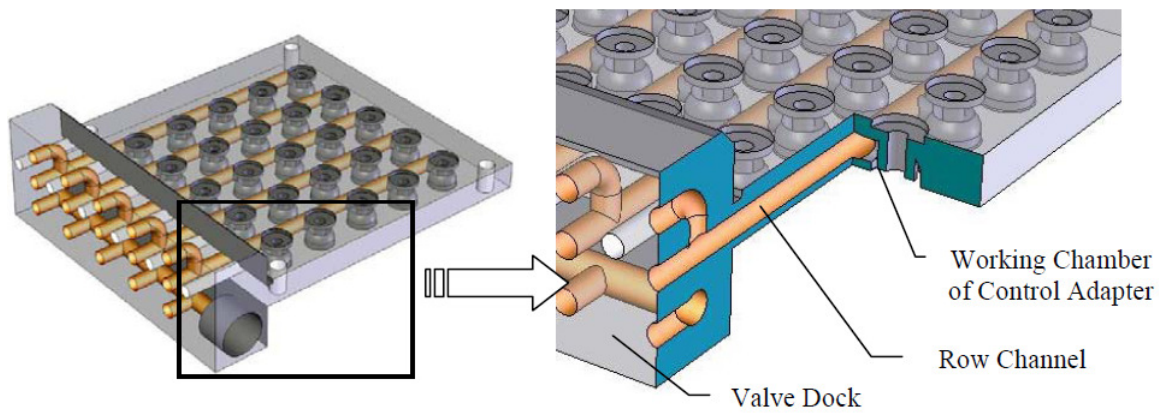


Figure 1.6 Column Fluid Channel Block [1]

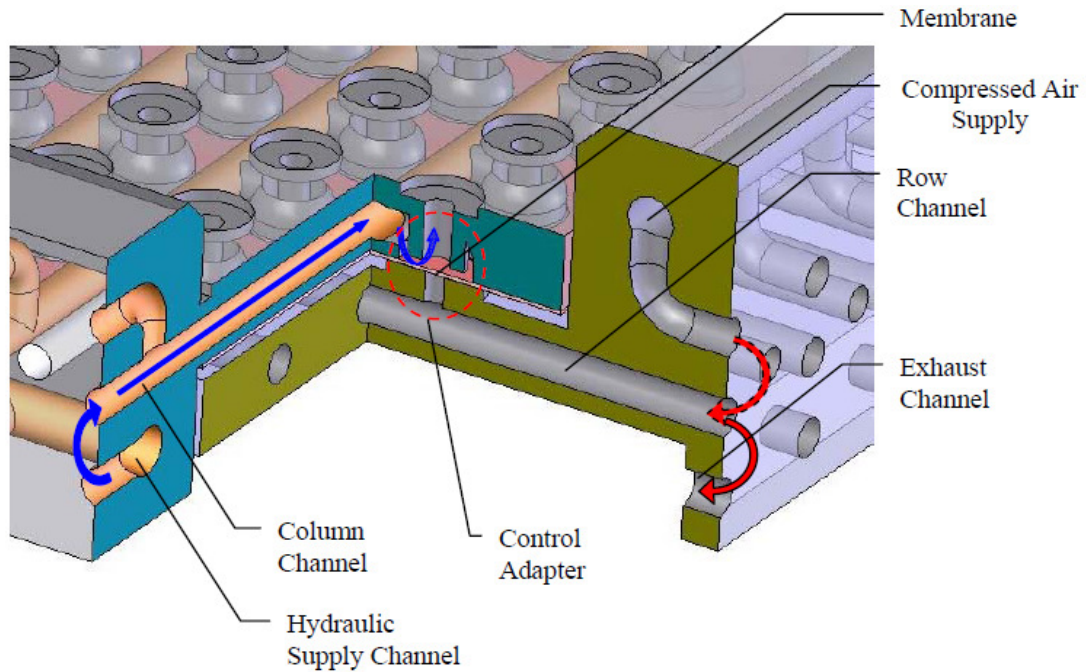


Figure 1.7 Fluid Paths and Control Adapter Location [1]

1.1.2 Actuator with Embedded Displacement Sensor

The displacement sensor for each pin of Digital Clay is embedded in the piston-cylinder configuration for maximum compactness. A capacitively coupled resistive displacement sensor was constructed for individual actuator [4]. Figure 1.8 shows the cross-sectional view of the sensor embedded actuator.

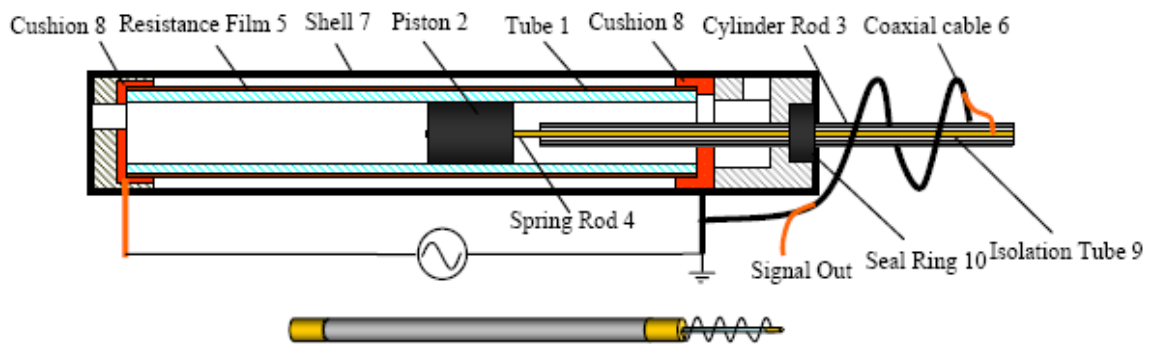


Figure 1.8 Sensor Embedded Actuator Components [1]

The piston (2) is made out of graphite for its excellent electrical conductivity, low friction and sealing capability. A thin aluminum wire acts as a spring rod (4) to reduce friction caused by misalignment while also conducting electricity. An outer stainless steel rod (3) protects the wire and provides rigidity to the piston rod. An isolation tube (9) electrically isolates the wire from its outer protection rod. The cylinder is made from high precision borosilicate glass to reduce friction. A resistive/metal film (5) is deposited on both sides of the outside wall of the glass tube. An electrically conducting cushion (8) connects the two ends of the film to the input. A coaxial cable (6) sends the desired output signal relative to the input signal. Figure 1.9 shows the electrical schematic of the sensor and its working principle.

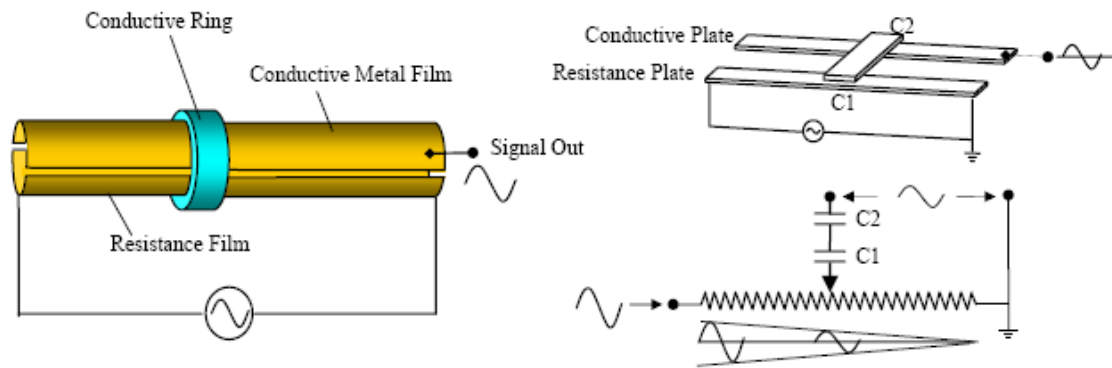


Figure 1.9 Displacement Sensor Electrical Schematic [1]

When an alternating voltage source of around 10 kHz is connected across the resistive film (5), an output signal from the rod (4) that has amplitude proportional to the displacement of the graphite piston (2) can be obtained. This signal amplitude variation with change in displacement is caused by the resistance change as the graphite piston moves along the resistive film. The graphite piston is capacitively connected to the

resistance film. $C1$ is the capacitance between the graphite piston and the resistive film and $C2$ is the capacitance generated in the coaxial cable when shielding the signal. Loosely, think of the working principle of a linear potentiometer.

This sensor embedded actuator has simple structure, negligible space, and high output linearity during operation. This micro-actuator and sensor has ~50mm stroke and has 5mm outer diameter. It can be made even smaller in the future and the possibility of eliminating the dangling coaxial cable would increase robustness, reduce complexity and wear effect.

1.1.3 Control Scheme

For the final product, Digital Clay’s control will be separated into 3 levels: user application programming interface (API), surface level control and cell level control [5].

Figure 1.10 below illustrates the proposed control scheme for Digital Clay.

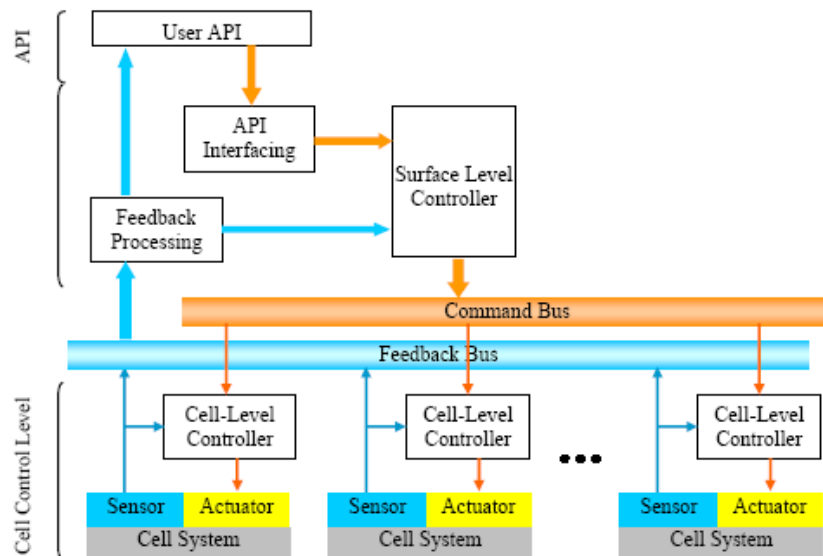


Figure 1.10 Digital Clay Control Level [1]

The API will be the user interface that generates commands to the surface level. For example, any 3D shape that the user inputs will be translated into corresponding surface information for lower level processing. The surface level control will generate command for individual cell level controller. How each cell or pixels interact with each other to produce a surface will be addressed here. Finally, the cell level control will address the displacement sensing and control and for the work to be investigated, force estimation and control of individual actuator. The current control architecture for the 5x5 prototype is only concerned with shape display and the bulk of attention in this thesis will be focused on cell level control and some of surface level control.

The current prototype implements a one-time refresh method [3] for surface generation. For the time being, Real Time Linux (RT Linux) with multi-threading is the operating system for high processing speed. The actuators are controlled to reach desired displacement column by column in one step. First, the matrix of a surface i.e. consisting desired vertical displacement of each actuator generated by surface level controller. The control adaptors of the first column will be open to allow for the cylinders to be actuated. Next the cell-level control takes over and row valves will be pulse width modulated for actuator of each row to reach desired displacement. The control adaptors of this column will be sealed and this surface generation will continue with the next column. This is the simplest surface control method but it will not have the best visual nor haptic effects.

As for the cell-level control, current position control is done with simple proportional control. As the actuators are hydraulic systems and have sufficient damping coefficient, the proportional control gives satisfactory and sufficiently fast settling. The PWM control of row valve has frequency of 100 Hz or 10ms period and duty cycle is limited to 90%

for linear region. Valve dead band is around 10-18% duty cycle depending on supply pressure while saturation and non-linearity is observed at above 90% duty cycle. Control law is updated every 1ms, which is 10 times faster than the PWM frequency. More analysis and improvements of the control will be in subsequent chapters. There is no force control as no pressure sensors are present in the current prototype although Zhu has presented it in [1]. The methodology and implementation of shape editing mode for single actuator was given by Zhu but not yet implemented on the 5x5 array prototype.

1.1.4 Control Hardware

Control hardware of the Digital Clay consists of 12-bit analog-to-digital conversion and multiplexing function for the displacement sensors through a micro-controller unit dsPIC30F4013, a valve spike and hold circuit for each control valve and a main host computer on a Pentium 4 processor which is running on a real time operating system (RT Linux). A Measurement Computing PCI-DAS6402-16 data acquisition card on the host computer is used for digital and analog input/output (I/O) and analog-to-digital conversion functions. A micro-controller unit dsPIC30F6010 is used for interfacing and controlling the valves driver circuit with the host computer data acquisition card.

Due to the large number of signals from the displacement sensors, multiplexing is needed before the signals are sent to the analog to digital (A/D) converter to reduce computational cost [6]. Also due to the high cost and size limitation of signal conditioners for the displacement sensors, multiplexing reduces the number of signal conditioners needed. 5 displacement sensors in the same row share a single signal conditioner. The signal conditioners are needed to convert AC voltage output into useful

DC voltage for feedback control. Details of the construction and components of the multiplexer in Figure 1.11 developed by Zhu will not be discussed in this thesis.

At any instance during sampling, only one signal output in a row is connected to a signal conditioner. The signals from the signal conditioner were then sent to the A/D converter for digital algorithm. For this purpose, a sole microcontroller was utilized and its digital output can be used by the host computer for real time processing. This reduces computational power required from the computer processor.

For the control of the valves, a spike and hold voltage profile as in Figure 1.12 is used. The point of this type of driver is to reduce the time response of the valve. A high voltage 2-4 times the valve rated voltage is applied for a very short time (0.5ms-1ms) and a low voltage half of the rated voltage is applied to hold the valve open until an off command is sent. Zhu managed to reduce the valve open time from 2ms to 0.6ms and valve close time from 2ms to 1ms with a spike and hold method compared to only supplying the max rated voltage for the valves.

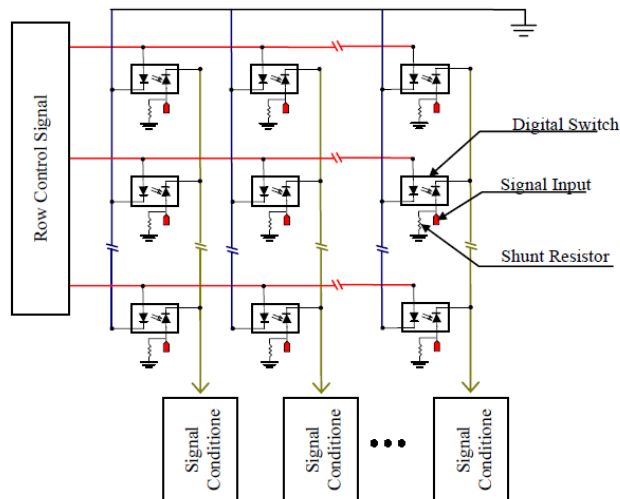


Figure 1.11 Multiplexing Circuit for Sensor Signals [1]

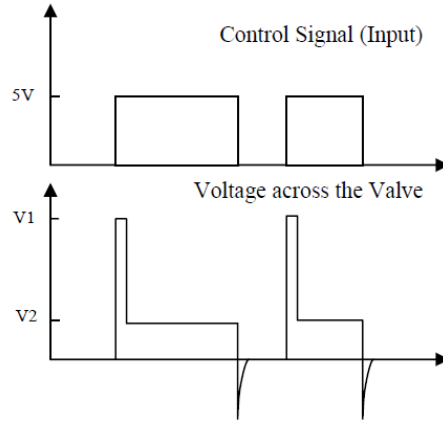


Figure 1.12 Control Valves Spike and Hold Voltage [1]

1.2 Digital Clay as an Efficient Haptic HMI Device

This thesis will aim to realize Digital Clay as an effective haptic device by developing the tools required to implement haptic control. The majority of the work will be focused on a single actuator system case as Digital Clay as a whole is essentially a collection of actuators in an array. Hence, the goal of a single Digital Clay actuator will mimic the behavior of a theoretical point on a material depicted in Figure 1.13.

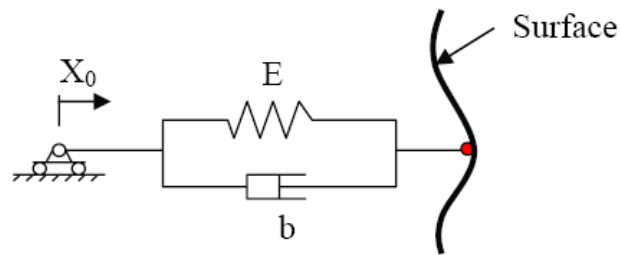


Figure 1.13 Point on a Material Simulation for Digital Clay Single Actuator

From various authors [7][8][9], there are 2 main types of haptic control methods; impedance and admittance. For the impedance haptic control method, the force feedback

from a point on Digital Clay to the user is a function of the displacement from its equilibrium and rate of change of the displacement, proportional to the virtual modulus of elasticity, E and viscous damping, b respectively. The displacement sensor will provide accurate measurement and a velocity estimator needs to be designed. Force/pressure feedback capability needs to be added to Digital Clay. The impedance haptic control law is given by,

$$F_{feedback} = E \cdot (x_0 - x) + b \cdot \dot{x} \quad (1.1)$$

For the admittance haptic control method, the displacement and velocity of Digital Clay is a function of the force applied onto the surface by the user. A force sensing capability needs to be added to Digital Clay. The admittance haptic control law is given by,

$$x_{desired} = x_0 - \frac{F_{applied}}{E} \quad (1.2)$$

$$\dot{x}_{desired} = \text{sgn}(F_{applied}) \cdot \frac{F_{applied}}{b} \quad (1.3)$$

The rate of displacement of Digital Clay surface will depend on the force applied by the user and the direction is dependent on the direction of the force.

1.3 Objective and Scope of Research

This thesis thus aims to realize Digital Clay as an effective haptic device by investigating and implementing the 2 most commonly used haptic control methods; admittance control and impedance control. Here the work of Zhu is extended and several preliminary supporting works are performed to enable implementation of haptic controllers. More specifically, the 2nd chapter will present a background investigation and literature review on past and current technology of haptic devices. The chapter will attempt to highlight the potential that Digital Clay has to be a better haptic device which serves as motivation for the work of this thesis. The 3rd chapter will present a solution to accurately estimate actuators velocity from displacement sensor measurements. Closed loop displacement and velocity controller will be designed to track desired displacement and velocity trajectory. The 4th chapter will present modeling results and simulation of Digital Clay single actuator system which will provide a base for the force observer design in chapter 5. A model based on mathematical formula is derived to design a novel sensorless force estimator. In chapter 5, two model-based unknown input estimation methods known as the proportional integral observer (PIO) and the disturbance observer are used to estimate user force on the actuators. Chapter 6 will present a novel electronic pressure regulation technique based on 2 separate valves to vary Digital Clay system pressure so as to provide haptic sensation to the user as the actuators are pushed. In chapter 7, all the tools and techniques developed in chapters 3 to 6 will be combined to implement the 2 haptic control methods for Digital Clay. A hot area processor is needed to enable surface haptics. Finally conclusions and recommendations for future work will be given in chapter 8.

CHAPTER 2 BACKGROUND AND LITERATURE REVIEW

2.1 Importance of Shape Display and Applications in Virtual Reality

The sense of touch, associated with feeling an object's shape, texture and properties plays an important aspect in everyday life to interpret information about the surroundings whether most people are aware of it or not. The sense of touch might be less apparent to humans compared to vision and hearing; which probably is why its importance is often overlooked. But Robles-De-La-Torre [10] argued, based on evidence in several patients, that having lost the sense of touch, they require more effort and even high possibility of not able to fully re-learn previous motor abilities compared to patients who have lost the sense of sight or hearing. Part of human's 5 major senses, the stimulus to the sense of touch is perceived by the receptors on the skin which fired associated neurons to the brain for processing. Together with visual and auditory information, humans are able to obtain and process information for different purposes. However the sense of touch is crucial for humans to quickly and accurately interact with the environment.

"Virtual Reality is a way for humans to visualize, manipulate and interact with computers and extremely complex data" according to the words of Isdale [11]. Humans visualize the world using the 5 senses by recognizing shapes, colors, textures, sounds, smell, taste etc. and a virtual environment aims to simulate realism concerning the elements of the real world. The user of the virtual environment through a human machine interface (HMI) can manipulate and interact with the objects within the world similar to interactions with the real world.

Available HMI output devices such as monitors and speakers convey visual and auditory information while input devices such as touch screen and microphones receive that information for human and machine interaction. Much focus on virtual environment has been given to such devices and they have become commonplace but there has yet to be a 'standard' or default input/output device utilizing our haptic perception. A haptic interface works by generating intended and controlled mechanical signals to stimulate the human kinesthetic and touch channels and for human to react to the virtual environment [2]. Some of the applications for haptic based HMI include: display of shape, texture, resistance (mechanical impedance) and spatial relationship; exploration of models and experimental data for understanding; training of both rare and common skills; physical retraining/rehabilitation and conditioning; enhancement of motion capabilities in surgery, manufacturing and construction in normal and hazardous environments; entertainment; and communication of emotions. Quoting Hayward, the advancement of moving from a sheet of paper (that is non-programmable) to a computer monitor, that is, being able to program pixel by pixel to display visual information is analogous to moving from a computer mouse (that is non-programmable) to a haptic interface [2]. Some advantages for having a haptic HMI device similar to Digital Clay include:

- Increased accuracy and success rate in remote surgery, palpation and visualization of human organs in Medicine.
- Learning becoming more effective and interesting as students is immersed into virtual learning experience.

- Improved control and visualization for operators during exploration of remote and hazardous environments and handling of hazardous materials by reducing reliance on visual cues.

Robles-De-La-Torre speculates that having a virtual reality interface with focus only on vision and auditory information but with poor haptic display is analogous to the patients having sense of touch impairment. Users of virtual reality and HMI devices would not be able to achieve the highest performance or ‘realism’. Therefore, having a force displaying device is one thing, and being able to accurately and effectively displaying force feedback is another, that presents a challenge in solving mechanical design, actuation, real-time systems, rendering algorithms and sensing problems. If Digital Clay were to be employed as an effective haptic HMI device, its force sensing and feedback capability has to be both effective and accurate to the point of human Just-Noticeable Difference (JND) i.e. the smallest detectable change in force reflected by a haptic device. A haptic device thus must provide a programmable bidirectional exchange of information between the user and the virtual environment [2][9].

2.2 Available Research on Haptic Devices, Tactile Stimulation, and Pin Array

Haptic device has its roots from teleoperation, in a sense that the “slave” part of a master-slave system is computational or virtual as compared to the slave of a teleoperation device which is usually a physical end-effector [2]. Early research on haptic terminology and devices was done by Srinivasan et al [9]. Basically, haptic devices can stimulate and provide two types of information: tactile and kinesthetic. Tactile

information refers to senses from the skin in contact with the environment while kinesthetic information refers to the feeling of forces and positioning of human limbs. The aim of Digital Clay is to provide both classes of information to the user through a tangible surface generation coupled with force feedback. In this subsection, first, force feedback devices will be discussed followed by tactile devices and some devices that attempt to combine both. This summary is by no means an exhaustive list and only provides discussion on available haptics research that the author feels is related to Digital Clay and helpful in directing the readers to see the importance and relevance of this research.

2.2.1 Force Feedback Haptic Devices

One popular and widely-used example of force reflecting haptic devices is the PHANToM by SensAble Technologies in Figure 2.1. This device has between 2 to 6 DOF motions with position sensing and uses cable driven by DC motor to provide force feedback for each axes based on that position feedback [12] [13]. The capstan drive system is used to amplify DC motor torque and able to reduce actuator size. The PHANToM is similar to a haptic stylus and has a point-by-point operation mode. It is capable from 3N and up to 20 N in force feedback depending on the device model and scale. In comparison to the PHANToM, Liu developed a novel stiffness display device that is essentially achieved by varying the length of an elastic beam to try to simulate material property of a virtual object [14]. This device is passive as only dissipation of energy is controlled as opposed to the PHANToM which is an active force feedback device. The schematic of this device is shown in Figure 2.2

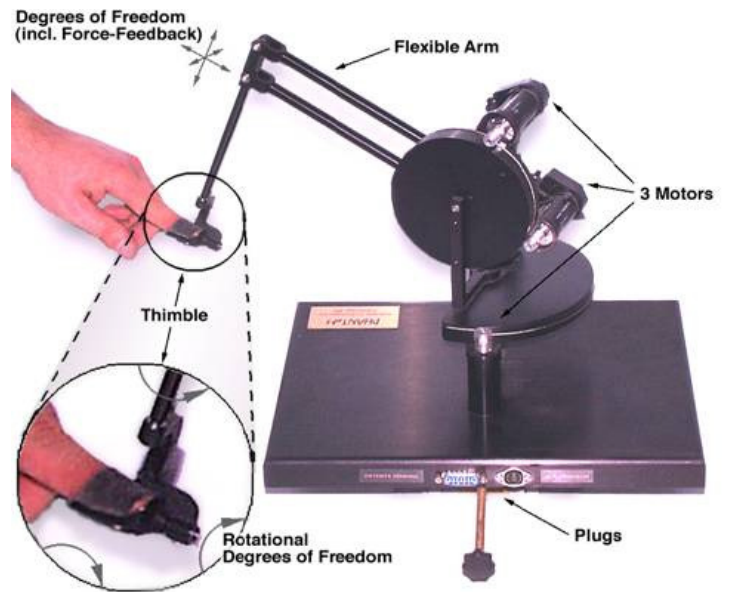


Figure 2.1 PHANToM 6DOF Haptic Device [12]

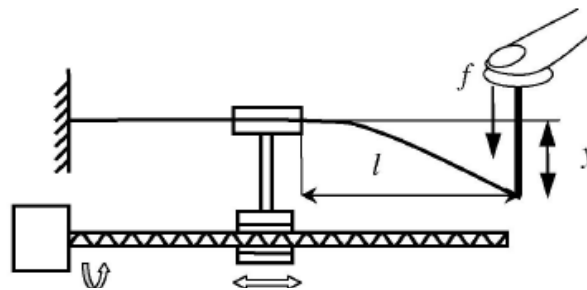


Figure 2.2 Stiffness Display Device by Liu [14]

Compared to both the devices mentioned which have single-point operation, Casiez et al. developed a new multi-finger force-feedback device called the DigiHaptic that has 3 DC motor actuated levers for the thumb, forefinger and ring finger shown in Figure 2.3 [15]. This device is claimed to be able to decouple degree of freedoms and also adds correlation between user finger and virtual object movements for a more realistic force

feedback representation. The user can feel a virtual object using 3 fingers instead of touching the virtual object at a single point.

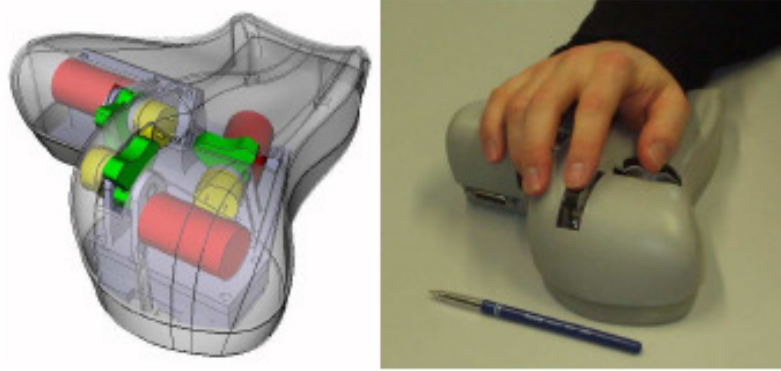


Figure 2.3 DigiHaptic Device by Casiez [15]

However, the mentioned devices are always in contact with the user for force feedback and therefore not able to differentiate the sensation of contact from non-contact like in the real environment. Yoshikawa has gone a step further by having developed a touch and force display device that overcomes this problem. Essentially a 3 DOF robot arm that provides force feedback similar to the PHANToM, this device has a ring that moves with the user finger in it via an optical positioning sensor. When contacting a virtual object, the user finger would touch the ring, simulating a touch sensation and force feedback provided by the arm [16]. Note that the above mentioned devices simulate virtual feeling in a virtual environment through for example a 3D model seen on a monitor. The device itself is not attempting to emulate any tangible form of the actual object. In fact, the point of virtual reality is just to simulate and not to emulate.

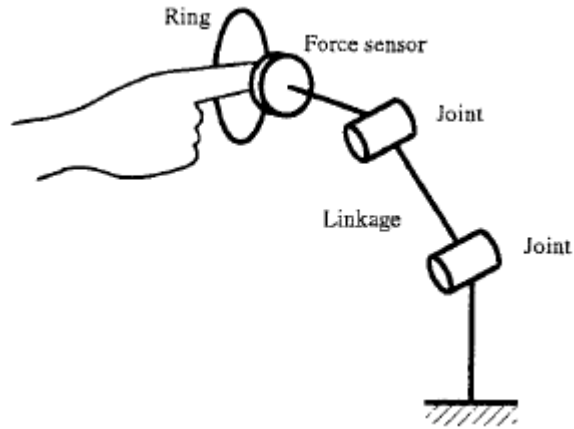


Figure 2.4 Touch and Force Display by Yoshikawa [16]

2.2.2 Planar Array Tactile Devices

Apart from force feedback devices, a device to display tactile information to the user is known as the tactile display array. It essentially consists of a planar array of actuators, filters and/or sensors that functions to measure and generate surface stress, amplitude and frequency to realistically simulate data from the environment [17]. Typically, surface roughness, texture information and small scale stiffness are displayed. Bliss in 1969 pioneered what would be the first tactile Braille reading device for aiding the blind called the Optacon [18]. This device has 144 pins in 6 x 24 arrays and with spacing of about 1.1mm between rows to 2.1mm between columns, and is a rather coarse display. Current typical tactile display array has about 8x8 actuators in a 1mm x 1mm square [19] to about 5x6 actuators in a 9mm x 9mm square [20] to about 8x8 actuators in a 16mm x 16mm square [21]. Killebrew et al. developed a dense 400 pin array for display of complex spatio-temporal patterns used in human psychophysical studies. The whole 20x20 array is only 1cm by 1cm in size, and has bandwidth up to 250Hz. The pins are individually

controlled by linear DC motor and proved to be the limiting factor in the huge actuator array size. [22]. Figure 2.5 shows the device by Killebrew.

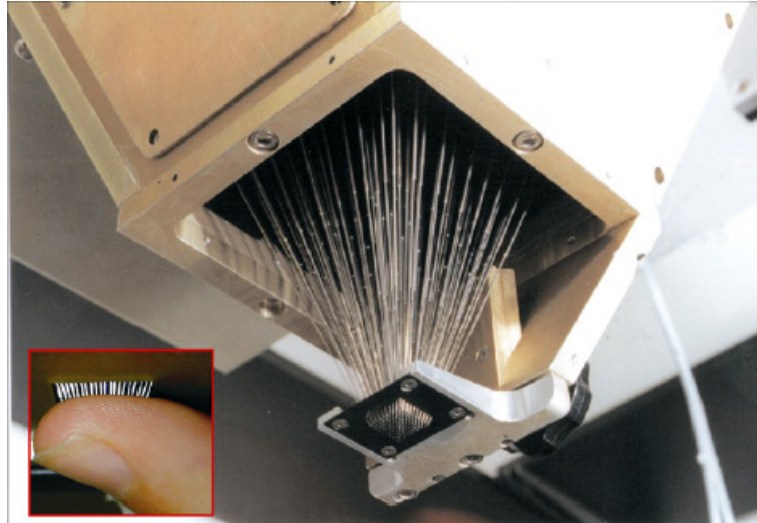


Figure 2.5 Dense 400-pin Array Tactile Stimuli by Killebrew [22]

The most common methods of actuation comprised of Piezoelectric actuators [20][23], Pneumatic actuators [24][25] and Servo Motors [26][27] although there are other types of actuation researched. According to Fisher, an ideal display requires 500 kPa (73psi) peak pressure, 4mm stroke, and 50 Hz or higher bandwidth with an actuator density of 1 per mm² [28]. The high pressure display is required to simulate material stiffness or a virtual wall. Tactile display is typically mounted on the master manipulator (user interface) for displaying information from the sensor mounted at the end-effector. Common applications are in the areas of tele-operation, remote surgery, and virtual environment simulation. Figure 2.6 shows some of the tactile devices developed by Sarakoglu [27], Kwon [20] and Wagner [26].

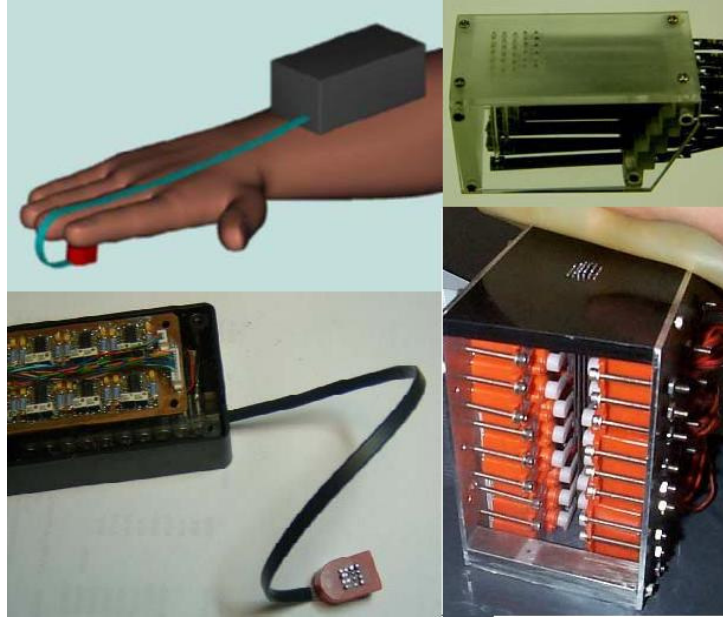


Figure 2.6 Various Tactile Devices: Sarakoglu [27] (Left), Kwon [20] (Upper Right), and Wagner [26] (Lower Right)

2.2.3 Haptic Devices Combining Tactile and Force Feedback

The device TextureExplorer by Ikei and Shiratori combined tactile sensation, force feedback and visual presentations into a single system for a complete virtual haptic experience. A 10 pin-array arranged in a 5x2 matrix mounted on the stylus end of a PHANToM device provides tactile sensation to the skin surface. The PHANToM device itself presents force feedback to the user. A projected screen gives visual representation of the virtual environment [29]. However, the device still only allows the user to “touch” a single point or a group of points in the virtual environment; spatial discontinuity is still a problem.

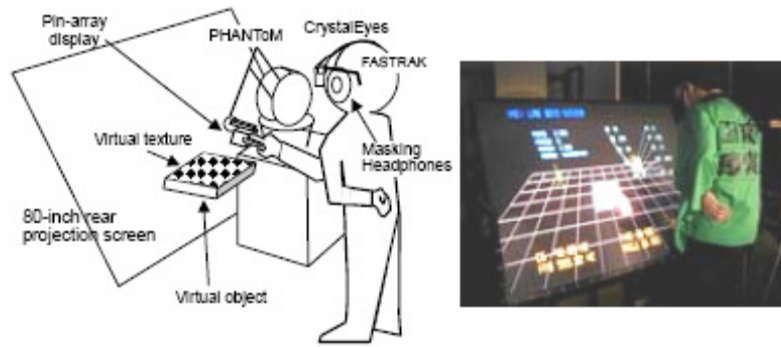


Figure 2.7 TextureExplorer by Ikei and Shiratori [29]

To address this problem, several researchers such as Iwata came up with project FEELEX [30] in Figure 2.8 and Nakatani [31] with his pin-rod matrix using Shape Memory Alloy (SMA) in Figure 2.9, which combines visual and haptic interfaces by means of a force displaying array of actuators to provide a spatially continuous surface. Similar to Digital Clay, an array of actuators move vertically in a plane to display a 2.5D surface with the top ends. FEELEX is actuated by electrical motors and actuator sizing for adequate force reflection remains the main limitation to having a high display resolution.

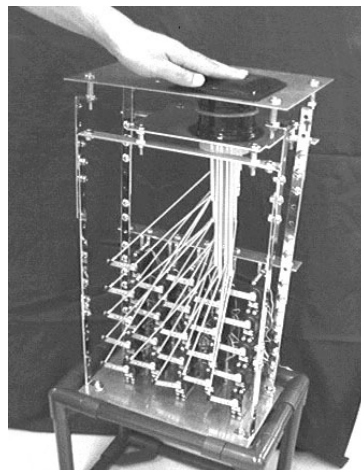


Figure 2.8 FEELEX by Iwata [30]

Nakatani uses SMA as actuators for its dense array of vertical pins with long range of movements. The pins would extend when cooled and return to its original position when heated. Due to the nature of SMA, it exhibits hysteresis and force control is difficult. Furthermore, coolant and forced convection cooling needs to be applied for fast actuation, although heating is relatively fast by passing through high current.

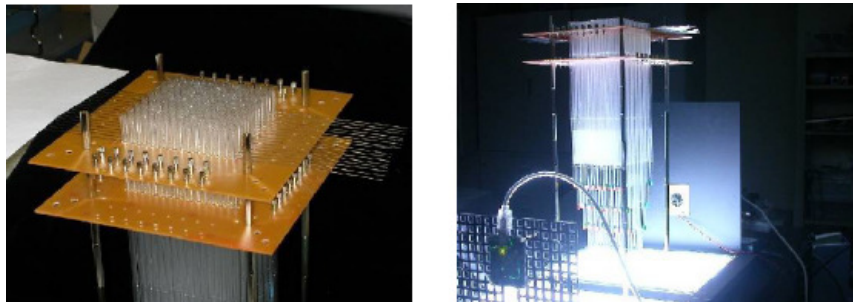


Figure 2.9 Shape Memory Alloy (SMA) Planar Haptic Device by Nakatani [31]

In 2006, Garth developed a second test bed for Digital Clay at Georgia Institute of Technology that is also a hydraulic actuated 5x5 array of linear actuators shown in Figure 2.10 [32]. The actuators have embedded inductance-based variable core transformer (VCT) position sensor and is much bigger in size compared to Zhu's prototype. The 5x5 array has an overall size of 160 mm by 160 mm square and each actuator has 30 mm travel. The system also has pressure sensors embedded. Each actuator is capable of lifting about 3.3N and holding 5.8N of weight with a 30psi pressurized reservoir compared to Zhu's prototype which is much smaller in size (20 mm by 20 mm) but only capable of lifting less than 1N of weight with 25psi pressurized reservoir.

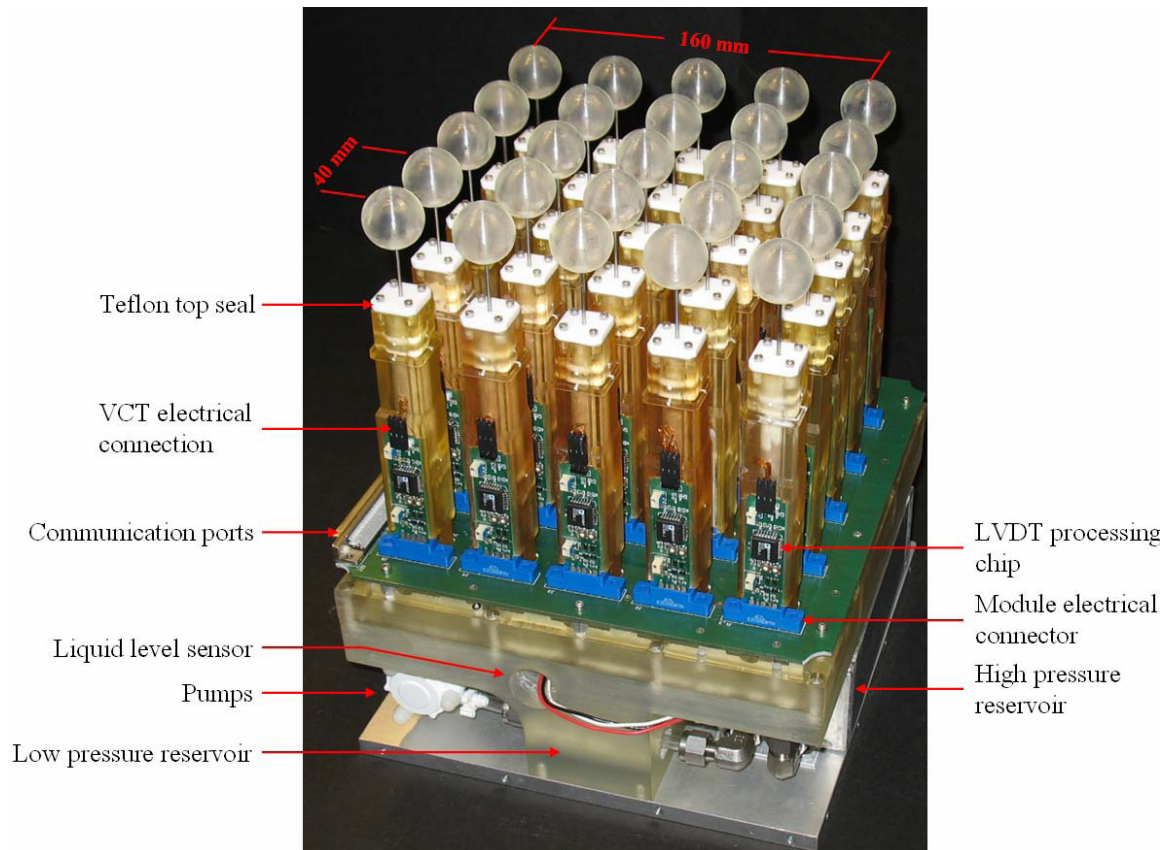


Figure 2.10 Digital Clay Testbed 2 by Garth [32]

Zhu's Digital Clay concept is similar to the tactile display array in that it is a tactile display array combined with tangible visual shape display except for not having the same sensing capability, but having a larger stroke of about 50mm, and also smaller bandwidth (~8Hz). The current 5x5 prototype does not have pressure sensors embedded therefore having force sensing and force display capability would make Digital Clay a complete tactile haptic device.

CHAPTER 3 DIGITAL CLAY DISPLACEMENT AND VELOCITY CONTROL

Digital Clay displacement sensor embedded actuator structure and working principle is explained in 1.1.2. To maintain compact size and reduce hardware complexity, the displacement sensor is the most feasible and important sensor for the system; hence it is vital to be able to obtain accurate and reliable displacement measurements from each sensor for control purposes. The accuracy of actuator velocity and acceleration information ultimately depends on the information from the derivative(s) of displacement sensors as there is no added hardware for this information. This chapter will first evaluate the accuracy and reliability of the displacement sensor; then selecting the best method of obtaining velocity information by comparing several methods; and designing appropriate displacement and velocity controller algorithm for Digital Clay goal stated in Chapter 1.

3.1 5x5 Prototype Actuator Array Locations and Naming Convention

Before going further into the system of Digital Clay prototype, a convention will be defined and used throughout the thesis to refer to the actuator by positional coordinates and/or numeric identification.

Figure 3.1 shows the following 5x5 actuator array if view from the top-front of the system assembly.

| | | | | | |
|------------|----------|----------|----------|----------|----------|
| 4 | 21 | 22 | 23 | 24 | 25 |
| 3 | 16 | 17 | 18 | 19 | 20 |
| 2 | 11 | 12 | 13 | 14 | 15 |
| 1 | 6 | 7 | 8 | 9 | 10 |
| 0 | 1 | 2 | 3 | 4 | 5 |
| y/x | 0 | 1 | 2 | 3 | 4 |

Figure 3.1 Digital Clay Pin Location and Naming Convention

When facing the system from the top-front, the lower left corner of the actuator array will be the origin (0,0) location while the upper right corner will be the (4,4) location. If a numerical identification is used, actuator at (0,0) will be actuator number 1 and in increment from left to right, row by row, until pin 25. This convention will be used whenever there is more than 1 actuator of interest mentioned. The coordinate system is also used in the software to control the row and column valves.

3.2 Displacement Sensor Accuracy and Repeatability Evaluation

The output from the displacement sensor was compared with actual displacement measurement using a commercial linear variable differential transformer (LVDT). The displacement sensor output is a square wave with amplitude relative to a 5V square wave excitation voltage and converted with a 12-bit Analog to Digital converter (ADC). The output amplitude will be highest at the highest displacement and lowest amplitude at the lowest displacement. The sensor is calibrated with a LVDT displacement sensor from zero position when the pin is fully retracted to 48mm when the pin is fully extended.

The actuator will be extended manually by hand to different random vertical displacements and both the calibrated displacement and actual measured displacement

values in millimeters are plotted to evaluate its accuracy. The results are shown in Figure 3.2 below. The curve fit result of 0.9995 and a sum of squared error (SSE) of 1.27 suggests that indeed the displacement sensor data has been calibrated to good accuracy and increases the confidence in its use. The sensor resolution is 0.25mm.

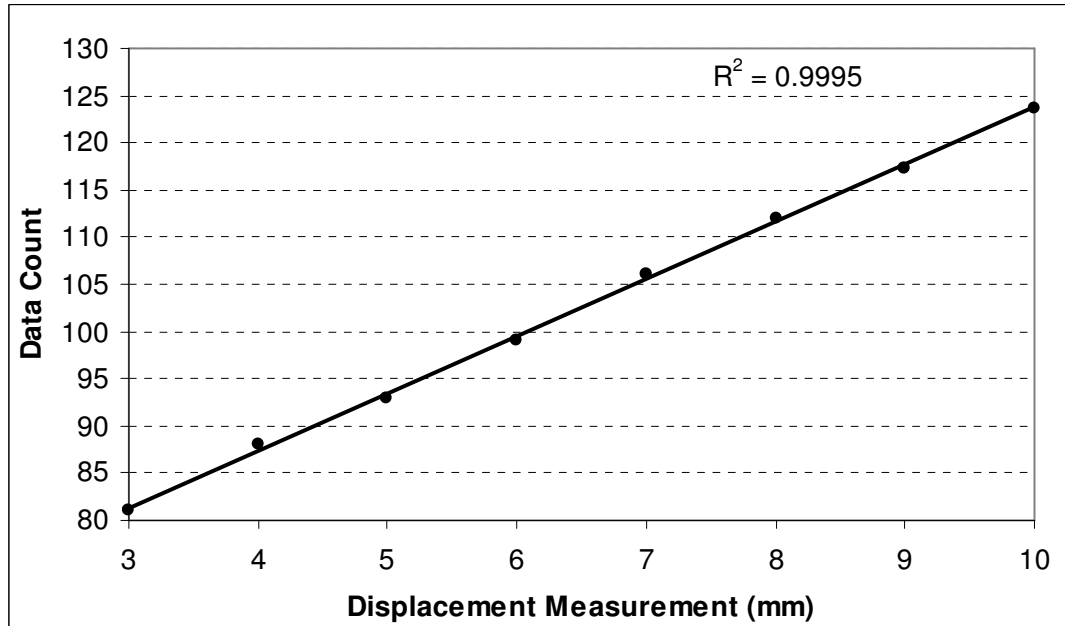


Figure 3.2 Comparison between Sensor Data Count and LVDT Displacement Measurement

3.3 Obtaining Velocity from Displacement Measurements

3.3.1 Finite Difference Approximation

Since velocity is the first derivative of position, the first method is to perform finite difference to approximate the velocity. There are 3 commonly used methods of finite difference, forward, backward and central difference. From Taylor's series expansion and neglecting higher order terms, the finite difference can be approximated as:

$$y'(t) \approx \frac{y(t + \Delta t) - y(t)}{\Delta t} \quad (3.1)$$

$$y'(t) \approx \frac{y(t) - y(t - \Delta t)}{\Delta t} \quad (3.2)$$

$$y'(t) \approx \frac{y\left(t + \frac{1}{2}\Delta t\right) - y\left(t - \frac{1}{2}\Delta t\right)}{\Delta t} \quad (3.3)$$

for forward, backward and central difference respectively. In real time application, only backward difference is realizable as forward and central difference requires the knowledge of the displacement in the future, unless delay is introduced, which defeats the purpose of real-time estimation. An example is shown below for backward difference approximation of the command and displacement measurement of sine wave tracking respectively.

In Figure 3.3, the method of finite difference approximation is the simplest algorithm to estimate velocity from displacement measurements, but the result is phase shifted and noise is amplified. When the generated sine wave trajectory is a discrete function, the finite difference shows a jagged signal. If a displacement signal is noisy, low pass filtering is required. A 2nd order digital Butterworth filter, $F(z)$ with cutoff frequency of 30Hz is used,

$$F(z) = \frac{0.00001(1.14z + 1.13)}{z^2 - 1.993z + 0.9933} \quad (3.4)$$

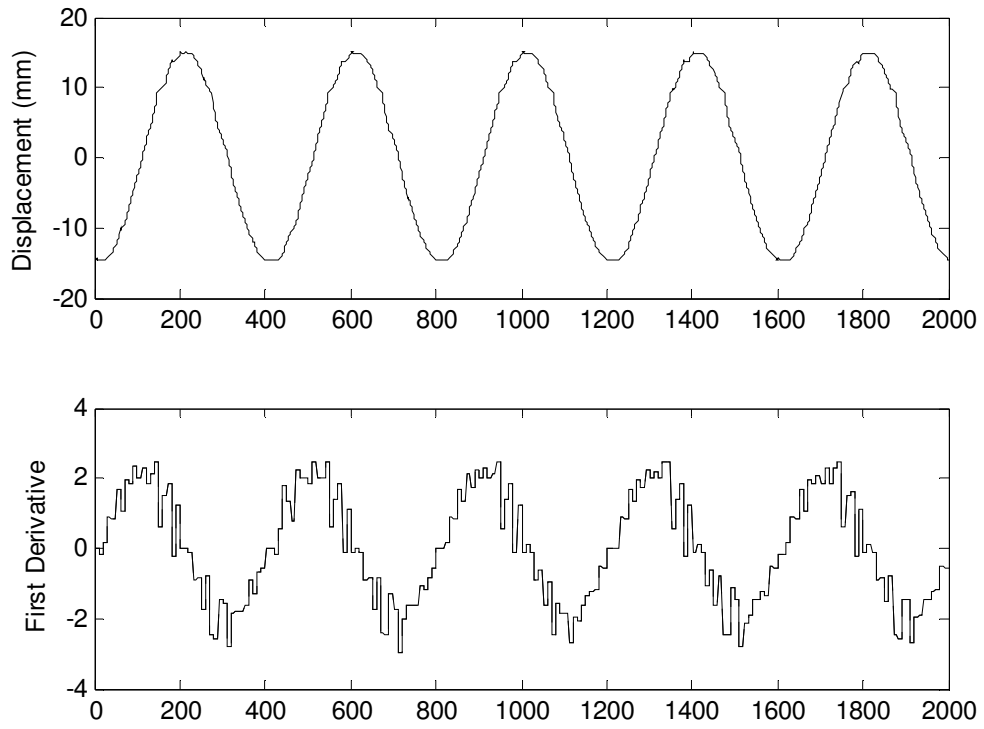


Figure 3.3 Measurement Signal First Derivative Approximation

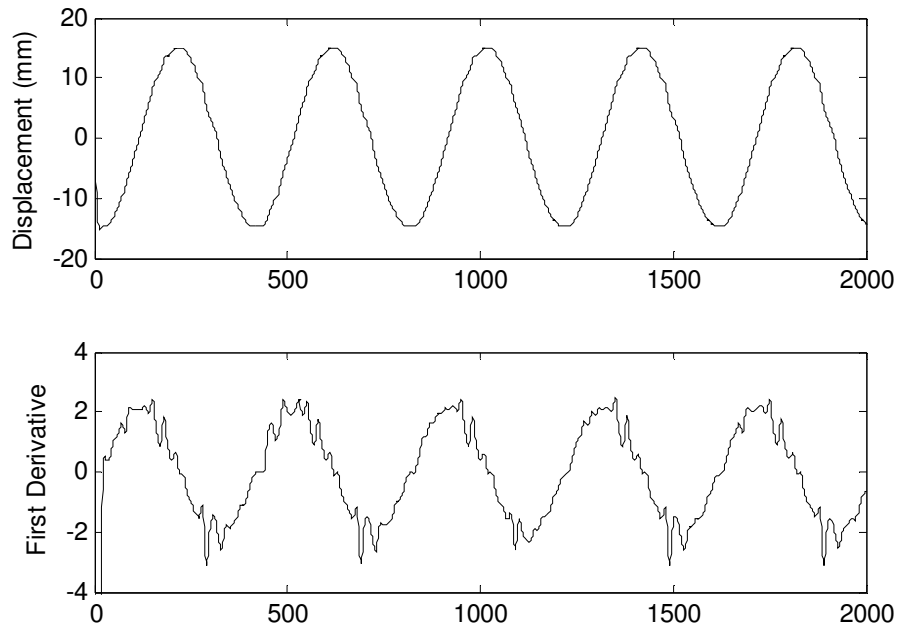


Figure 3.4 2nd Order Filtered Signal First Derivative Approximation

Figure 3.4 showed that by filtering the finite differentiated signal, high frequency components are removed and the smoother signal yields better velocity information but still not able to fully remove estimation error spikes. A higher order low pass filter will increase delay effect to the estimation and it is not desirable to reduce the bandwidth.

3.3.2 Alpha-Beta-Gamma Filtering

A steady-state filter known as the alpha-beta-gamma filter [33] is commonly used in radar and global positioning system (GPS) application to approximate the velocity of a target from position measurement. This filter is derived from the steady-state form of Kalman filter with constant gains α , β , and γ . The filter equation is given as,

$$\bar{\mathbf{x}}(k) = \begin{bmatrix} 1 & T & \frac{T^2}{2} \\ 0 & 1 & T \\ 0 & 0 & 1 \end{bmatrix} \hat{\mathbf{x}}(k-1) + \tilde{\mathbf{w}}(k-1) \quad (3.5)$$

$$\hat{\mathbf{x}}(k) = \bar{\mathbf{x}}(k) + \mathbf{L}[y(k) - \bar{x}_1(k)]$$

where $x(k)$ is the matrix with states of position, velocity and acceleration. The prediction, $\hat{\mathbf{x}}(k)$ involves the current states, $\bar{\mathbf{x}}(k)$ and estimation error, $y(k) - \bar{x}_1(k)$. The output is the measured displacement, $y(k)$. The noise $\tilde{\mathbf{w}}$ is assumed to be zero-mean and white Gaussian. For this filter in (3.5), pin acceleration is assumed to be constant at sampling interval, T . The filter gain matrix, \mathbf{L} consists of gains α , β , and γ , is determined from (3.6) by choosing a small $\alpha = 0.1$ first and solving for β , and γ in (3.7) and (3.8). The gain α is chosen from trial and error based on the trade-off between smoothness (filtering) and

phase-shift. In other words, the gains are chosen to minimize the mean-square errors in the estimates. Figure 3.5 shows the velocity as estimated by the alpha-beta-gamma filter. The velocity estimate is more accurate as estimate error is taken into account and the noise reduction characteristic of the filter is an advantage over finite difference approximation. In designing this filter, the α value is chosen to be small to avoid instability.

$$\mathbf{L} = \begin{bmatrix} \alpha & \frac{\beta}{T} & \frac{\gamma}{2T^2} \end{bmatrix}^T \quad (3.6)$$

$$\beta = 2(2 - \alpha) - 4\sqrt{1 - \alpha} \quad (3.7)$$

$$\gamma = \frac{\beta^2}{\alpha} \quad (3.8)$$

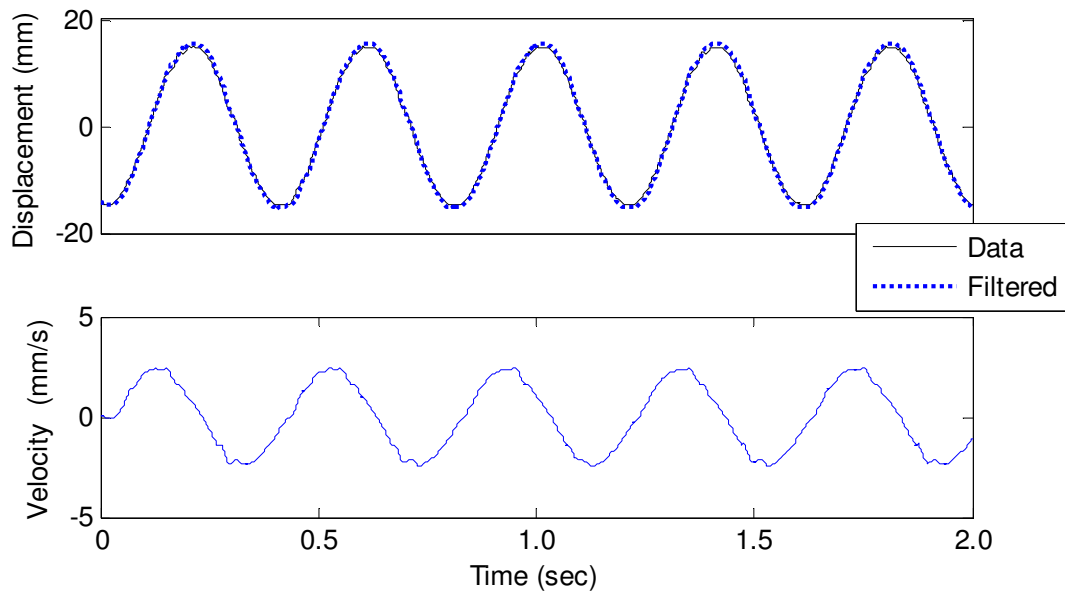


Figure 3.5 Alpha-Beta-Gamma Filter Prediction of Velocity

3.3.3 Low Velocity and Low Acceleration Estimator (LAE)

As can be seen from the two previous methods, estimating actual velocity from displacement measurements with differentiations can cause the amplification of noise and erroneous behavior in the low velocity sections. As investigated and proposed by Lee and Song [34], a new algorithm to accurately estimate especially low velocity and low acceleration will be shown and applied to Digital Clay. The basic idea is that numerical integration is more stable and accurate than numerical differentiation, and assuming the displacement information is accurate.

Based on Figure 3.6, the estimated displacement, x_e is the integral of the estimated velocity, v_e , which in turn is the integral of the estimated acceleration, a_e . The error between actual displacement measurement, x and x_e are multiplied by gain K_1 and subtracts v_e multiplied by gain K_2 to act as a proportional-derivative (PD) controller such that x_e tracks x . This is summarized as equation (3.9) and (3.10).

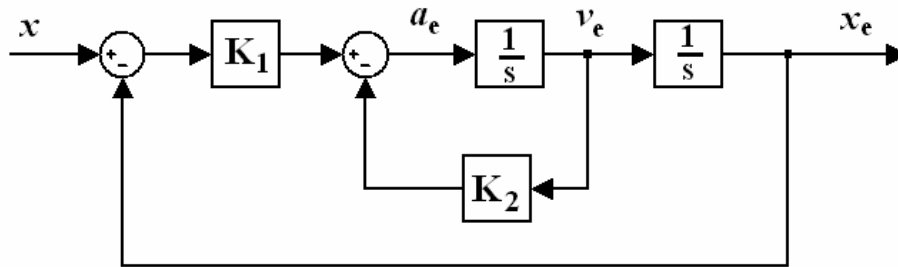


Figure 3.6 Low Velocity and Low Acceleration Estimator Block Diagram

$$\begin{bmatrix} \dot{x}_e \\ \dot{v}_e \end{bmatrix} = \begin{bmatrix} 0 & 1 \\ 0 & 0 \end{bmatrix} \cdot \begin{bmatrix} x_e \\ v_e \end{bmatrix} + \begin{bmatrix} 0 \\ 1 \end{bmatrix} \cdot a_e \quad (3.9)$$

$$a_e = K_1 \cdot (x - x_e) - K_2 \cdot v_e \quad (3.10)$$

The transfer function from x to x_e is given as,

$$\frac{X_e}{X} = \frac{K_1}{s^2 + K_2 s + K_1} = \frac{\omega_b^2}{s^2 + 2\xi\omega_b s + \omega_b^2} \quad (3.11)$$

and the gains K_1 and K_2 are related to the damping ratio and bandwidth, $K_1 = \omega_b^2$, $K_2 = 2\xi\omega_b$.

By letting $\xi = 0.7071$, which is the critical damping ratio, a fastest response without overshooting can be obtained. Let $\omega_b = 50$ Hz as the bandwidth. A higher bandwidth will be better for increasing tracking capability, but too high of a bandwidth will also adversely effect the estimation performance. A large bandwidth will enable estimator to track discontinuity and be more robust for higher frequency components. If the acceleration variation is not very large, the bandwidth can be reduced.

For implementation on Digital Clay, the discretized version of this estimator with sampling time, T is,

$$\begin{bmatrix} x_e(k+1) \\ v_e(k+1) \end{bmatrix} = \begin{bmatrix} 1 & T_s \\ 0 & 1 \end{bmatrix} \cdot \begin{bmatrix} x_e(k) \\ v_e(k) \end{bmatrix} + \begin{bmatrix} \frac{T_s^2}{2} \\ \frac{T_s}{1} \end{bmatrix} \cdot a_e(k) \quad (3.12)$$

$$a_e(k) = K_{D1} \cdot (x(k) - x_e(k)) - K_{D2} \cdot v_e(k) \quad (3.13)$$

and the gains are given by, $K_{D1} = K_1$, $K_{D2} = \frac{K_2}{T_s}$.

Figure 3.7 shows the velocity estimation using the LAE which effectively attenuates measurement noise with the double integrator model. The result is better compared to the finite difference approximation in Figure 3.4. Both the displacement sensor data and differentiated signal has to be filtered, but the LAE does not require a separate filtering of the displacement sensor data before running the algorithm. Thus the LAE algorithm is simpler to implement than the finite difference approach and the Alpha-Beta-Gamma filter in Figure 3.5. Hence this approach will be implemented on the Digital Clay prototype to obtain velocity information for each actuator. As each of the actuator has uncertain parameters and varying characteristics, this robust approach is the best method to ensure accurate information without involving the model of each actuator.

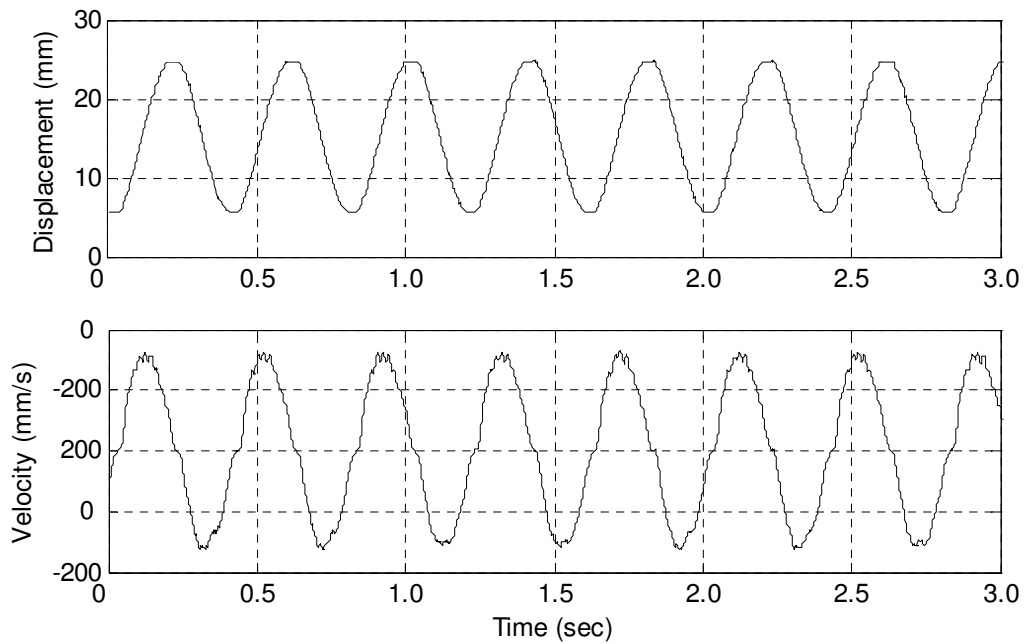


Figure 3.7 LAE Estimation of Actuator Velocity

3.4 Digital Clay Actuator Displacement and Velocity Tracking Controller

The displacement control law for Digital Clay actuator is achieved using a simple proportional controller where the duty ratio, $u(t)$ is proportional to the tracking error or the difference between the desired displacement, $y_{desired}$ and measured displacement, $y_{measured}$. The control law is given by,

$$u(t) = K_p \cdot (y_{desired} - y_{measured}) \quad (3.14)$$

Figure Figure 3.8 and Figure 3.9 below show how well the actuator tracks a sine wave and a square wave displacement respectively.

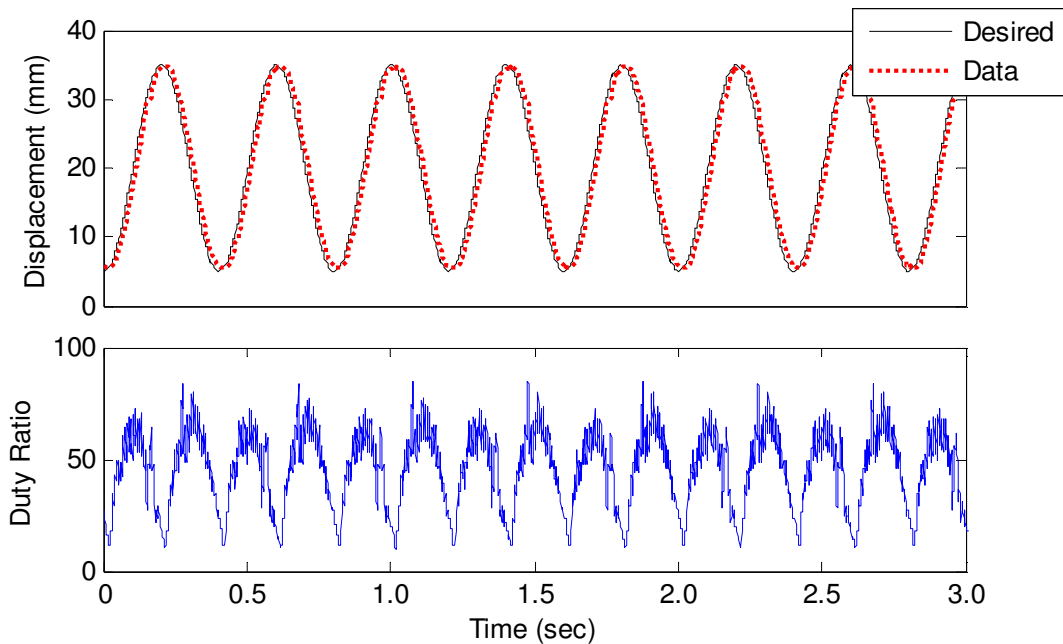


Figure 3.8 Actuator Sine Wave Displacement Tracking

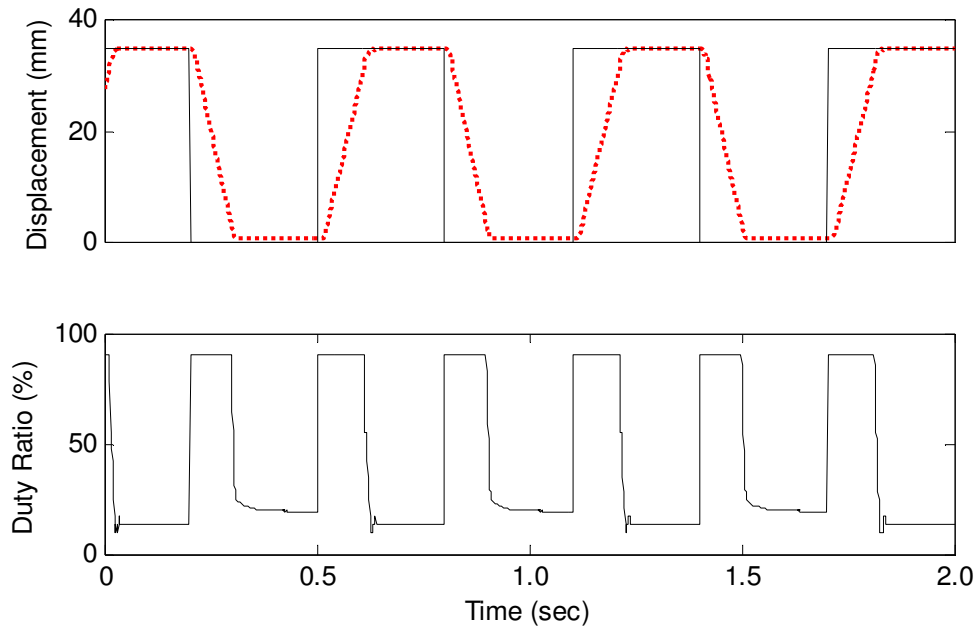


Figure 3.9 Actuator Square Wave Displacement Tracking

From Figure 3.9, the actuator tracking speed is limited by the both physical and software-implemented saturation at 90% duty ratio. By increasing system pressure, a faster response can be achieved. Otherwise, both sine wave and square wave tracking is excellent for this application within the physical limits and valve saturation.

For the velocity tracking, from experience a feed forward plus feed back controller is needed. The control law can be written as:

$$u(t) = (a_1 \cdot v_{desired} + a_2) + K_v(v_{desired} - v) + K_D(v(k) - v(k-1)) \quad (3.15)$$

The feed forward term is a result of linear curve fitting of velocity vs. duty ratio plot which are given in Appendix 1 for all 25 actuators. This term will attempt to give an ‘initial’ duty ratio, $u(t)$ and any error from $(v_{desired} - v)$, the duty ratio will be compensated

by the proportional feedback gain, K_v multiplied by the error. The derivative gain, K_D will remove oscillation by introducing a damping behavior.

From curve fitting, the coefficients are $a_1 = 0.422$ and $a_2 = 17.93$. The goodness of fit is $r^2 = 0.983$. Figure 3.10 below shows the curve fit of Velocity vs. PWM Duty Ratio. For negative velocity, (downward displacement), the same parameters are used. The return pressure is chosen such that velocity is symmetric upwards and downwards.

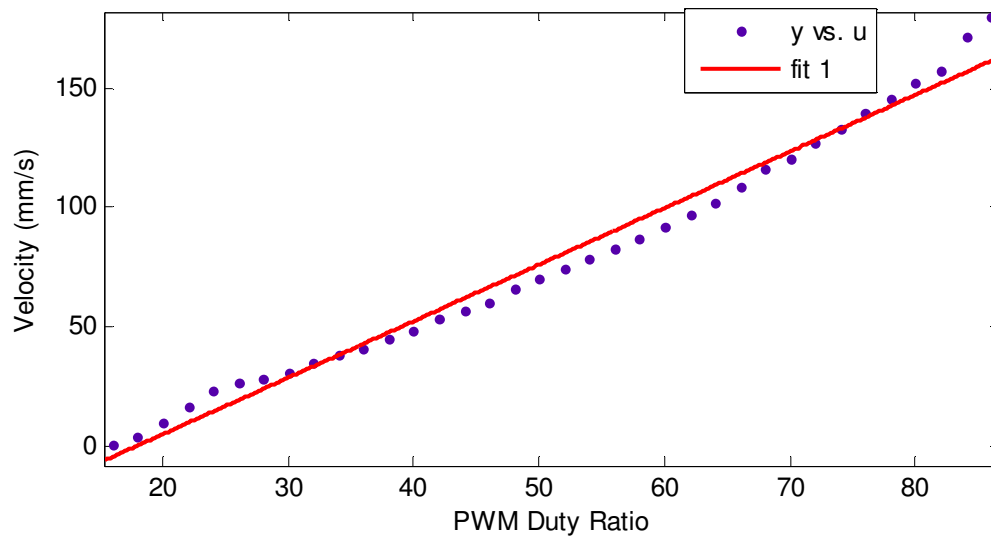


Figure 3.10 Velocity vs. PWM Duty Ratio Linear Curve Fit for (0,0)

The tracking of a square wave velocity under proportional feedback is shown in Figure 3.11. The gain, K_v used was 0.5. A higher gain (Figure 3.12) would result in increased oscillation while a lower gain would increase rise time thus the derivative of the error is needed to remove oscillation.

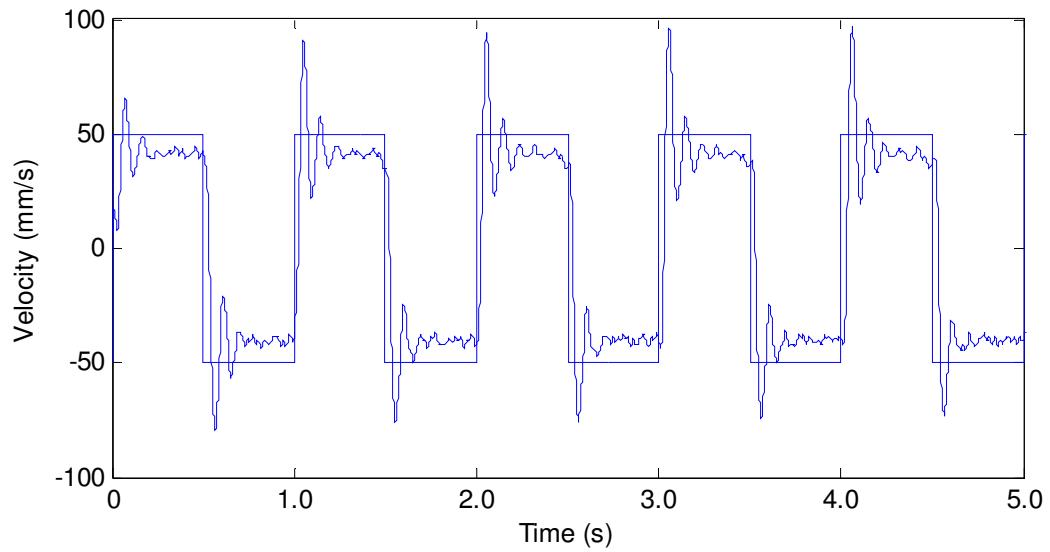


Figure 3.11 Square Wave Velocity Tracking with Proportional Feedback ($K_v=0.5$)

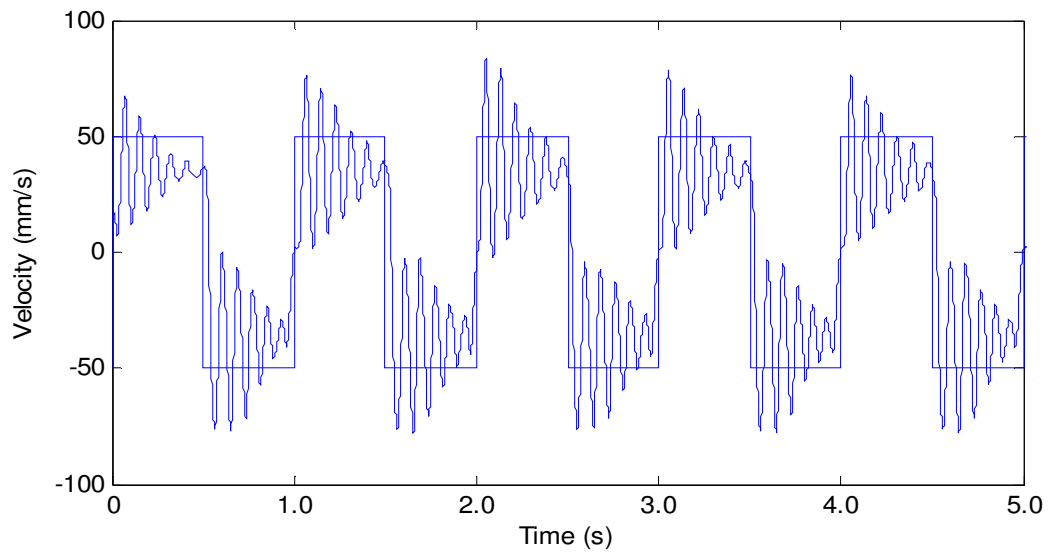


Figure 3.12 Square Wave Velocity Tracking with Proportional Feedback ($K_v=1$)

By increasing the feed forward gain to 2.5, reducing the proportional feedback gain to 0.1 and introducing the derivative of error term with gain of 5, steady state error and overshoot are reduced, while the rise time is maintained. By selecting appropriate gains,

this controller is robust enough if applied to all 25 actuators without resorting to switching control gains. The result is shown in Figure 3.13, along with how the triangular profile displacement looks.

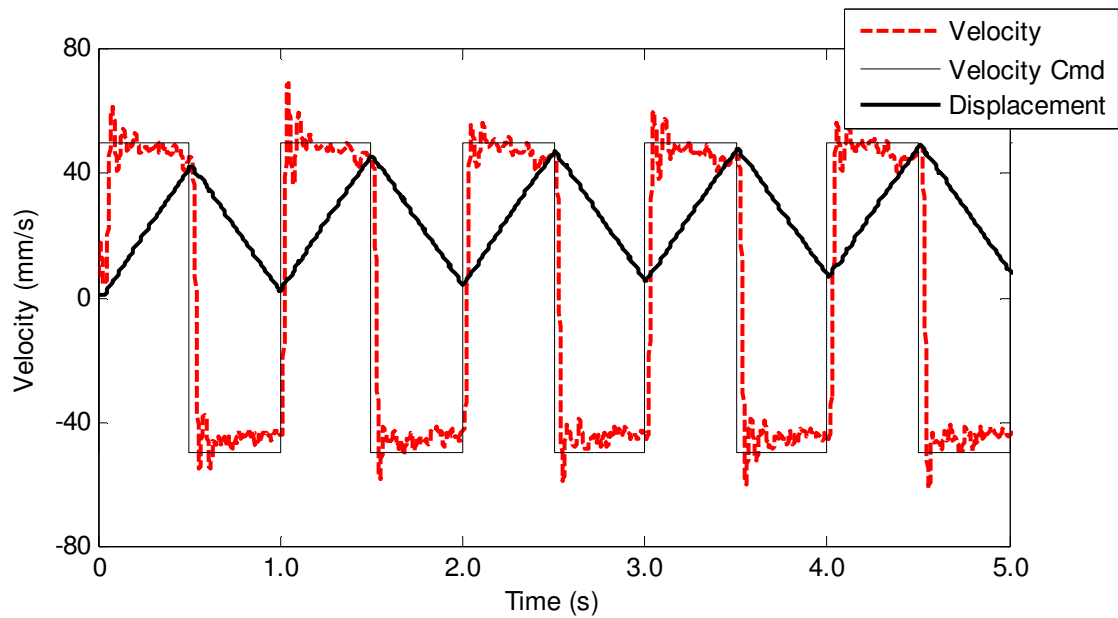


Figure 3.13 Square Wave Velocity Tracking with Proportional Derivative Feedback ($K_v=0.1$, $K_D=5$)

3.5 Remarks and Discussion

In this chapter, the displacement sensor was shown to be highly linear and repeatable for Digital Clay application. Three methods of estimating actual velocity from displacement measurements are presented and the best estimator is the Low Velocity and Low Acceleration Estimator (LAE). The alpha-beta-gamma filter provides good velocity estimates but assumes that the acceleration of the actuator is constant, which is not the case with Digital Clay application. The Low Acceleration Estimator uses the integral of displacement signal instead of the difference; which has the effect of attenuating measurement noise. In addition, the structure of the LAE is simpler than the alpha-beta-gamma filter and takes up very little computational and memory resources. This method is not only applicable to Digital Clay but is a reliable and straightforward method of estimating velocity and acceleration from any displacement sensor measurements. As with any estimator, low noise and repeatable sensor output is highly desired. The design steps for both position and velocity control are outlined with great detail and satisfactory results with a PD controller has been achieved. As for the controller, the PD gains have to be specifically tuned for each actuator of Digital Clay as the parameters may vary by a great amount. For future research, an adaptive controller or a robust controller can be implemented, which will require higher computational costs.

CHAPTER 4 DIGITAL CLAY SINGLE ACTUATOR SYSTEM MODELING AND SIMULATION

The force feedback capability required to realize Digital Clay as a haptic HMI device means that a suitable control algorithm is needed. Typically in a control loop, a feedback signal of the variable of interest is needed to generate appropriate control signal to drive the actuator such that the feedback signal would track the desired trajectory with good accuracy. However as mentioned in Chapter 1, the use of force sensors as feedback would not be an optimal solution for the large scale actuator array of Digital Clay. Instead, alternative solution has to be devised. Thus the goal of this chapter is to study the overall Digital Clay system in detail by combining theoretical and experimental investigations to better understand its behavior. The knowledge gained from this study will then be used to design alternative solutions to achieve the goal of force feedback for Digital Clay. Furthermore, a close study of the behavior and characteristics of this novel device has not been done, which further motivates the work in this chapter. First, the frequency response of the single actuator system is investigated. Then, a model is derived from a set of differential equations describing hydraulic systems. The model is compared with actual experimental data for validity.

4.1 Digital Clay as an Electro-Hydraulic System

Digital Clay can be classified as an electro-hydraulic system which means that the main actuator's power source is pressurized fluid but it requires the control of electronic solenoid valves and feedback of position by electrical signals. A main microprocessor unit is programmed to control the actuators in a desired manner. Even though the overall system consists of many other electrical and mechanical components, by focusing on the main components and effects that govern its behavior, an accurate mathematical representation can be obtained. The hydraulic schematic of the 5x5 system is shown in Figure 1.3.

The row control valves are pulse width modulated (PWM) to control the flow into the actuators. By assuming that there is no time delay in the process of generating the duty ratio in the computer and converting the digital signal to analog on/off voltage output, this schematic is a fairly accurate representation of the actual system. The overall system consists of repeated actuator units which have differing parameters; however with similar structure. For a single unit of the array shown in Figure 4.1, the plant to be modeled consists of the piston-cylinder actuator, the control adapter, and a set of solenoid valves. Transmission line effects are assumed to be negligible as the actuator size is much larger than the fluid channel diameter in the system.

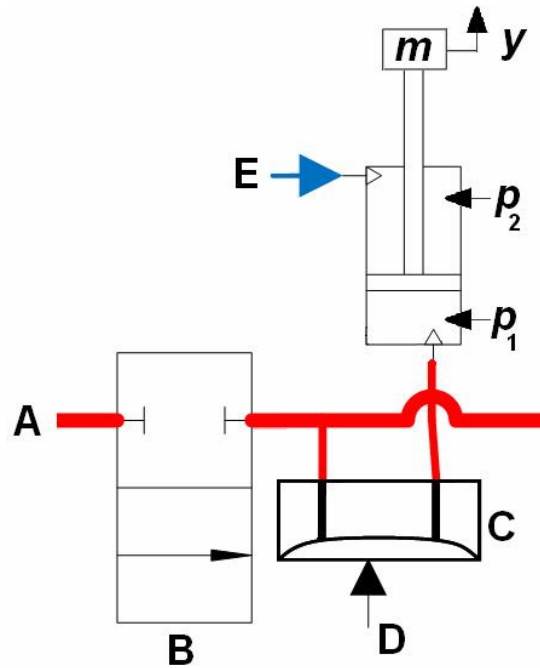


Figure 4.1 Single Digital Clay Actuator Schematic

As the high pressure fluid A enters the array, the input for the plant is the average voltage applied to the valve, B via pulse width modulation (PWM) which determines the average flow rate into the actuator. The effects of the control membrane, C and its time response to high-pressured air, D is assumed to be instantaneous and not taken into account. The return pressure, E is a constant. The output that is sensed is the vertical displacement, y while unmeasured states are the pressures in both chambers of the actuator, p_1 and p_2 . To simplify the model, the model input is taken to be the duty ratio of the PWM. It is assumed that the duty ratio applied to the valve is proportional to the average flow rate out of the valve.

4.2 Frequency Response of a Single Actuator

From fluid dynamics, the simplified relationship between the input signal applied to a valve and its flow rate is given by the following equation [35],

$$Q = c_d A_{\text{orifice}} \sqrt{\Delta p} \quad (4.1)$$

where Q is the flow rate, c_d is the coefficient of discharge, and Δp is the pressure difference across the valve. There is no energy loss modeled. If the input PWM duty ratio is proportional to the average orifice area, A_{orifice} of the valve, then the duty ratio is also linearly related to the flow rate for any particular instance when c_d and Δp are constant. It is also known that for a linear actuator such as the piston-cylinder, the velocity of the piston is proportional to the flow rate into the cylinder,

$$Q = A_{\text{cylinder}} V \quad (4.2)$$

Loosely speaking, the relationship between the PWM duty ratio and actuator piston is a proportional relationship. Appendix A1 to A5 show the plots of 25 Digital Clay actuators as function of PWM duty ratio input for supply pressures of 25psi and 10psi of return pressure. As expected, the plots are slightly non-linear for both cases due to unmodeled dynamics such as friction, leakage and gravitational effect, but otherwise have nearly linear characteristics. The actuators have saturation zone from about 95% of duty ratio, however they show considerable dead band up to about 20% of duty ratio. The dead band

effect can be minimized by lowering the return pressure applied on the actuator to obtain a uniform velocity for both upwards and downwards travel. As there are variations in the behavior of each actuator sub-system, a single model with single set of nominal parameters can not be adequate to represent all 25. Therefore, a general model structure will be derived and each actuator will have a unique set of parameters from system identification. The following investigation will use the actuator in the (0,0) location to show the steps taken. The frequency response of the single actuator system is investigated by applying several sinusoidal input duty ratios with varying frequencies and measuring the magnitude of the actuator velocity. Table 4.1 shows the period of the sinusoidal inputs and the corresponding velocity magnitude.

Table 4.1 Single Actuator Experimental Frequency Response Data

| Input Sine Period (sec) | Frequency (Hz) | Frequency (rad/s) | Duty Ratio Magnitude (%) | Velocity Magnitude (mm/sec) | Magnitude(dB) |
|-------------------------|----------------|-------------------|--------------------------|-----------------------------|---------------|
| 1.62 | 0.62 | 3.9 | 30 | 271.7 | 19.1 |
| 1.31 | 0.77 | 4.8 | 30 | 262.0 | 18.8 |
| 1.05 | 0.96 | 6.0 | 40 | 362.4 | 19.1 |
| 0.78 | 1.28 | 8.0 | 40 | 332.6 | 18.4 |
| 0.51 | 1.95 | 12.3 | 40 | 338.9 | 18.6 |
| 0.26 | 3.85 | 24.2 | 40 | 303.8 | 17.6 |
| 0.13 | 7.69 | 48.3 | 40 | 263.1 | 16.4 |
| 0.10 | 10.20 | 64.1 | 40 | 193.9 | 13.7 |
| 0.07 | 14.71 | 92.4 | 40 | 169.8 | 12.6 |
| 0.05 | 18.87 | 118.6 | 40 | 142.3 | 11.0 |
| 0.05 | 20.00 | 125.7 | 40 | 121.6 | 9.7 |
| 0.04 | 23.26 | 146.1 | 40 | 113.8 | 9.1 |
| 0.03 | 35.71 | 224.4 | 40 | 102.5 | 8.2 |

Figure 4.2 shows the Bode magnitude plot of a single actuator for velocity as the output. The bandwidth of the actuator or when the magnitude drops 3dB is about 8Hz.

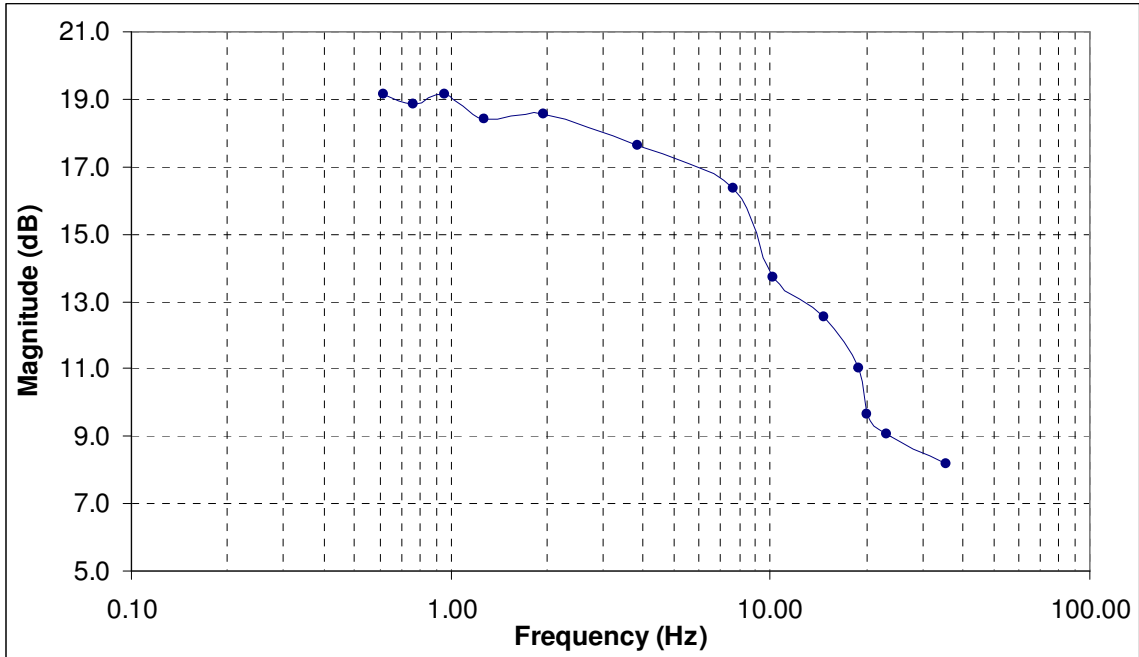


Figure 4.2 Frequency Response Magnitude Plot of Single Actuator

The next section will outline a model derived from hydraulic system differential equations which will be an essential element for designing a force observer.

4.3 Model of Digital Clay Single Actuator from Mathematical Equations

The single-pin model of Digital Clay consists of a micro-miniature on/off solenoid valve that is pulse width modulated for flow control, a glass cylinder with graphite piston that forms the actuator unit, and a brass rod that acts as the pin between the user and the Digital Clay surface. When extending upwards, the fluid flows from the reservoir and through the valve into the cylinder to push the piston up. The return fluid will be forced out at the top of the cylinder and sucked out with a pump to sink. When retracting, the high pressure fluid from the reservoir will be disconnected from the valve and switched

to a sink for fluid in the lower portion of the cylinder to exit through the same valve. The combined weight of the brass rod and return fluid pressure will then push the piston down.

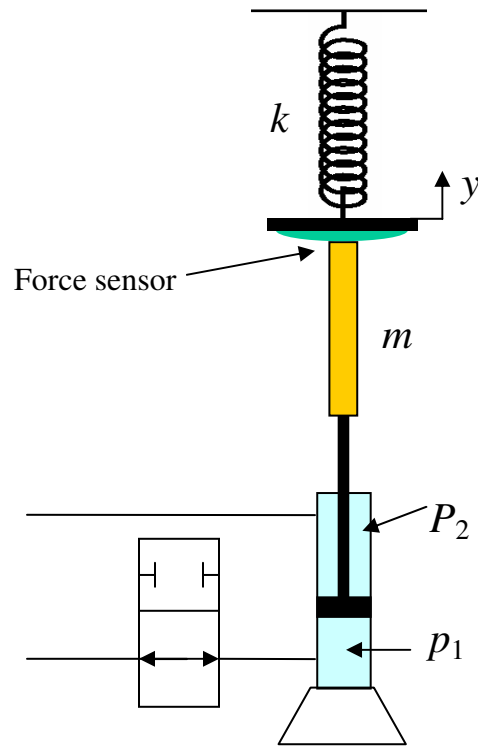


Figure 4.3 Digital Clay Single Actuator and Spring Force Experiment Schematic

The single digital clay pin model is derived from common hydraulic system equations [35]. From Figure 4.3, the model diagram consists of a spring with stiffness k , representing the environment that the pin is pushing against. The stiffness can be changed to represent different situations, for example, a high value of k represents a stationary stop, while a really low value of k represents no reaction or free motion. The brass rod has mass, m while the pressures in the cylinder are expressed as p_1 and p_2 respectively. Let the vertical displacement of the pin be represented as y . Then the force balance equation can be written as,

$$p_1 A_1 - p_2 A_2 - b\dot{y} - F_{\text{reaction}} - \text{sgn}(\dot{y}) \cdot f_{\text{coulombic}} - mg = m\ddot{y} \quad (4.3)$$

where A_1 and A_2 are the effective areas of the piston-cylinder, b is the average actuator damping constant, $f_{\text{coulombic}}$ is the coulombic friction that opposes the motion of the actuator and g is the acceleration due to gravity. The reaction force in this case is just $F_{\text{reaction}} = k \cdot y$. In real life, the value of environmental stiffness, k is not usually known, thus it is not able to simply estimate the reaction force by $F_{\text{reaction}} = k \cdot y$. The reaction force will thus be left as an unknown. The force sensor is assumed to be highly stiff compared to the environment stiffness and not taken into account. In fact, all the external forces can be modeled as a single disturbance force, $F_d = F_{\text{reaction}} + \text{sgn}(\dot{y}) \cdot f_{\text{coulombic}} + mg$. This lumped parameter model will be useful when designing the force estimator in the next chapter.

The nonlinear equations for flows q_1 and q_2 through an orifice are given by,

$$q_1 = c_{d,1} w x_v \cdot \text{sgn}(p_s - p_1) \sqrt{\frac{2}{\rho} |p_s - p_1|} \quad (4.4)$$

$$q_2 = c_{d,2} A_2 \cdot \text{sgn}(p_2 - p_{\text{return}}) \sqrt{\frac{2}{\rho} |p_2 - p_{\text{return}}|} \quad (4.5)$$

for extension of piston not under external finger force, where c_d is the valve coefficient of discharge, w is the gradient associated with the valve opening, x_v is the valve spool position that is proportional to the control signal, ρ is the fluid density, p_s is the supply

pressure, p_{return} is the constant return pressure applied, and A_2 is the area of fluid outlet through the top of the actuator.

For retraction of the piston for the case that the actuators are not under external finger force, the following equations hold.

$$q_1 = c_{d,1} w x_v \sqrt{\frac{2}{\rho}} (p_1) \quad (4.6)$$

$$q_2 = c_{d,2} A_2 \cdot \text{sgn}(p_{\text{return}} - p_2) \sqrt{\frac{2}{\rho} |p_{\text{return}} - p_2|} \quad (4.7)$$

When the user is exerting some external force on the actuator piston, the following equations will hold,

$$q_1 = c_{d,1} w x_v \cdot \text{sgn}(p_1 - p_s) \sqrt{\frac{2}{\rho} |p_1 - p_s|} \quad (4.8)$$

$$q_2 = c_{d,2} A_2 \cdot \text{sgn}(p_{\text{external}} + p_{\text{return}} - p_2) \sqrt{\frac{2}{\rho} |p_{\text{external}} + p_{\text{return}} - p_2|} \quad (4.9)$$

when forcing fluid out of the valve, ($p_1 > p_s$). The solenoid valves are still open and allowing flow in. The return pressure is always constant while the orifice area is just the area of the cylinder where the fluid enters/exits. As there is only one valve controlled, only the flow in through the bottom of the actuator via the solenoid valve has variable orifice area. The top of the actuator has constant area, A_2 where the fluid exits and sucked out by a pump to the drain. The relationship between the solenoid valve spool position, x_v to voltage input, $u(t)$ is approximated by the 1st order differential equation,

$$\frac{dx_v}{dt} = -\frac{x_v}{\tau} + \frac{K_v}{\tau} u(t) \quad (4.10)$$

where τ is the valve time constant and K_v is the valve gain. The fluid continuity equations relating fluid flow to pressure in the cylinder are given by,

$$q_1 = A_1 \frac{dy}{dt} + \frac{V_1}{\beta_1} \frac{dp_1}{dt} + C_{\text{leak},1} \cdot p_1 \quad (4.11)$$

$$q_2 = A_2 \frac{dy}{dt} - \frac{V_2}{\beta_2} \frac{dp_2}{dt} + C_{\text{leak},2} \cdot p_2 \quad (4.12)$$

where β_1 is the effective bulk modulus of the fluid in the bottom of the cylinder and the working chamber of the control adapter and V_1 is the average volume trapped in the bottom side of the cylinder. The value of β_1 depends on the bulk modulus of the working fluid from manufacturer's data, β_f and the fluid bulk modulus due to the control adapter compliance, β_c ; and can be approximated by,

$$\frac{1}{\beta_1} = \frac{1}{\beta_f} + \frac{1}{\beta_c} \quad (4.13)$$

This equation assumes that there is negligible amount of air trapped inside the cylinder. Similarly, β_2 is the effective fluid bulk modulus of the fluid in the top of the cylinder and V_2 is the average volume trapped in the top part of the cylinder. However, in this case, it

will be assumed that $\beta_2 = \beta_f$ as there is no deformable boundary present. From the equations above, the fluid capacitances at the bottom side and the top side of the cylinder can be denoted by $C_1 = V_1/\beta_1$ and $C_2 = V_2/\beta_2$ respectively. In the case where the deformation of the control adapter membrane is not taken into account, $\beta_1 = \beta_f$. And if the average volume in the cylinder, \bar{V} is used, the fluid capacitance for the “stiff” model is given by

$$C = \frac{\bar{V}}{\beta_f} \quad (4.14)$$

Fluid leakage is approximated by the coefficients $C_{\text{leak},1}$ and $C_{\text{leak},2}$ and has unit of flow rate per unit pressure. The extending velocity and flow into side 1 and out of side 2 are termed positive.

To apply linear analysis to the model, the nonlinear flow equations need to be linearized. By linearizing the nonlinear valve flow equations, only one steady state values to another can be approximated. The assumption is that the change in between two instances is not too remote. For the fluid flow through an orifice equation, the linearized equations following application of Taylor series expansion theory and neglecting higher order terms, are given as:

$$q_1 = K_f^1 x_v - K_p^1 p_1 \quad (4.15)$$

$$q_2 = K_f^2 + K_p^2 p_2 \quad (4.16)$$

where the two K_f are the flow sensitivity constant and the two K_p are the pressure sensitivity constants. The coefficients evaluated at steady state conditions are given, for when the piston is extending, not under external finger force,

$$K_f^1 = c_{d,1} w \cdot \text{sgn}(p_s - p_1) \sqrt{\frac{2}{\rho} |p_s - p_1|} \quad (4.17)$$

$$K_f^2 = c_{d,2} A_2 \cdot \text{sgn}(p_2 - p_{return}) \sqrt{\frac{2}{\rho} |p_2 - p_{return}|} \quad (4.18)$$

$$K_p^1 = \frac{\text{sgn}(p_s - p_1) c_{d,1} A_{orifice}}{\sqrt{2\rho |p_s - p_1|}} \quad (4.19)$$

$$K_p^2 = \frac{\text{sgn}(p_2 - p_{return}) c_{d,2} A_2}{\sqrt{2\rho |p_2 - p_{return}|}} \quad (4.20)$$

and for when the piston is retraction, not under external finger force,

$$K_f^1 = c_d w \sqrt{\frac{2}{\rho} (p_1)} \quad (4.21)$$

$$K_f^2 = c_{d,2} A_2 \cdot \text{sgn}(p_{return} - p_2) \sqrt{\frac{2}{\rho} |p_{return} - p_2|} \quad (4.22)$$

$$K_p^1 = \frac{c_d A_{orifice}}{\sqrt{2\rho \cdot (p_1)}} \quad (4.23)$$

$$K_p^2 = \frac{\text{sgn}(p_{return} - p_2) c_{d,2} A_2}{\sqrt{2\rho |p_{return} - p_2|}} \quad (4.24)$$

assuming $p_{atm} = 0$, and for retraction, when finger is pushing on the actuator, forcing fluid out, ($P_1 > P_s$).

$$K_f^1 = c_{d,1} w \cdot \text{sgn}(p_1 - p_s) \sqrt{\frac{2}{\rho} |p_1 - p_s|} \quad (4.25)$$

$$K_f^2 = c_{d,2} A_2 \cdot \text{sgn}(p_{external} + p_{return} - p_2) \sqrt{\frac{2}{\rho} |p_{external} + p_{return} - p_2|} \quad (4.26)$$

$$K_p^1 = \frac{\text{sgn}(p_1 - p_s) c_{d,1} A_{orifice}}{\sqrt{2\rho |p_1 - p_s|}} \quad (4.27)$$

$$K_p^2 = \frac{\text{sgn}(p_{external} + p_{return} - p_2) c_{d,2} A_2}{\sqrt{2\rho |p_{external} + p_{return} - p_2|}} \quad (4.28)$$

Putting all the equations together, a state space representation of the single Digital Clay hydraulic actuator system can be derived. Let the states be the piston velocity \dot{y} and both cylinder pressures p_1 and p_2 . The known input applied to the solenoid valves $u(t)$, the unknown input, that is the unknown disturbance force, F_d and let the measured output be the piston velocity estimated from Chapter 2.

$$\ddot{y} = -\frac{b}{m} \dot{y} + \frac{A_1}{m} p_1 - \frac{A_2}{m} p_2 - \frac{F_d}{m} \quad (4.29)$$

$$\dot{p}_1 = -\frac{A_1}{C} \dot{y} - \text{sgn}(\dot{y}) \frac{K_p^1}{C} p_1 - \frac{C_{leak,1}}{C} \cdot p_1 + \text{sgn}(\dot{y}) \frac{K_f^1}{C} x_v \quad (4.30)$$

$$\dot{p}_2 = \frac{A_2}{C} \dot{y} - \text{sgn}(\dot{y}) \frac{K_p^2}{C} p_2 - \frac{C_{leak,2}}{C} \cdot p_2 - \text{sgn}(\dot{y}) \frac{K_f^2}{C} \quad (4.31)$$

$$\dot{x}_v = \left(-\frac{1}{\tau}\right)x_v + \left(\frac{k_v}{\tau}\right)u \quad (4.32)$$

$$\begin{bmatrix} \ddot{y} \\ \dot{p}_1 \\ \dot{p}_2 \end{bmatrix} = \begin{bmatrix} -b/m & A_1/m & -A_2/m \\ -A_1/C & -(K_p^1 + C_{leak,1})/C & 0 \\ A_2/C & 0 & -(K_p^2 + C_{leak,2})/C \end{bmatrix} \cdot \begin{bmatrix} \dot{y} \\ p_1 \\ p_2 \end{bmatrix} + \begin{bmatrix} 0 \\ K_{f,1}/C \\ 0 \end{bmatrix} \cdot x_v + \begin{bmatrix} -\frac{1}{m} \\ 0 \\ 0 \end{bmatrix} \cdot F_d \quad (4.33)$$

To determine the parameters for model verification and simulation, several experiments have to be performed. For measurable parameters such as the cylinder areas, mass of the piston pin and brass rod, supply pressure and return pressure, obtaining the numerical values is straightforward and fairly accurate. The actuator damping coefficient is estimated by taking the ratio of known force applied and average velocity that it travels under the force. The fluid properties, valve coefficient of discharge, time constant and gain factor are estimated from manufacturer's data. Coefficient of discharge for top of cylinder opening is estimated by performing a flow test. Figure 4.4 shows the flow rate of the valve as a function of PWM duty ratio with base frequency of 100Hz and pressure drop across the valve is 25psi. Consequently, flow and pressure sensitivity coefficients are calculated. The nominal parameters used for initial simulation is summarized in Table 4.2.

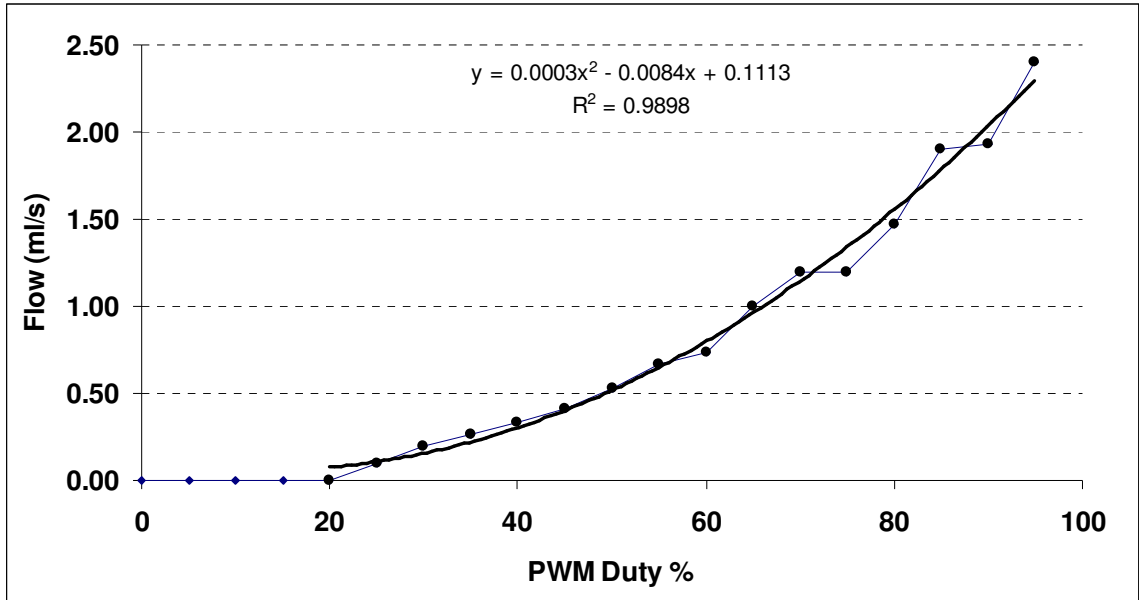


Figure 4.4 Flow Rate vs. PWM Duty Ratio Experiment for Solenoid Valve

To verify that the model parameters are indeed accurate and able to capture the behavior of the actual system, a simulation is performed. The simulation is performed in MATLAB Simulink and the block diagram is shown in Figure 4.5. The input PWM duty applied to the model is from the actual proportional controller of the system to track a sine wave displacement. Valve saturation and dead band were also taken into account in the simulation. From Figure 4.4, the dead band of the valve is around 20% duty ratio while saturation is set to 95% duty ratio.

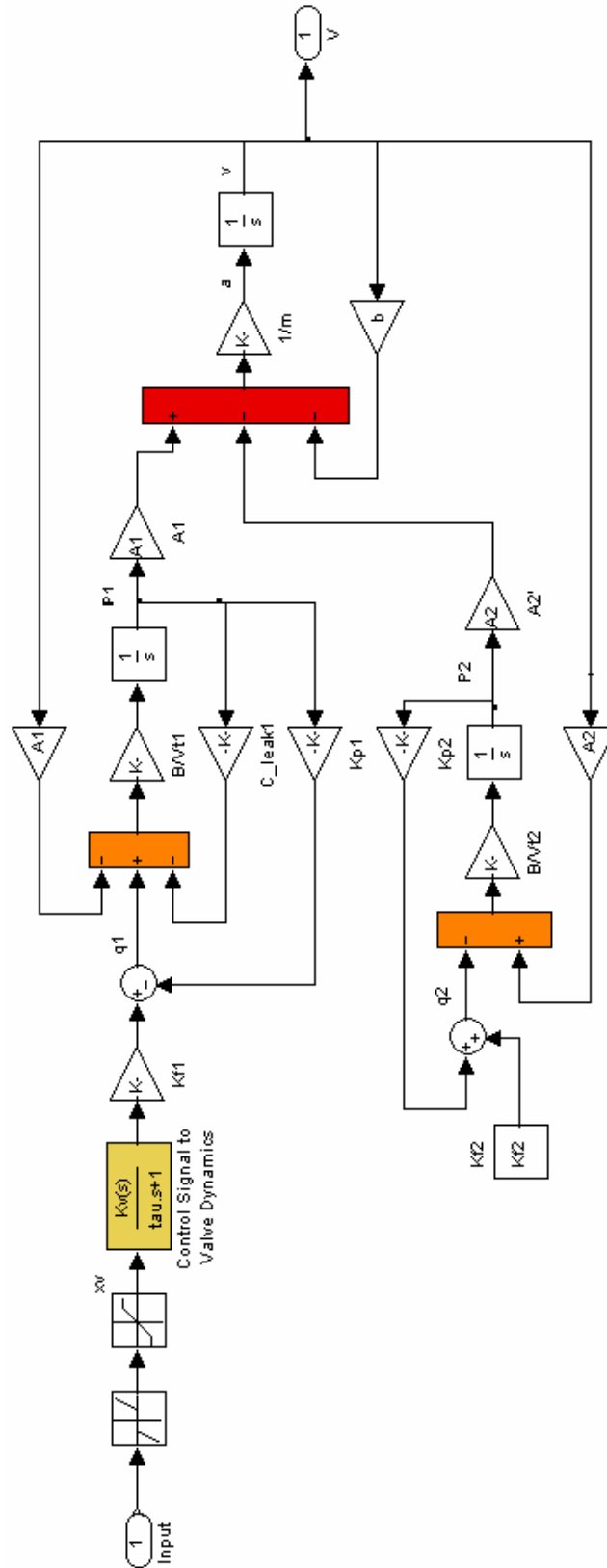


Figure 4.5 MATLAB Simulink Simulation Block Diagram

In Figure 4.6, the simulated velocity is plotted together with the measured actuator velocity. The initial parameters used to simulate the model clearly do not match the system actual behavior. It is therefore necessary to change some of the linearized parameters so that the system actual behavior can be modeled. In particular, the flow and pressure sensitivity coefficients K_f and K_p are linearized and could well be far from being the most appropriate for the model initially.

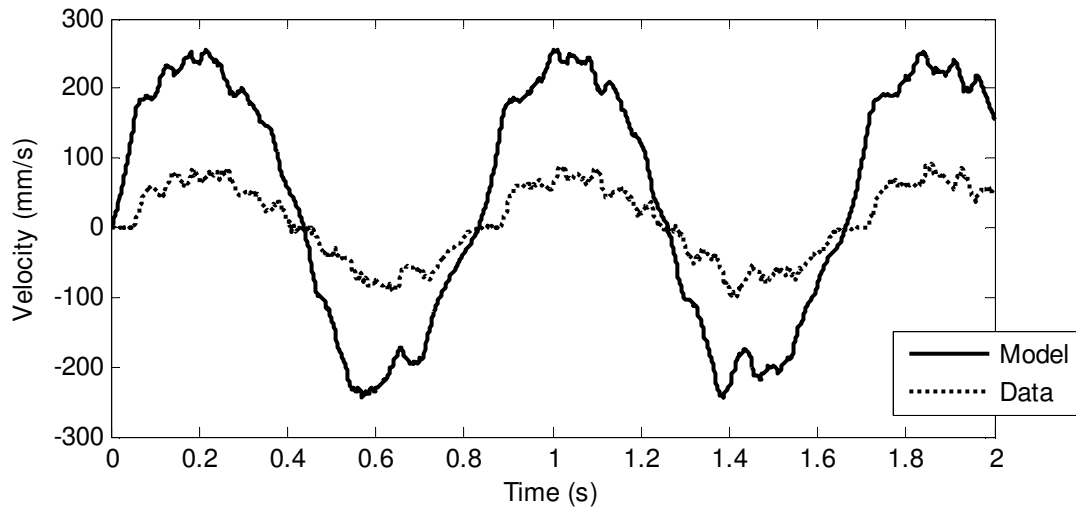


Figure 4.6 Experimental and Simulated (Initial Parameters) Sine Wave Velocity

To perform this task, the Matlab parameter estimation tool is employed such that the nonlinear least squares cost function is minimized. During this task, the program will iterate the parameters of interest such that the output of the model matches the actual system output. The closer the model output is to the actual system output, the lower the cost function will become. As mentioned, only the flow and pressure sensitivity coefficients K_f and K_p are fine-tuned to minimize the cost function. All other parameters are deemed more correct and therefore left unchanged. After 27 iterations, the

cost function was reduced from $2.985e7$ to $1.516e5$; a two order of magnitude improvement. Figure 4.7 shows the new model output as compared to actual system output and the updated parameters are listed in Table 4.2.

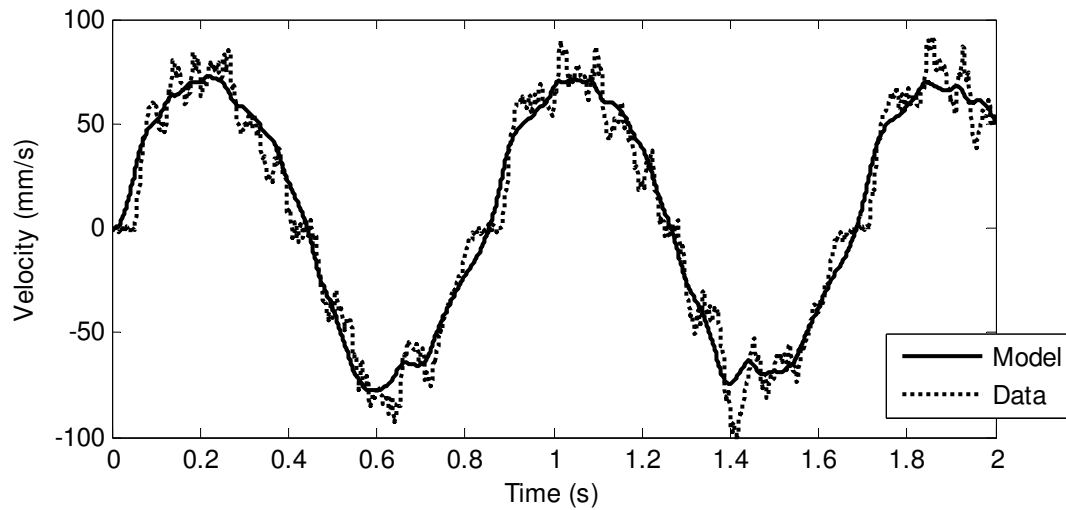


Figure 4.7 Experimental and Simulated (Model) Sine Wave Velocity

Figure 4.8 and Figure 4.9 show the model output compared to the actual response for both a square and a sine wave displacement tracking.

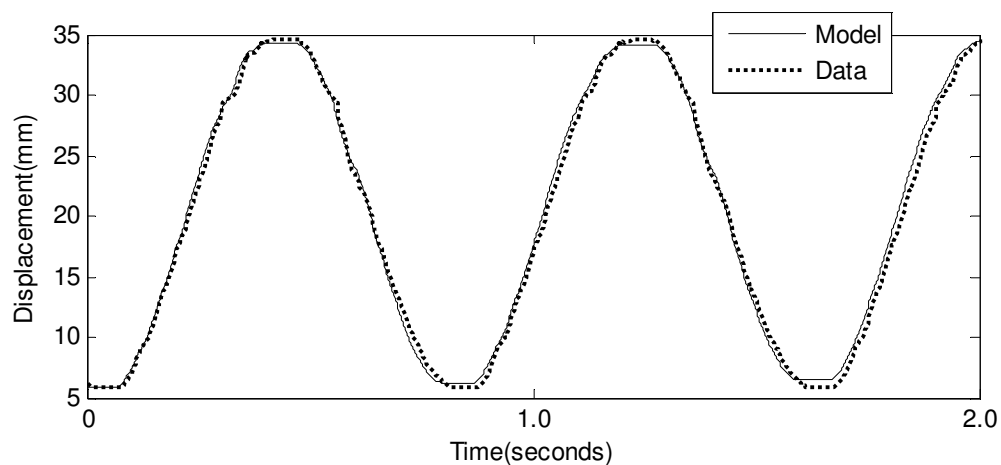


Figure 4.8 Experimental and Simulated (Model) Sine Wave Displacement Tracking

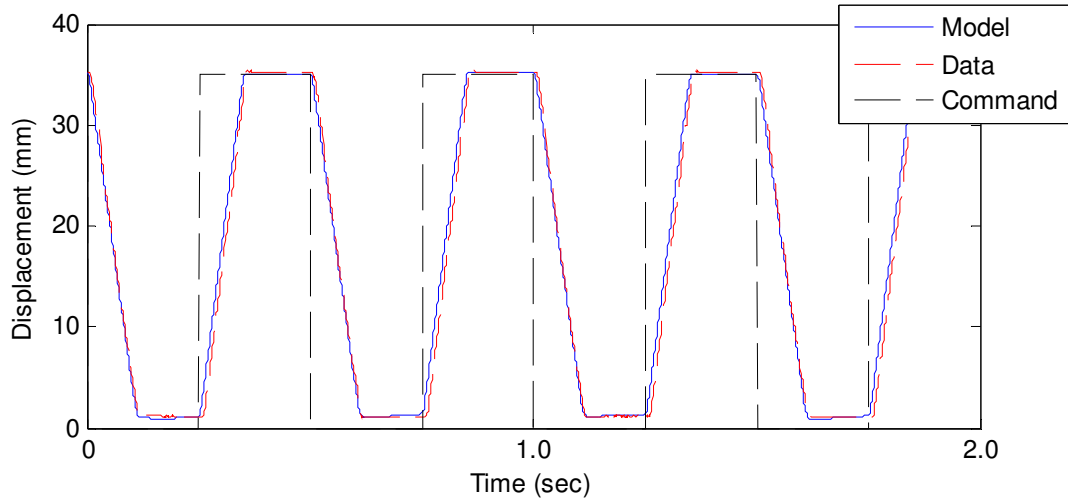


Figure 4.9 Experimental and Simulated (Model) Square Wave Displacement Tracking

Table 4.2 Digital Clay Single Actuator Parameters

| Parameters | Description | Initial Values | Fitted Values |
|---------------|--|--|--|
| k | Environmental Stiffness | Unknown | Unknown |
| A_1 | Piston area 1 | 8.143 mm ² | 8.143 mm ² |
| A_2 | Piston area 2 | 6.88 mm ² | 6.88 mm ² |
| m | Brass rod + piston mass | 0.01445 kg | 0.01445 kg |
| b | Estimated damping factor | 27 N/m/s | 27 N/m/s |
| β_f | Silicon oil bulk modulus | 9.58x10 ⁸ Pa | 9.58x10 ⁸ Pa |
| \bar{V} | Average fluid volume in cylinder | 4 x10 ⁻⁶ m ³ | 4 x10 ⁻⁶ m ³ |
| C | Effective capacitance | 4.3x10 ⁻¹⁵ m ³ /Pa | 4.3x10 ⁻¹⁵ m ³ /Pa |
| C_{leak} | Leakage coefficient | 3.7x10 ⁻¹² m ³ /Pa.s | 3.7x10 ⁻¹² m ³ /Pa.s |
| $c_{d,1}$ | LEE co. valve coefficient of discharge | 0.27 | 0.27 |
| $c_{d,2}$ | Top opening coefficient of discharge | 0.5 | 0.5 |
| $A_{orifice}$ | LEE co. valve orifice area | 9.6842x10 ⁻⁷ m | 9.6842x10 ⁻⁷ m |
| w | LEE co. valve orifice opening gradient | 0.000927 m | 0.000927 m |
| $K_{f,1}$ | Nominal flow sensitivity factor 1 | 0.003446 m ³ /Pa.s | 0.001064 m ³ /Pa.s |
| $K_{f,2}$ | Nominal flow sensitivity factor 2 | 3.45x10 ⁻⁵ m ³ /Pa.s | -0.00233 m ³ /Pa.s |
| K_p^1 | Nominal pressure sensitivity factor 1 | 2.295x10 ⁻¹¹ m ² /s | 9.7248x10⁻¹¹ m ² /s |
| K_p^2 | Nominal pressure sensitivity factor 2 | 5.00x10 ⁻¹⁰ m ² /s | 4.6135x10⁻⁹ m ² /s |
| τ | Valve time constant | 5.0 ms | 5.0 ms |
| K_v | Valve gain factor | 0.00012 m/V | 0.00012 m/V |
| p_s | Supply pressure | 25 psi (172.4 kPa) | 25 psi (172.4 kPa) |
| p_{return} | Return pressure | 10 psi (68.9 kPa) | 10 psi (68.9 kPa) |

As a side note, the model of the system will be significantly altered when the effective bulk modulus of the fluid takes into account deformation of the control adapter membrane. There has not been much work done previously on analytically determining the value of fluid bulk modulus due to the environment other than to experimentally measure the value. However there have been results on determining fluid bulk modulus contained in a cylindrical container with a thin wall. In the case of the single actuator system, the control adapter wall is much stiffer compared to the membrane and therefore the formula is not applicable. Analytically analyzing Equation 4.13, it can be concluded that $\beta_c \ll \beta_f$ by several magnitudes and thus the fluid effective modulus in the bottom part of the cylinder β_1 can be approximated by β_c . This implies that the cylinder volume change is mostly due to the compliance of the membrane and the pressure inside the cylinder is too small to cause any significant compressibility of the fluid. And from before, $\beta_2 = \beta_f$. Thus the fluid capacitance in both compartments of the cylinder can be written as,

$$C_1 = \frac{\bar{V}}{\beta_c}, \quad C_2 = \frac{\bar{V}}{\beta_f} \approx 0 \quad (4.34)$$

since \bar{V} is much smaller than β_f . Basically the assumption drawn here is that for the operational range of Digital Clay, the working fluid has no compressibility effect, and the fluid capacitance is only due to the compliance of the control adapter membrane. From

Equation 4.12, $\frac{V_2}{\beta_2} \frac{dp_2}{dt} \approx 0$ and Equation 4.31 can be eliminated from the system of equations. Hence the system model is reduced to a 2nd order state space equation,

$$\begin{bmatrix} \ddot{y} \\ \dot{p}_1 \end{bmatrix} = \begin{bmatrix} -b/m & A^1/m \\ -A_1/C_1 & -(K_p^1 + C_{leak,1})/C_1 \end{bmatrix} \cdot \begin{bmatrix} \dot{y} \\ p_1 \end{bmatrix} + \begin{bmatrix} 0 \\ K_{f,1}/C_1 \end{bmatrix} \cdot x_v + \begin{bmatrix} -1/m \\ 0 \end{bmatrix} \cdot F_d' \quad (4.35)$$

where the new unknown input or disturbance force term is defined by,

$$F_d' = F_{\text{reaction}} + \text{sgn}(\dot{y}) \cdot f_{\text{coulombic}} + mg + A_2 p_2 \quad (4.36)$$

The return pressure, p_2 is then a constant value and the steady state flow equation is satisfied by $q_2 = A_2 \dot{y} + C_{leak,2} \cdot p_2$. This new model can be used to construct a lower order observer to reduce computational load. However as will be shown in the next chapter, the full order observer is implemented without sacrificing too much computational load.

4.4 Remarks and Discussion

In this chapter, a model of the Digital Clay single actuator system is derived. First, the frequency response of the system is investigated. From the Bode magnitude plot, the Digital Clay single actuator plant has a bandwidth of 8Hz. Then, a third order “stiff” model is derived from differential equations commonly used in describing hydraulic behaviors. The compliance of the control adapter membrane is not taken into account. However the model can be reduced to a second order model if the membrane compliance is taken into account. It was found that the model output agrees well with actual experimental output even with linearized coefficients. The explanation is that nonlinear effects such as actuator stiction, fluid compressibility and flow-pressure nonlinearities are small within the operating range of this device. Furthermore in performing input-output experiments, fluid leakage and other coupling effects from adjacent actuators are non-existent. This knowledge serves as a margin for using linear models to represent the system dynamics and also as a caution that linear assumptions will fail in the presence of these effects. This result provides great confidence in using the linearized parameters in the mathematical model for designing force observers in the next chapter. The model needs to estimate internal states of the system as the only measured output is the displacement of the actuator. This is an extremely difficult task as hydraulic systems are highly non-linear and linearization only provides good estimates for very small working range. In the next chapter, two types of observers will be designed to estimate the force exerted on the actuator.

CHAPTER 5 MODEL BASED FORCE ESTIMATION

For the application of Digital Clay, the use of force/pressure sensor in every actuator is not considered the best option to keep the overall cost and hardware complexity at the minimum. This creates a challenge to estimate the force exerted on the actuator without force/pressure sensor present. Zhu developed a pressure sensor array system to measure cylinder pressure, but the sensor array requires one sensor for each actuator which inevitably adds to the cost and complexity of not only to the structure but also to the software. Furthermore, the current 5x5 prototype does not have that sensor array embedded, which motivates this research and study on sensorless force estimation. Fortunately in control theory, estimator (or observer) is widely used in estimating unmeasured states and in feedback control of dynamical systems. It is a field that is widely researched and has achieved much success in practical real-world applications. From Franklin [36], an observer or an estimator is used to estimate unmeasurable state variables of a system from available input and output measurements. A mathematical model of the plant of interest is used to construct an observer. To ensure that the estimation tracks the actual plant behavior, the observer error is defined as $e = x - \hat{x}$. Where x is the actual state variable while \hat{x} is the estimated state variable. The mathematical model is compensated with the observer error to ensure that the error dynamics converge to zero. Figure 5.1 graphically explains a state observer developed by Luenberger in 1966 [37].

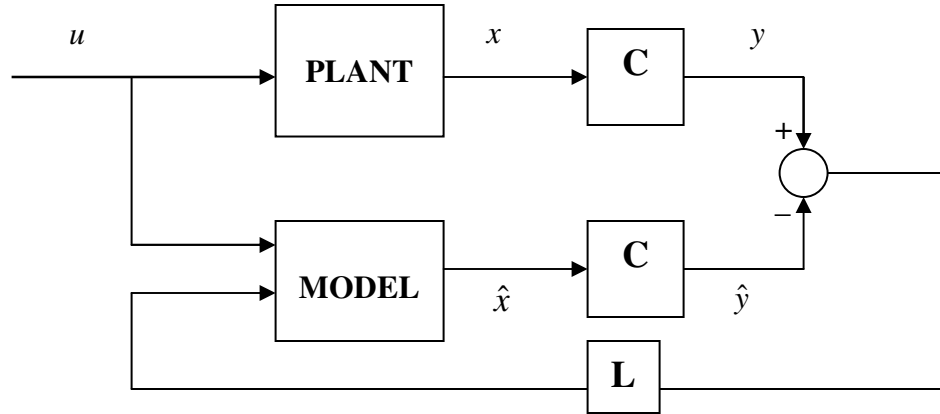


Figure 5.1 Block Diagram of a Luenberger State Observer

From Figure 5.1, u is the input matrix, x is the actual state variable matrix, \hat{x} is the estimated state variable matrix, y is the actual output and \hat{y} is the estimated output. The gain matrix \mathbf{L} can be chosen so that the observer error dynamic is stable and converges as fast as possible. Mathematically, consider the plant to have the following state space representation,

$$\begin{aligned}\dot{x} &= Ax + Bu \\ y &= Cx\end{aligned}\tag{5.1}$$

where \mathbf{A} is the state matrix, \mathbf{B} is the input matrix and \mathbf{C} is the output matrix. The observer for the system is given by,

$$\dot{\hat{x}} = A\hat{x} + Bu + L(y - C\hat{x})\tag{5.2}$$

and the observer error dynamic equation is

$$\dot{e} = (A - LC)e \quad (5.3)$$

If the error matrix $(A - LC)$ is stable, i.e. with all the poles (or eigenvalues) in the right half plane, the observer error will converge to zero and the estimated states will converge to the actual states.

5.1 Previous Work on Sensorless Force Estimation

There has been much research done on sensorless force estimation and control in the past, but mainly on robotic applications and some on pneumatic systems but very little on hydraulic systems. One of the earlier works on robotic applications was done by Salcudean and Hacksel [38] on observer-based determination of environment forces acting on a rigid body of a manipulator. An accurate model of the plant was needed for the observer designed. The manipulator position, actuator force and torque information were assumed known and the observer error dynamics were considered as a mass damper spring model driven by the environmental forces. Although the environmental forces can be estimated accurately, full knowledge of the model was needed, i.e. small error in mass parameters and an absence of unmodeled dynamics. Typically, this information is not accurately known and it is almost impossible to obtain an accurate model in real applications without any uncertainties.

Ohishi [39][40][41] designed an acceleration controller and a force observer on robotic manipulator based on the mixed sensitivity H_∞ method. A torque observer is first

used to estimate disturbance force on the actuator. The disturbance force is the sum of the reaction force, frictional force, pay-load torque and gravity effect. Inertial effect was assumed to be small and negligible. Then the reaction force is estimated by subtracting the remaining forces from the disturbance force. The gravitational force and pay-load force is assumed to be known a-priori while the friction force is estimated from a coulomb friction model. A sensorless force control was then designed from the environmental reaction force estimate. The force response without force sensor was comparable to force response with actual force sensor. This is an example of using disturbance controller to estimate the reaction force, which is not the detrimental disturbance to be cancelled.

A number of other works on force control without sensors were also based on disturbance observer method and are fundamentally similar to the work of Ohishi except for some modifications and/or improvements of algorithm. Ahn et al. [42] designed a disturbance observer using the information from deviation of the system from a nominal model for an automatic live-line maintenance robot with H_∞ method.

Katsura et al. [43] developed a disturbance observer based force control to achieve stable contact of a robot with the environment. It was shown that stable contact with the environment is difficult when there is variation in the stiffness of the environment and the soft contact characteristic of the force sensor. There is also the limited bandwidth (due to low-pass filtering) of a force sensor to cover all situations. To solve this problem, a disturbance observer was designed to cancel the disturbance torque as rapidly as possible and a reaction torque observer was designed to estimate the contact force. The reaction torque observer is based on the disturbance observer technique. By assuming that the

disturbance torque is due to the contact force, similar to Ohishi, the reaction torque observer can estimate robot contact force with the environment. Simulation and experimental results show a wide bandwidth of force sensing and stable force response attained even with high environmental stiffness variation.

For application to pneumatic and hydraulic actuators, using observers to estimate the states of the system is not as straight forward and as linear as the relationship between actuator input and force for a DC or servo motor. The highly non-linear and uncertain dynamics of such fluid systems will require advanced/ more complex methods to estimate all the states and overcome non-linearity. Gulati and Barth [44] presented two Lyapunov-based pressure observers for a pneumatic system. The first observer was developed using an energy-based Lyapunov function while the second was developed using a force-based Lyapunov function. The actuator cylinder pressures were estimated based on states of the system. The Lyapunov functions are chosen such that the estimated pressures will converge to the actual pressures. From experimental results, the observed pressures converged sufficiently fast to actual pressures but there remained a small error. The measured mass flow rates did not include the dependency on orifice size but rather an average value of discharge coefficient. Frictional effect was also neglected.

Koontz [45] developed a pressure observer for estimating the aortic blood pressure of the Penn State Electric Ventricular Assist Device (EVAD). The electric motor voltage and pusher plate position are known inputs and outputs respectively. The observer is based on a state space Luenberger observer method. System parameters had to be determined to construct a model. The observer gains are determined using optimal

control theory. The estimated pressure is used in feedback control of the beat of the device.

In a more related work, Hahn [46] developed estimation algorithm for the output pressure of a vehicle power transmission hydraulic actuator based on a robust non-linear observer setup. With only control input, measured slip velocity and empirical model of the system dynamics, the hardware-in-loop (HIL) simulation result showed satisfactory pressure estimation. However, the observer was only tested for small variations in operation conditions and uncertainties involving the modeling error, not for a significant disturbance involving reaction force.

Kashi and Soffker [47] developed a force and displacement model-based observer for a single-rod hydraulic cylinder. The application was for the Active Suspension Control System (ASCS) developed by TRW Automotive Inc. The different piston areas, unmeasurable friction between piston and cylinder housing and non-linear fluid behavior makes the design of an observer more challenging. Similar to Digital Clay, many parameters are uncertain and not measurable. The external reaction force is the desired variable but as discussed previously, is either not measurable directly or there does not exist a good way to obtain the value. The authors introduced the use of a Proportional-Integral observer to overcome the issues with uncertainties and non-linearity. The only difference with a conventional Luenberger observer is the inclusion of integral observer error together with proportional observer error. The observer inputs are the flow rates in and out of the cylinder; which are calculated forward from system supply pressure and valve input voltage along with pressures in the cylinder. Both of the cylinder pressures are available by measurements. The observer output is the actuator displacement and

force. Although the actuator force was estimated with good accuracy, the use of such large number of pressure sensors for Digital Clay is not a very cost effective or simple solution. It is therefore desirable to be able to extend the works of the above mentioned authors to develop a suitable force estimation method for Digital Clay.

5.2 Open Loop Force Estimation

The first experiment performed was to study the behavior of Digital Clay actuator force dynamic behavior. Since we are interested in force estimation, the experiment was carried out to see the behavior of actuator force in both dynamic and static condition for the purpose of force display without a force sensor. This simple study only serves as a starting point for further work. For the dynamic force experiment, the set up in Figure 5.2 was used.

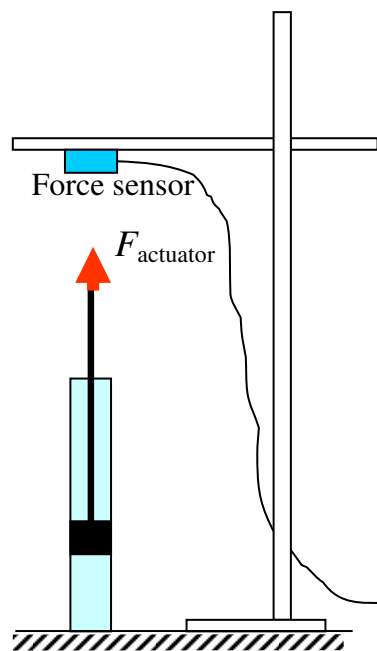


Figure 5.2 Duty Ratio vs. Dynamic Force Experiment

. The height of the rigid platform where the force sensor is attached to is 10mm above the zero position of an actuator. The input duty ratio was varied from 20% to 90% and the dynamic force is measured with a 0-1 lbf (4.4N) dynamic force sensor from *PCB Electronics Inc.* A total of five measurements are taken for each input. The duty ratio is the input and this experiment will allow us to see its relationship with the average dynamic force. Table 5.1 shows the reading obtained from the force sensor. The output is in milliVolts (mV) and the sensitivity of the sensor is 2379 mV/lbf or 535 mV/N. Five readings were taken for each duty ratio and the average voltage is converted to equivalent force unit.

Table 5.1 Average Dynamic Actuator Force Compared to Duty Ratio

| PWM Duty(%) | Sensor reading (mV) | | | | | Average (mV) | Force (N) |
|--------------------|----------------------------|------|------|------|------|---------------------|------------------|
| 20 | 260 | 246 | 262 | 268 | 254 | 258 | 0.48 |
| 30 | 548 | 558 | 438 | 434 | 464 | 488 | 0.91 |
| 40 | 678 | 792 | 670 | 816 | 824 | 756 | 1.41 |
| 50 | 860 | 808 | 856 | 870 | 750 | 829 | 1.55 |
| 60 | 1180 | 1200 | 1070 | 900 | 1110 | 1092 | 2.04 |
| 70 | 1040 | 1350 | 1330 | 1390 | 1280 | 1278 | 2.39 |
| 80 | 1560 | 1310 | 1290 | 1320 | 1290 | 1354 | 2.53 |
| 90 | 1530 | 1550 | 1670 | 1690 | 1650 | 1618 | 3.03 |

Figure 5.3 shows the plot of actuator dynamic force with respect to duty ratio. The relationship was surprisingly linear and has a goodness of fit close to unity. The same set up as Figure 5.2 was used to study the static force relationship with duty ratio but the actuator was allowed soft contact with the force sensor before increasing the duty ratio. This time, a force sensing resistor from *TekScan Inc.* was used to measure the static force.

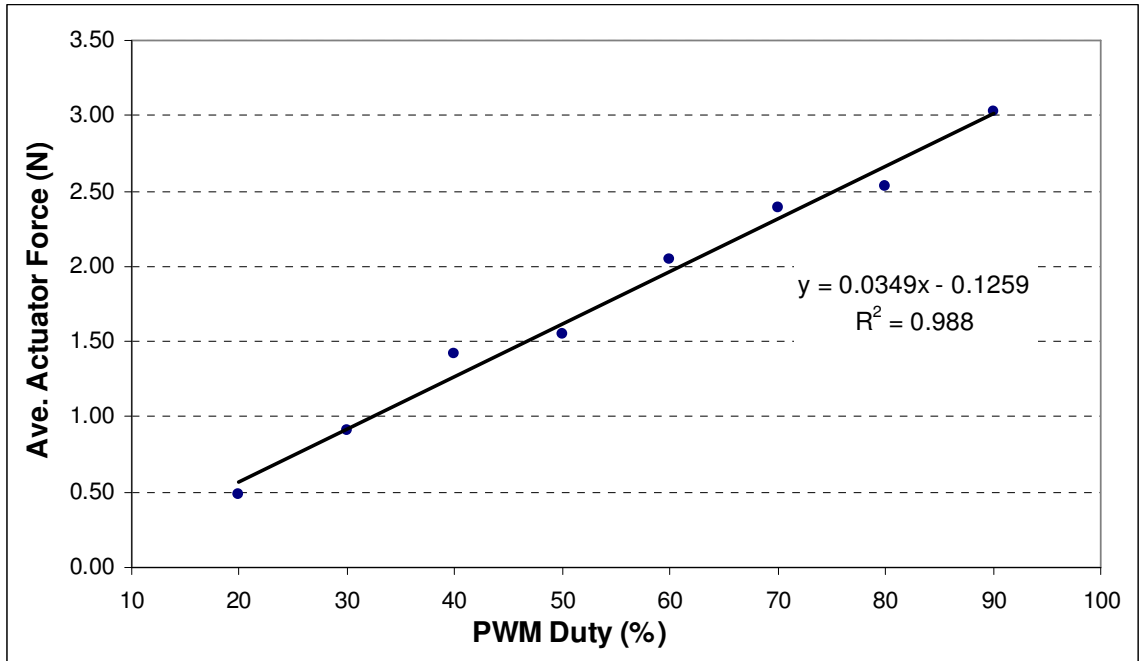


Figure 5.3 Actuator Dynamic Force as a Function of Duty Ratio

Figure 5.4 shows the force sensor output and duty ratio as the experiment was performed. Since it was a continuous experiment, the duty ratio was first set to 15% for the pin to contact the force sensor. Then the duty ratio was set to the desired value for this experiment before a duty ratio of 20% in the opposite direction was applied for the pin to remove contact (retract). Figure 5.5 plots the average static force with respect to duty ratio. As expected, the average force across duty ratio remained almost constant as the supply pressure builds up in the actuator when a stop is encountered. For 20% and 30% duty ratio, the actuator force was still rising when commanded to retract. This is due to small flow rate hence the slow response. However, it is clear that the actuator force will reach a steady state value corresponding to the maximum supply pressure.

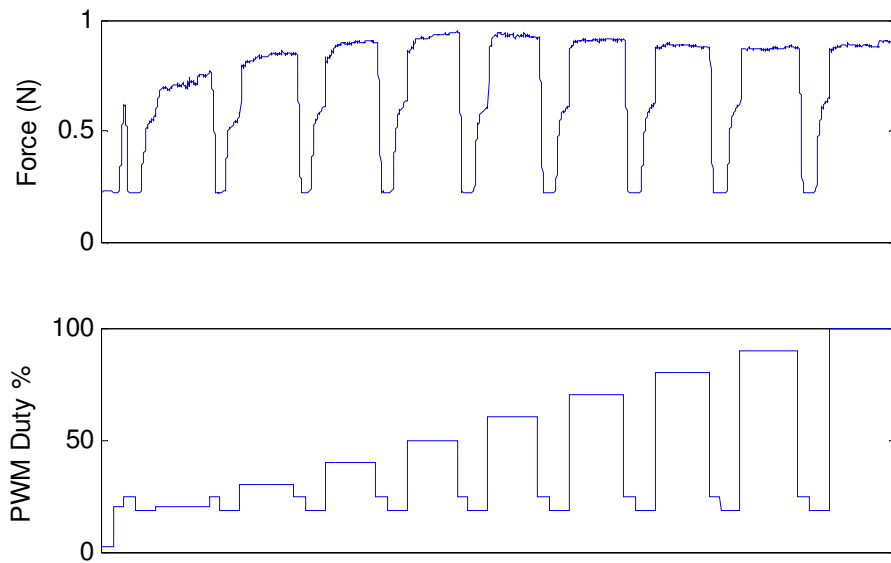


Figure 5.4 Static Force Experiment With Respect to Duty Ratio

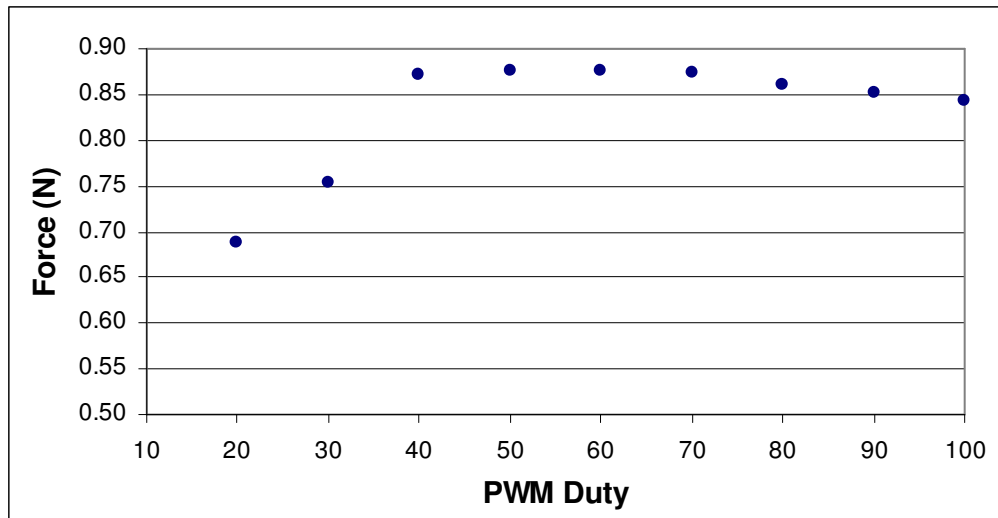


Figure 5.5 Relationship Between Actuator Static Force and Duty Ratio

From the results of the two experiments, it can be concluded that the average actuator dynamic force is linear with respect to duty ratio or input flow. More importantly, actuator static force cannot be estimated by linearized observer method as

the system input is only duty ratio of the valve and no pressure sensor is present. This is the fundamental physical limitation that will be discussed further at the end of the chapter.

5.3 Proportional Integral Observer

The conventional Luenberger observer from (5.2) depends on the model of the system to estimate unmeasured states. For Digital Clay, the measured output is displacement and the variable to be estimated is the external force from user. However as modeled in (4.3) in Chapter 4, the external force is not explicitly a state variable but modeled as part of an unknown input, F_d . Recall from previous chapter that $F_d = F_{\text{reaction}} + \text{sgn}(\dot{y}) \cdot f_{\text{coulombic}} + mg$. From Soffker and Kashi [47][48], a variation of the Luenberger observer called the Proportional Integral Observer (PIO) can be used to estimate unknown input.

Given the same linear system as in (5.4), that can be expressed as the following set of equations:

$$\begin{aligned} \dot{x} &= Ax + Bu + N \cdot f(x, u, t) \\ y &= Cx \end{aligned} \tag{5.4}$$

with a state vector, x of order n , input u , output y and system matrices, A, B and C . And if this system has an unknown input $f(x, u, t)$ that can be described by an unknown input matrix N , the PIO dynamics is given by:

$$\begin{aligned}\dot{\hat{x}} &= A\hat{x} + Bu + L_3\hat{f} + L_1(y - \hat{y}) \\ \hat{f} &= L_2(y - \hat{y})\end{aligned}\tag{5.5}$$

The estimated state matrix is \hat{x} while the estimated output is \hat{y} . The observer gains are L_1 , L_2 and L_3 and the estimated unknown input is \hat{f} . Basically the difference between the PIO dynamics and the Luenberger observer dynamics in (5.2) is the addition of an integral of estimation error term, which is the estimated unknown input, \hat{f} . Figure 5.6 shows the block diagram of the system as well as the PIO.

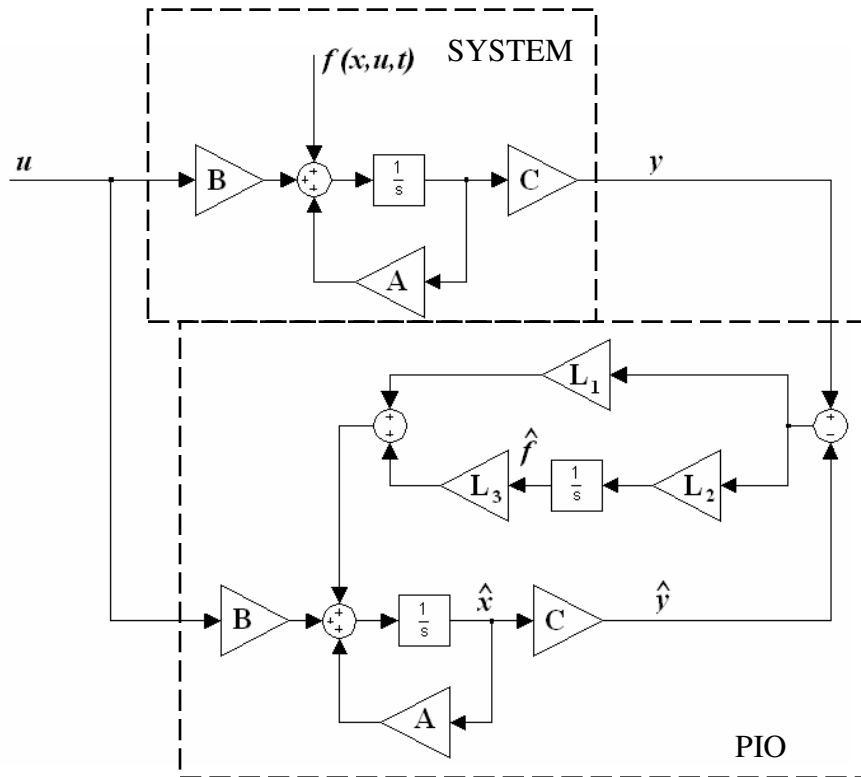


Figure 5.6 Block Diagram of Plant and Proportional Integral Observer (PIO)

From Soffker [48], the conditions for application of PIO to estimate the unknown input are outlined by the following three theorems.

Theorem 1: If the pair of (A, C) is observable, then there exists a PI observer for the system (5.4), such that, $\lim_{t \rightarrow \infty} [\hat{x}(t) - x(t)] = 0$ for any initial states $x(0)$, $\hat{x}(0)$ and $\hat{f}(0)$.

And if,

$$\text{rank} \left\{ \begin{bmatrix} sI - A & -L_3 \\ 0 & sI \\ C & 0 \end{bmatrix} \right\} = n + \dim(\hat{f}) \quad (5.6)$$

or equivalently,

$$\text{rank} \left\{ \begin{bmatrix} A & L_3 \\ 0 & 0 \end{bmatrix} \right\} = n + \dim(\hat{f}) \quad (5.7)$$

when $s = 0$, then the eigenvalues of the error dynamics matrix A_e can be arbitrarily placed by means of the gain matrices L_1 and L_2 to guarantee that $\lim_{t \rightarrow \infty} e(t) = 0$ and

$\lim_{t \rightarrow \infty} \hat{f}(t) = 0$ for any $e(0)$ and $\hat{f}(0)$.

Theorem 2: Assuming that $\lim_{t \rightarrow \infty} \hat{f}(x, u, t)$ exists, then there exists a PI observer for the system (5.4), such that $\lim_{t \rightarrow \infty} [\hat{x}(t) - x(t)] = 0$, for any initial states $x(0)$, $\hat{x}(0)$ and $\hat{f}(0)$

if (A, C) is observable and $\text{rank} \left\{ \begin{bmatrix} A & N \\ C & 0 \end{bmatrix} \right\} = n + r$. The order of $f(x, u, t)$ is r .

By letting $L_3 = N$, the eigenvalues of the error dynamics matrix A_e can be arbitrarily placed by means of the gain matrices L_1 and L_2 . The error dynamics matrix A_e is given by:

$$A_e = \begin{bmatrix} A - L_1 C & N \\ -L_2 C & 0 \end{bmatrix} \quad (5.8)$$

When the error dynamics $\begin{bmatrix} \dot{e} \\ \dot{\hat{f}} \end{bmatrix} = A_e \begin{bmatrix} e \\ \hat{f} \end{bmatrix} - \begin{bmatrix} 0 \\ I \end{bmatrix} f$ is asymptotically stable, its solution will converge to equilibrium, which is $\lim_{t \rightarrow \infty} [\hat{f}(t) - f(x, u, t)] = 0$ and $\lim_{t \rightarrow \infty} e(t) = 0$.

Theorem 3: Assume that $f(x, u, t)$ is bounded. Then there exists a high-gain PI observer for system (5.4) such that $\hat{x}(t) - x(t) \rightarrow 0$ ($t > 0$) for any initial states $x(0)$, $\hat{x}(0)$ and $\hat{f}(0)$ if,

(i) (A, C) is observable

$$(ii) \quad \text{rank} \left\{ \begin{bmatrix} A & N \\ C & 0 \end{bmatrix} \right\} = n + r \quad (5.9)$$

(iii) $CA^i N = 0$, $i = 0, 1, \dots, k - 2$, where k is the observability index of (A, C) , i.e. the least integer such that

$$\text{rank} \left\{ \begin{bmatrix} C \\ CA \\ \vdots \\ CA^{k-1} \end{bmatrix} \right\} = n \quad (5.10)$$

In the case of high-gains, \hat{x} and \hat{f} may approximate x and f . The matrix $L_3 = pN$ ($p > 1$) can be increased by using a large gain to avoid problems with computation of high gains for L_1 and L_2 .

5.3.1 Design Procedure

From the three theorems outlined in the previous section, the design procedure of the PIO is down to choosing the appropriate gains to minimize estimation error and that the observer has sufficiently fast dynamics and is stable. The following steps are guidelines:

1. Check that the pair of (A, C) is observable.
2. Check that $\text{rank} \left\{ \begin{bmatrix} A & N \\ C & 0 \end{bmatrix} \right\} = n + \dim(F_d)$
3. Let $L_3 = pN$ ($p > 1$)
4. Design observer gains L_1 and L_2 with pole-placement such that eigenvalues of A_e equals to the desired eigenvalues for the observer. This step could also be done iteratively by trial and error as designing controller gains.

The condition that number 4 above has to satisfy is that the error dynamics matrix,

$$A_e = \begin{bmatrix} A - L_1 C & N \\ -L_2 C & 0 \end{bmatrix} \text{ if and only if the pair } \left(\begin{bmatrix} A & N \\ 0 & 0 \end{bmatrix}; [C \ 0] \right) \text{ is observable.}$$

Subsequently, the error dynamics characteristic equation can be written as:

$$\det \left[sI - \left(\begin{bmatrix} A & N \\ 0 & 0 \end{bmatrix} - \begin{bmatrix} L_1 \\ L_2 \end{bmatrix} [C \ 0] \right) \right] = 0 \quad (5.11)$$

From the state space model of the Digital Clay single actuator, the state matrix is:

$$x = \begin{bmatrix} \dot{y} \\ p_1 \\ p_2 \end{bmatrix} \quad (5.12)$$

The system matrices A , B and C are:

$$A = \begin{bmatrix} -b/m & A_1/m & -A_2/m \\ -A_1/C & -(K_p^1 + C_{leak,1})/C & 0 \\ A_2/C & 0 & -(K_p^2 + C_{leak,2})/C \end{bmatrix} \quad (5.13)$$

$$B = \begin{bmatrix} 0 \\ K_f^1/C \\ 0 \end{bmatrix} \quad (5.14)$$

$$C = [1 \quad 0 \quad 0] \quad (5.15)$$

and the unknown input matrix, N is:

$$N = \begin{bmatrix} -\frac{1}{m} \\ 0 \\ 0 \end{bmatrix} \quad (5.16)$$

Using MATLAB function *obsv*(), the observability of the system can be found. Then using the function *rank*() to check the rank of the observability matrix found that it has full rank of three. Next, the rank of equation 5.9 has to be equal to four to satisfy condition 2 of the design procedure:

$$\text{rank} \left\{ \begin{bmatrix} A & N \\ C & 0 \end{bmatrix} \right\} = n + r = 3 + 1 \quad (5.17)$$

$$\text{rank} \begin{bmatrix} A & N \\ C & 0 \end{bmatrix} = \text{rank} \begin{bmatrix} -b/m & A_1/m & -A_2/m & -1/m \\ -A_1/C & -(K_p^1 + C_{\text{leak},1})/C & 0 & 0 \\ A_2/C & 0 & -(K_p^2 + C_{\text{leak},2})/C & 0 \\ 1 & 0 & 0 & 0 \end{bmatrix} = 4 \quad (5.18)$$

and it is clear that the matrix has rank equal to four. The number of independent measurements (order of y) has to be equal to or greater than the number of external inputs (order of $f(u,x,t)$). In this case, they are both one.

With the conditions from the three theorems satisfied, the PIO gains can be designed. First, by letting $L_3 = pN$ ($p > 1$) and then for the remaining two gains, the pole placement function in MATLAB, *acker*() based on the Ackermann's formula or *place*() can be used.

$$\begin{bmatrix} L_1 \\ L_2 \end{bmatrix} = \text{acker} \left(\begin{bmatrix} A & N \\ 0 & 0 \end{bmatrix}^T, [C \ 0]^T, p \right)^T \quad (5.19)$$

where,

$$\begin{bmatrix} A & N \\ 0 & 0 \end{bmatrix} = \begin{bmatrix} -b/m & A_1/m & -A_2/m & -1/m \\ -A_1/C & -(K_p^1 + C_{leak,1})/C & 0 & 0 \\ A_2/C & 0 & -(K_p^2 + C_{leak,2})/C & 0 \\ 0 & 0 & 0 & 0 \end{bmatrix} \quad (5.20)$$

$$[C \ 0] = [1 \ 0 \ 0 \ 0] \quad (5.21)$$

5.3.2 Continuous Time Simulation of PIO

A simple simulation in continuous time is performed to verify that the PI Observer can indeed estimate the unknown input. This simulation also computes the appropriate gain matrices L_1 , L_2 and L_3 .

First, the block diagrams of the PIO and of the model are built in Simulink that resembles Figure 5.7. A sine wave disturbance with four times the frequency of the input was added to the force balance of the actuator; which resembles an unknown input force.

The poles of the continuous time system are: $-1.087e6$, $-2.372e4$, $-1.912e3$ and -200 . The desired poles for the PI Observer are chosen to be: $-2e6$, $-3e5$, $-3e3$, and -700 based on some iteration to obtain good tracking and estimation. After performing the following pole placement, the observer gains are:

$$L_1 = [1.193e6; -1.844e13; 1.543e15],$$

$$L_2 = -7.071e5, \text{ and}$$

$$L_3 = [-68.97; 0; 0] = N.$$

Although the observer proportional gain matrix, L_1 has very large numbers, the continuous time simulation is performed anyway to see if there is any ill condition.

Figure 5.8 shows the model velocity with disturbance and the input applied.

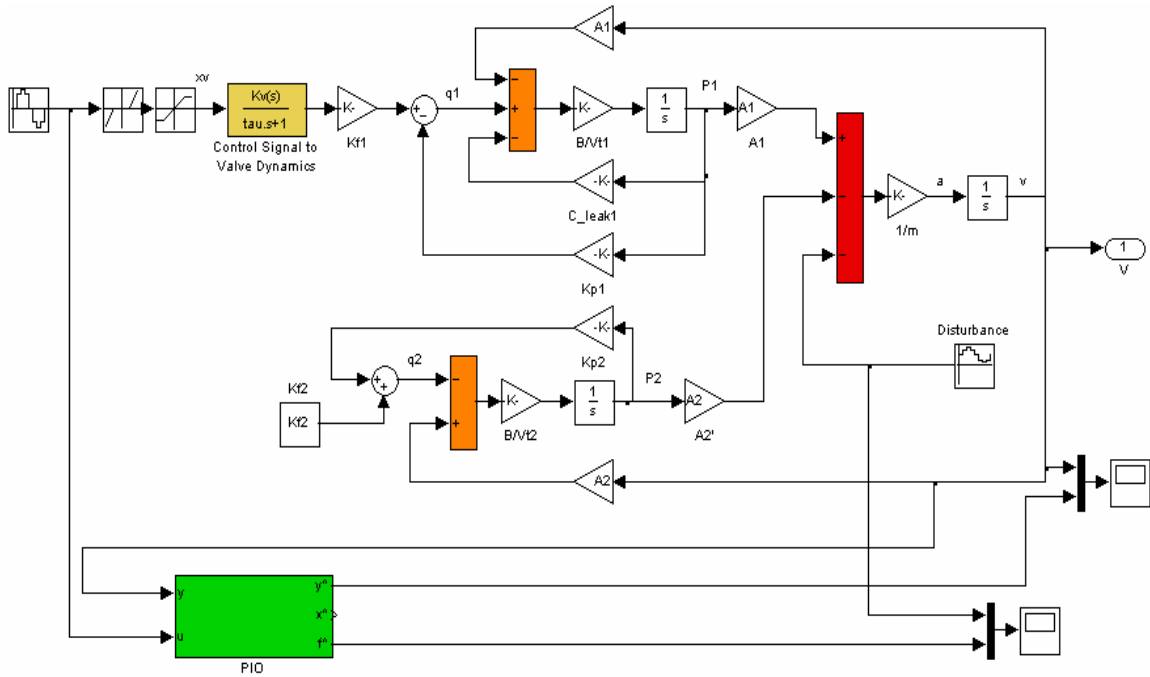


Figure 5.7 Continuous Time Simulation of PIO Simulink Block Diagram

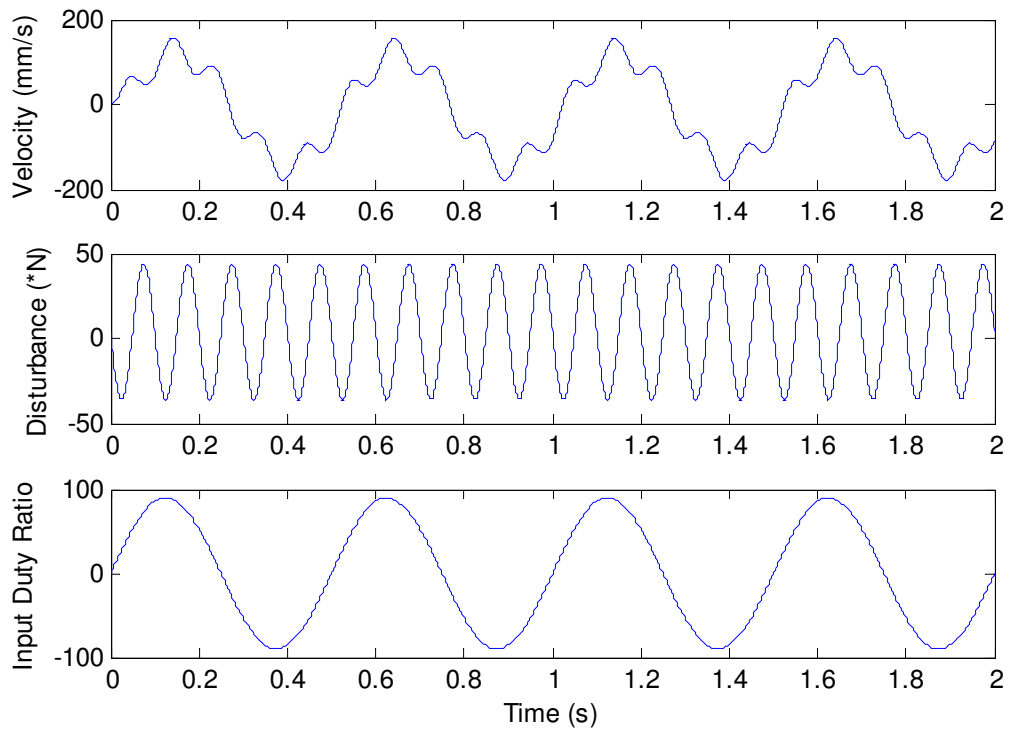


Figure 5.8 Continuous Model Output with Disturbance and Input Applied

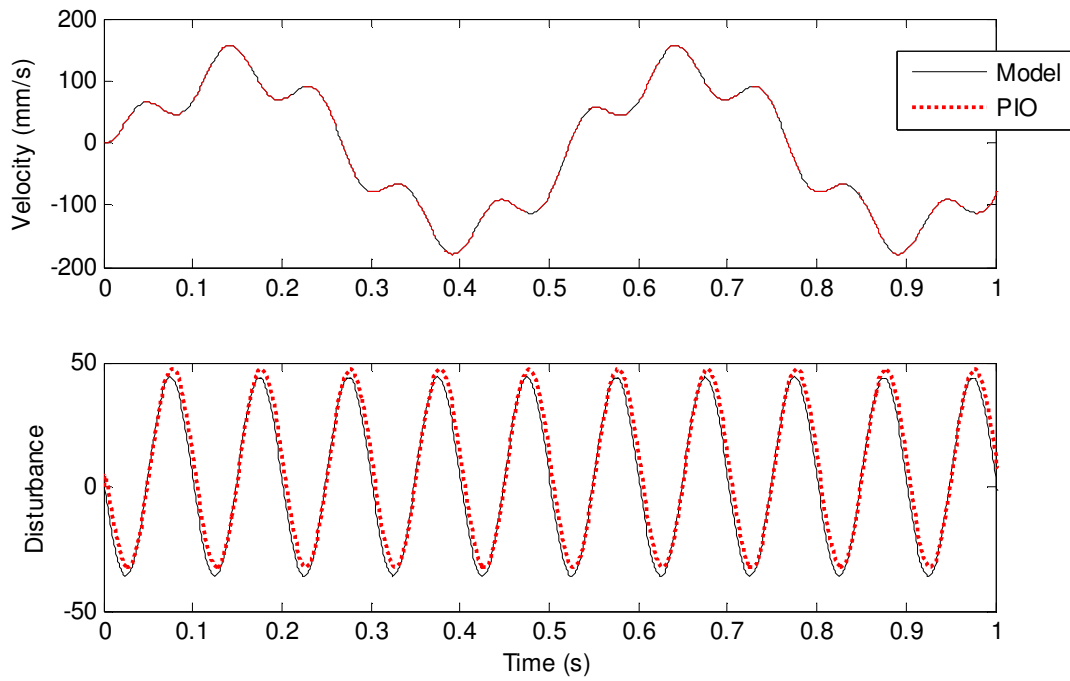


Figure 5.9 Comparison of Model and PI Observer Output and Disturbance

The estimated output and estimated disturbance from the PI Observer are compared to the model output and disturbance applied respectively in Figure 5.9. The velocity from both the model and the PI Observer are almost indistinguishable. The PI Observer estimated the applied disturbance with good accuracy, which gives the confidence that the observer can be used to estimate unknown input and that the gains chosen are appropriate.

5.3.3 Discretization of PIO

To implement the PIO in real time control hardware, the state space matrices needs to be discretized. From Chang [49], the steps to discretize the PIO and also critical assumptions are presented. Let sampling interval to be T and a zero-order hold is used to discretize the continuous system. The discrete time model of the system can be derived as:

$$\begin{aligned} x(k+1) &= \Phi x(k) + \Gamma u(k) + Ff(k) + O(T^2) \\ y(k) &= Cx(k) \end{aligned} \quad (5.22)$$

where $\Phi = \exp(A \cdot T)$, $\Gamma = \int_0^T \exp(A\tau)B d\tau$ and $F = \int_0^T \exp(A\tau)N d\tau$. The following assumptions are made by Chang.

Assumption 1: Sampling interval T is sufficiently small such that the disturbance between sampling does not vary much. Then, $f(k+1) - f(k) \in O(T^2)$ can be obtained for all k . The state estimation and disturbance estimation errors need to have at least the size of $O(T^2)$.

Assumption 2: The system is observable and $\text{rank}\left\{\begin{bmatrix} \Phi & F \\ C & 0 \end{bmatrix}\right\} = n + r$ for the matrices Φ , F and C in discrete time form to minimize state estimation and disturbance estimation errors.

Thus, the discrete time PIO structure is:

$$\begin{aligned}\hat{x}(k+1) &= \Phi\hat{x}(k) + \Gamma u(k) + L_1(y(k) - \hat{y}(k)) + F\hat{f}(k) \\ \hat{f}(k+1) &= \hat{f}(k) + L_2(y(k) - \hat{y}(k)) \\ \hat{y}(k) &= C\hat{x}(k)\end{aligned}\tag{5.23}$$

The sampling period is $T = 0.001$ s and using matlab $c2d()$ function and zero order hold ‘zoh’ method to discretize the state space matrices for observer,

$$\Phi = \begin{bmatrix} 0.9568 & 2.265e-8 & -4.177e-10 \\ -7.73e4 & -0.0018 & 3.375e-5 \\ 1425.8 & 3.375e-5 & -6.224e-7 \end{bmatrix}\tag{5.24}$$

$$\Gamma = \begin{bmatrix} 5.553 \\ 1.01e7 \\ 8.267e3 \end{bmatrix}\tag{5.25}$$

$$F = \begin{bmatrix} -0.0675 \\ 5221 \\ -100.53 \end{bmatrix}\tag{5.26}$$

$$C = [1 \quad 0 \quad 0]\tag{5.27}$$

The following gains are used for the discrete PI Observer:

$$L_{1,D} = L_1 T^2 / 2 = L_1 / 2e6 = [0.5965; -9.218e6; 7.715e8],$$

$$L_{2,D} = L_2 T = L_2 / 1e3 = -707.06, \text{ and}$$

$$L_{3,D} = F = [-0.0675; 5221; -100.53].$$

Where the proportional gain $L_{1,D}$ is chosen to be high so that the estimated output will track the measured output fast and with good accuracy. The gain $L_{2,D}$ improves the unknown input estimation while the gain $L_{3,D}$ scales the actual unknown input appropriately. The gains for implementation on a digital computer is scaled from the gains for continuous time simulation to prevent instability from amplification of measurement noise and digitization,

To evaluate how good the observer is in estimating actual force applied to the actuator, the experiment set up in Figure 4.3 is used. The actuator is commanded to track a sine wave displacement while at the same time being disturbed by the spring restoring force. A force sensor is fixed between the two surfaces and measures the reaction force as the actuator pushes against a vertical linear spring on a stand. Here, the expectation is that the force will be proportional to the displacement of the actuator, assuming other nonlinearity and disturbance forces are minimal. The PIO is run as simulation from MATLAB Simulink offline after the experimental input-output data has been recorded. The input and output is shown in Figure 5.10 while Figure 5.11 shows the Simulink block diagram for offline observer implementation.

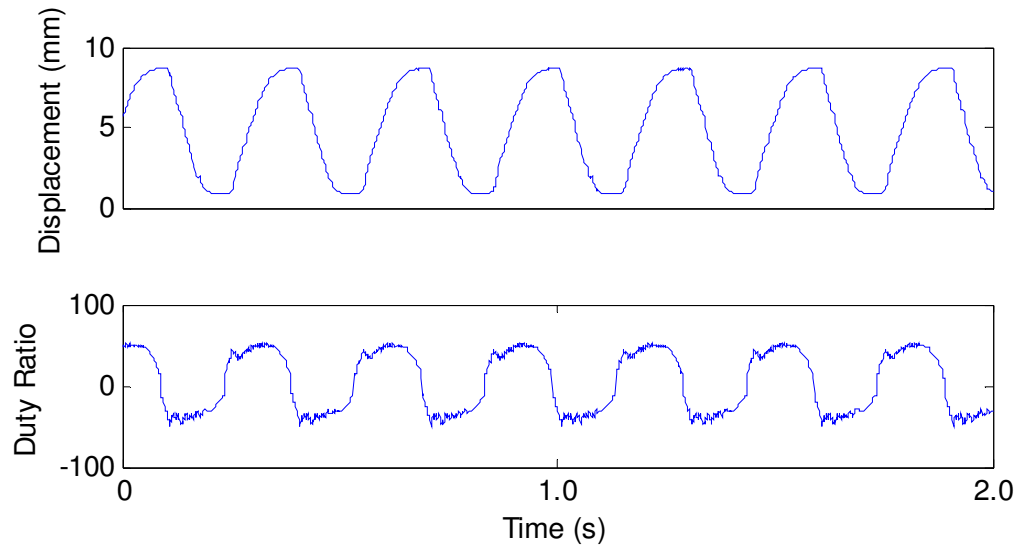


Figure 5.10 Output and Input from Sine Wave Force Experiment

The estimated unknown input force also includes other factors such as gravitational constant, friction force and also constant return pressure as discussed in (4.5). After taking into account other unrelated factors, Figure 5.12 shows how the reaction force estimation compares to the actual measured force.

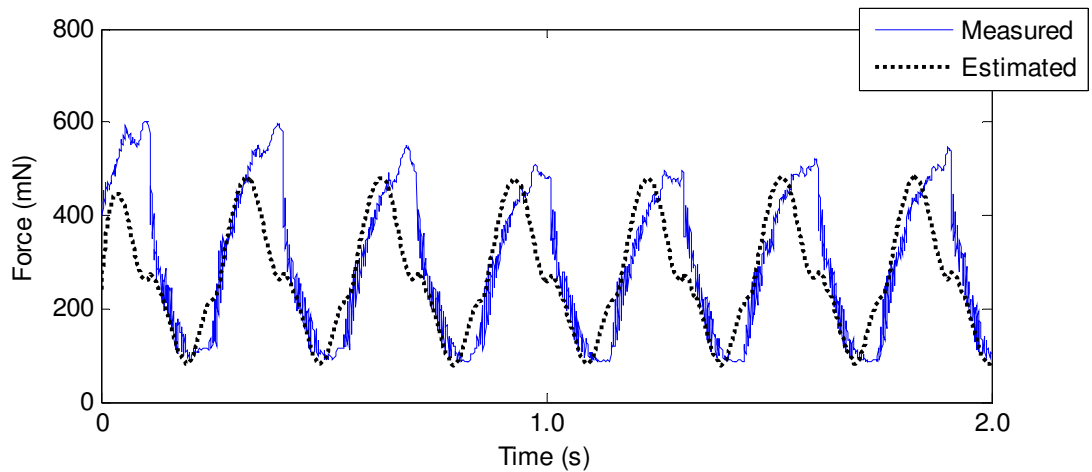


Figure 5.12 Comparison between Estimated and Measured Reaction Force (Sine Wave)

Sine wave displacement is somewhat representative of how the Digital Clay might be used or interacted with, however it is desirable to see how well the PIO estimates the force as the user interacts with the actuator. Here, the actuator is first commanded to stay at an arbitrary vertical displacement before the user pushes down on the pin and releases his/her finger. In both cases, The input of the observer, $u(t)$ is the duty ratio that is proportional to the error in position i.e. $u(t) = K_p \cdot (y_{cmd} - y)$.

Figure 5.13, Figure 5.15 and Figure 5.17 show the input-output data as the user interacts with the actuator. The corresponding comparisons between estimated and measured forces are shown in Figure 5.14, Figure 5.16 and Figure 5.18.

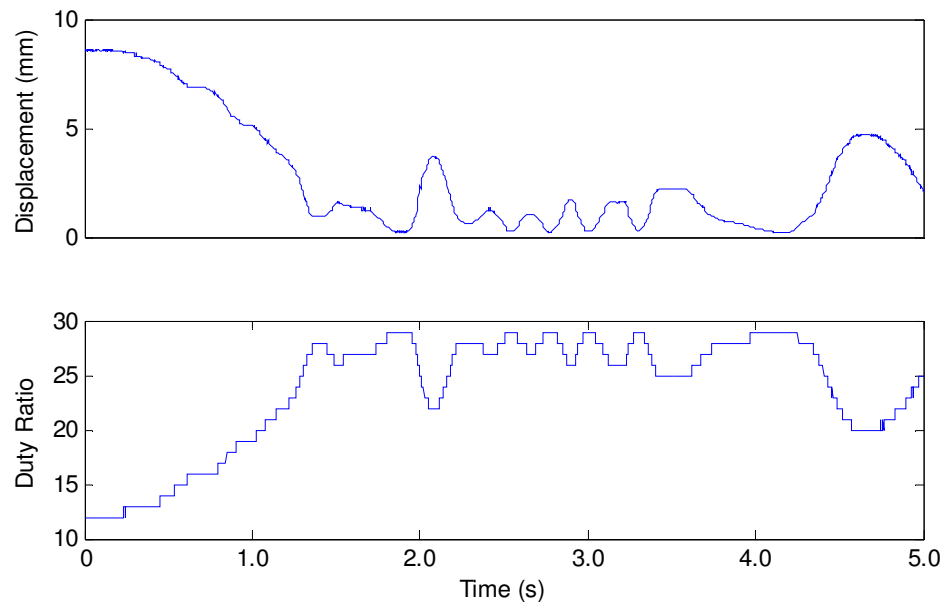


Figure 5.13 Output and Input Data from User Interaction 1

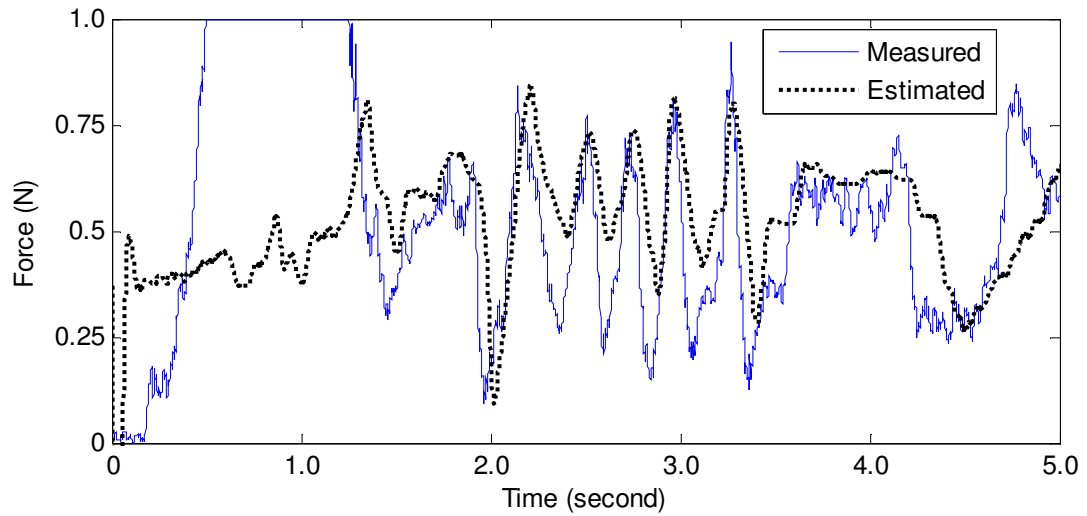


Figure 5.14 Comparison between Estimated and Measured Force from User Interaction 1

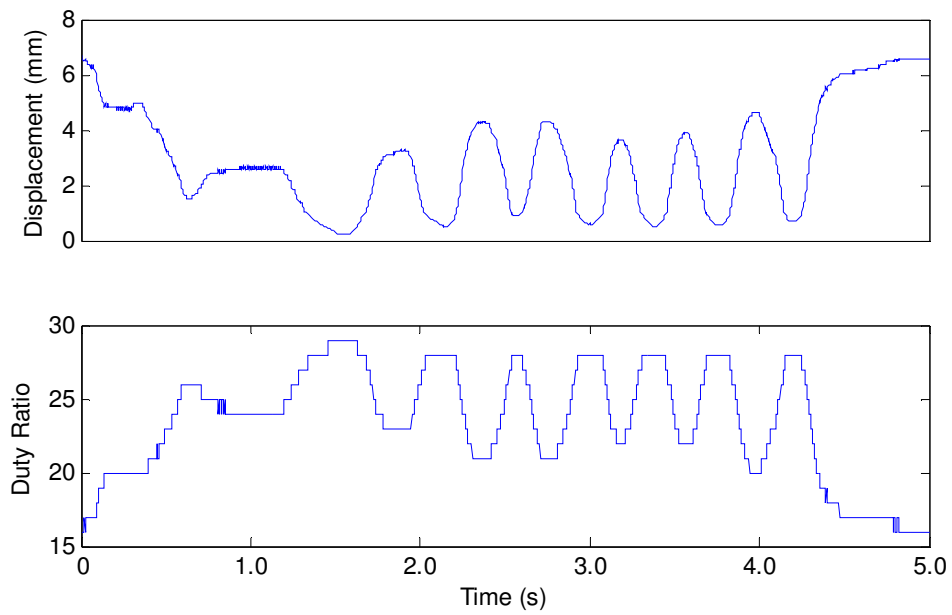


Figure 5.15 Output and Input Data from User Interaction 2

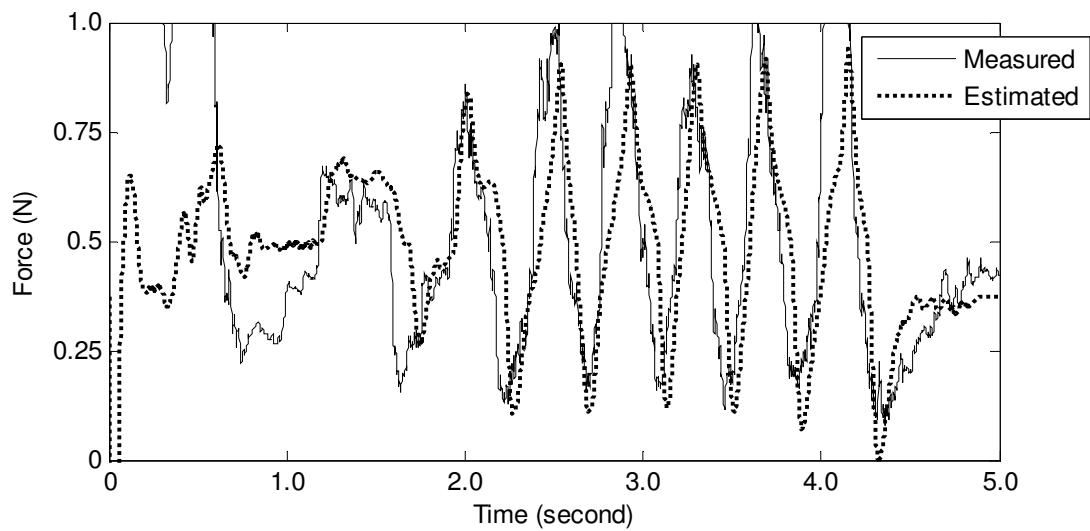


Figure 5.16 Comparison between Estimated and Measured Force from User Interaction 2

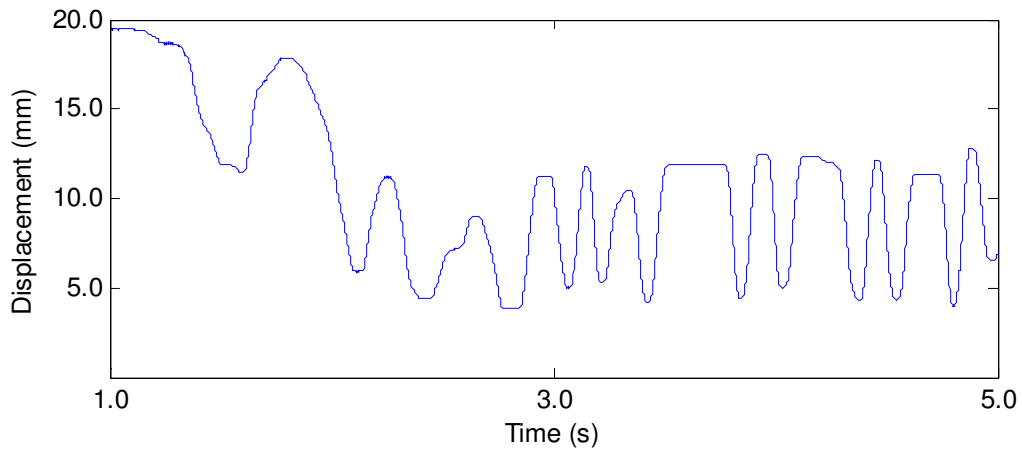


Figure 5.17 Output and Input Data from User Interaction 3

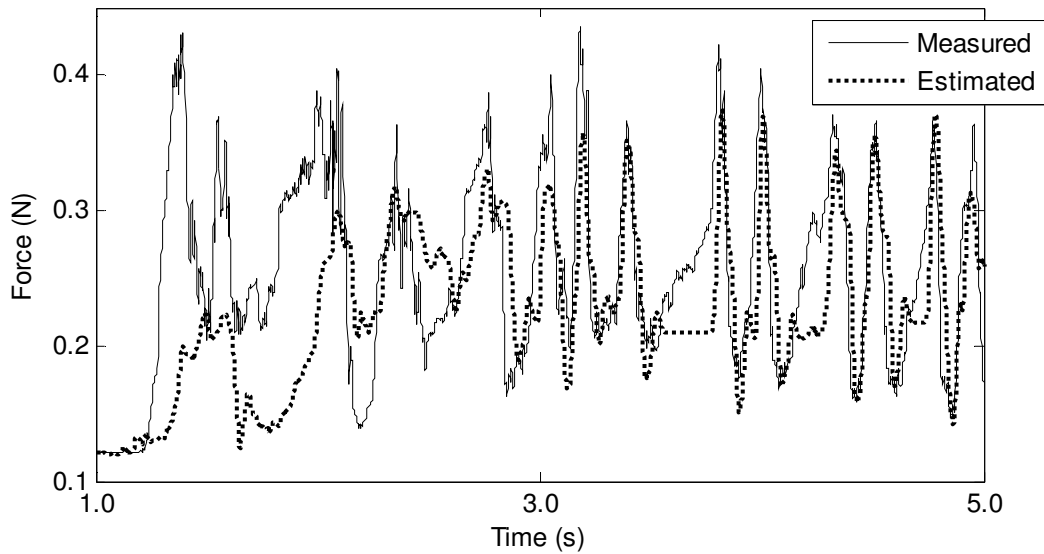


Figure 5.18 Comparison between Estimated and Measured Force from User Interaction 3

From Figure 5.14, Figure 5.16 and Figure 5.18, the estimation of dynamic forces is satisfactory however the observer was not able to estimate the correct forces when the valve was not opening, as shown at the beginning of both figures. This was the initial stage when the actuators were stationary and the valves were closed.

5.4 Disturbance Observer

Another method that can be used to estimate unknown input is the disturbance observer made known by Tomizuka [50][51] and other authors [52][53]. Although typically used for estimating and attenuating unwanted disturbances to a system, this type of observer is simple and widely used. The whole design process lies in choosing the best Q filter to achieve desired results. Figure 5.19 shows the block diagram of the disturbance observer.

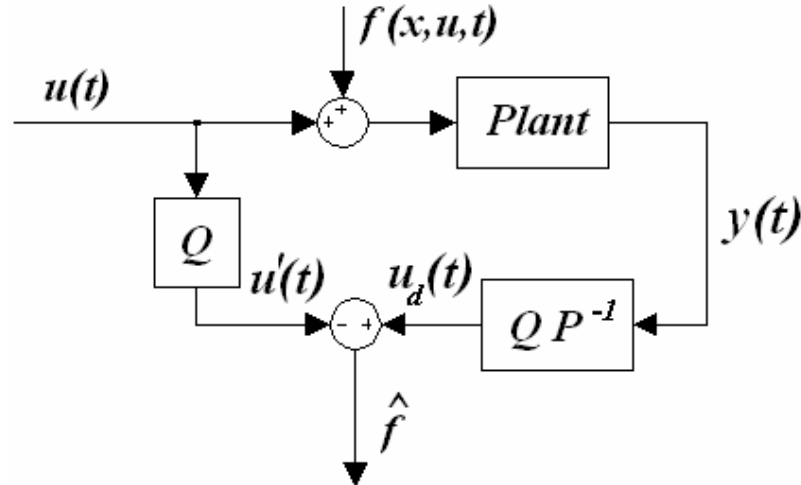


Figure 5.19 Inverse Plant Dynamics Disturbance Observer

This type of observer is sometimes named inverse plant dynamics disturbance observer because according to Schrijver [54], the PIO in the previous sections is also a variation of disturbance observer but with a state space structure. In fact, most of the time, the two will produce similar outcome, as will be shown in the following results. The inverse dynamics disturbance observer (disturbance observer for short) uses the plant transfer function instead of state space form. The plant transfer function is given by,

$$P(s) = \frac{3.284 \times 10^{17}}{5.78 \times 10^{-21} s^4 + 1.038 \times 10^{-16} s^3 + 3.018 \times 10^{-13} s^2 + 1.257 \times 10^{-10} s} \quad (5.28)$$

The disturbance observer shown in Figure 5.19 works by subtracting the actual input without disturbance, $u'(t)$ (before the addition of disturbance signal in the loop) from the estimated input, $u_d(t)$ (after disturbance added) using the measured output, $y(t)$. The disturbance or unknown input, $f(x,u,t)$ is treated as an additional input to the real physical plant, thus the output measured can be assumed to be the result of a commanded input plus the unknown input. The plant model is used to estimate the input that causes this measured output. This involves the inversion of the plant to obtain the input. But in the real world, inversion of a strictly proper polynomial cannot be implemented because of the causality issue. The inverted plant would be non-proper. For a discrete time plant, the inversion of plant requires predicting the future value which is impossible. Thus, a low pass filter, Q is used to introduce a time delay for the real input. Instead of having to predict the future value of the estimated input, the estimate at time k can be obtained from the real input value at time $k-1$.

The low-pass filter, Q is designed in MATLAB using the Butterworth filter program. The Butterworth type is selected as it gives flat bandwidth frequency response (magnitude before cutoff). In this case, the filter has to be the same or higher order than the plant order ($n \geq 4$). The cutoff frequency needs to be designed to meet stability criteria. The open loop plant is stable but with a closed loop proportional control, the plant is able to track input with desirable result.

Figure 5.20 is a plot of the Q filters with various cutoff frequencies (30Hz, 50Hz, 100Hz, 500Hz) in Hz. The delta term is the assumed unmodeled dynamics of the

unknown input. It is modeled as a constant time varying function. $F_d(s) = F/s$. The filters are able to capture the dynamics of the plant and also maintain robust stability with the

$$\text{criteria: } \|T(j\omega)\|_\infty \|\Delta(j\omega)\|_\infty < 1 \text{ or } \|T(j\omega)\|_\infty < \frac{1}{\|\Delta(j\omega)\|_\infty}$$

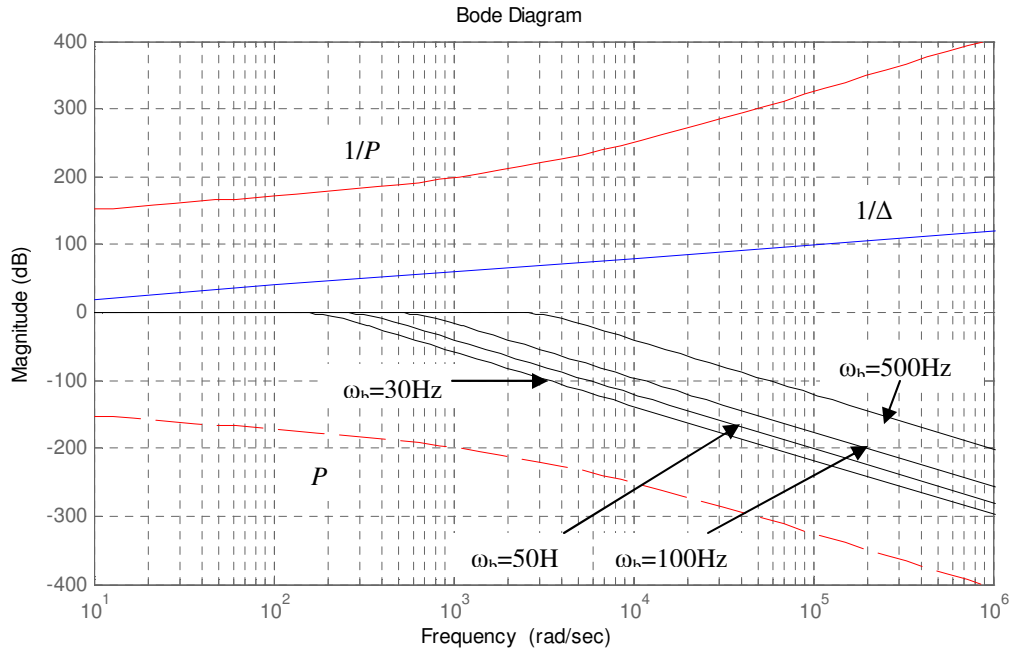


Figure 5.20 Plot of Q Filter with Various Cutoff Frequencies

Figure 5.21 shows the Simulink block diagram for simulating the disturbance observer and the following Figure 5.22 to Figure 5.25 show the actual input (solid), filtered input (dots) and estimated input with disturbance (dashed) for Q filter cutoff frequencies of 100Hz, 50Hz, 30Hz and 16Hz.

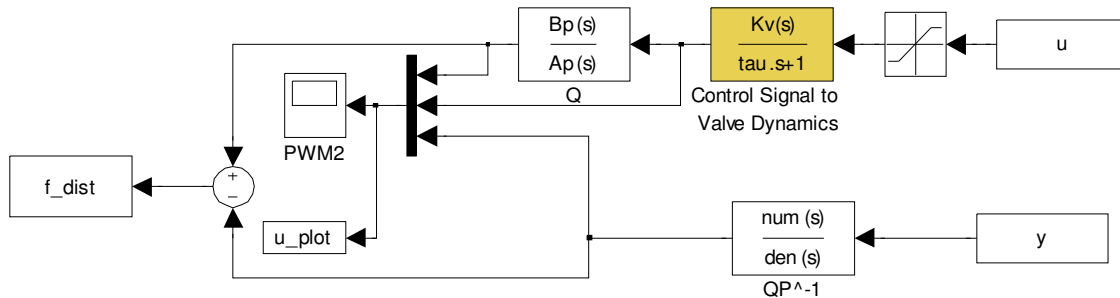


Figure 5.21 Simulink Block Diagram for Disturbance Observer Simulation

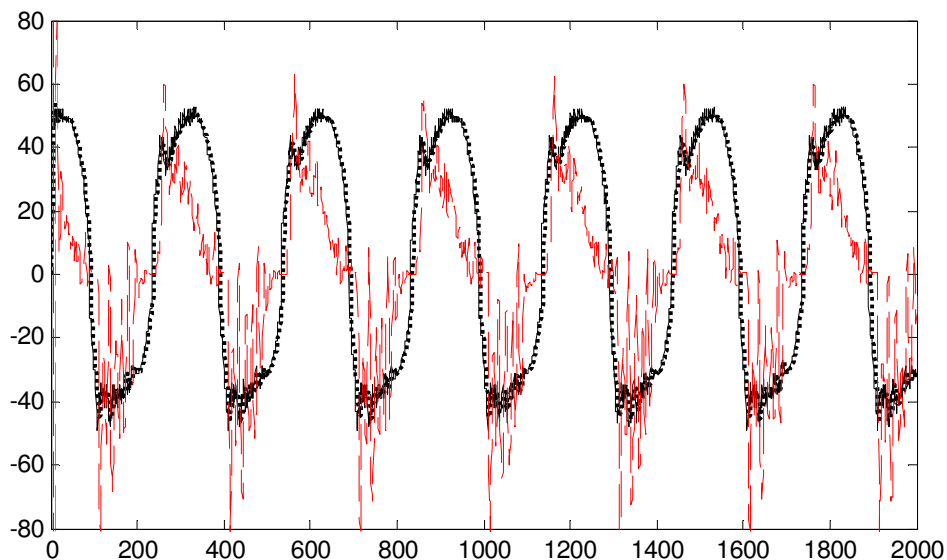


Figure 5.22 Disturbance Observer with 100Hz Q Filter. Actual input (solid), filtered input (dots) and estimated input with disturbance (dashed)

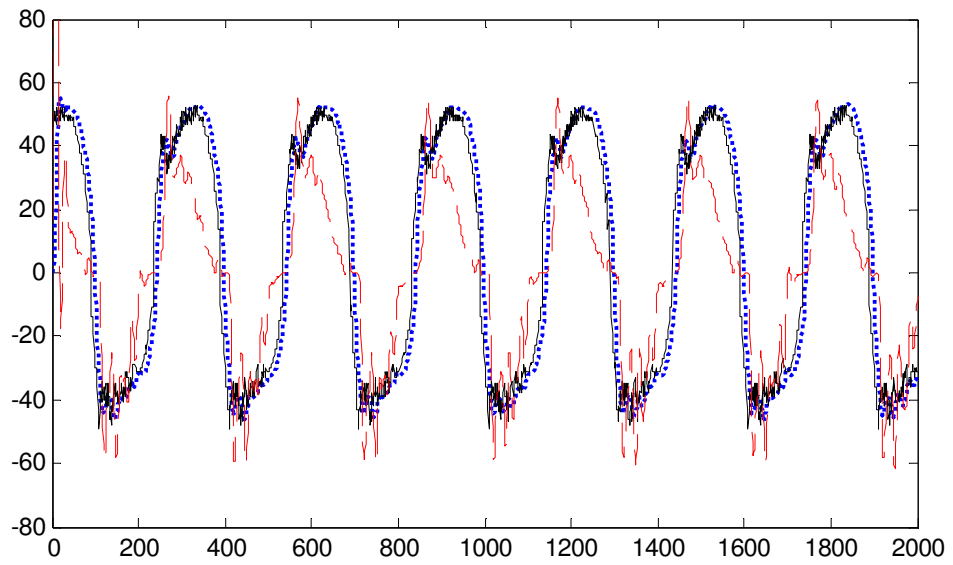


Figure 5.23 Disturbance Observer with 50Hz Q Filter. Actual input (solid), filtered input (dots) and estimated input with disturbance (dashed)

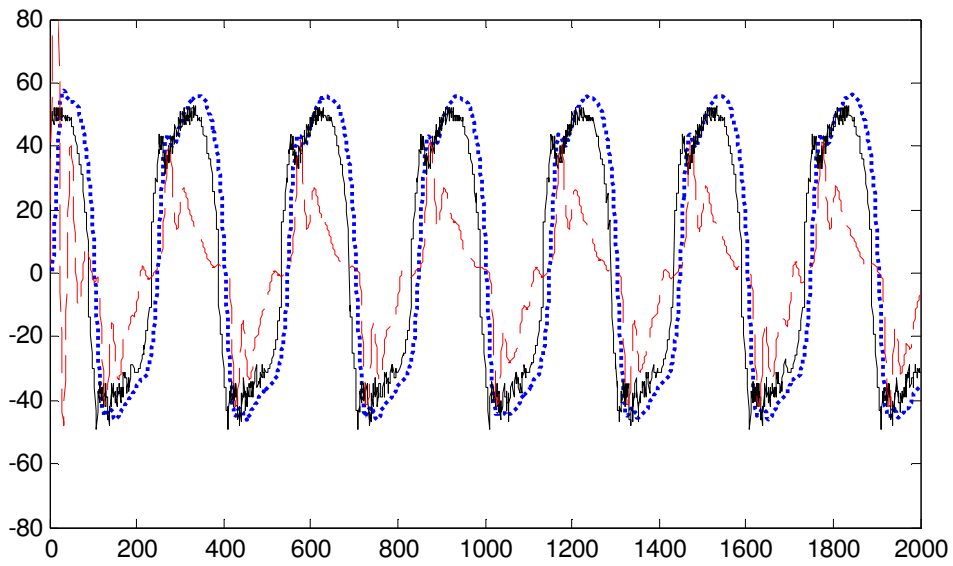


Figure 5.24 Disturbance Observer with 30Hz Q Filter. Actual input (solid), filtered input (dots) and estimated input with disturbance (dashed)

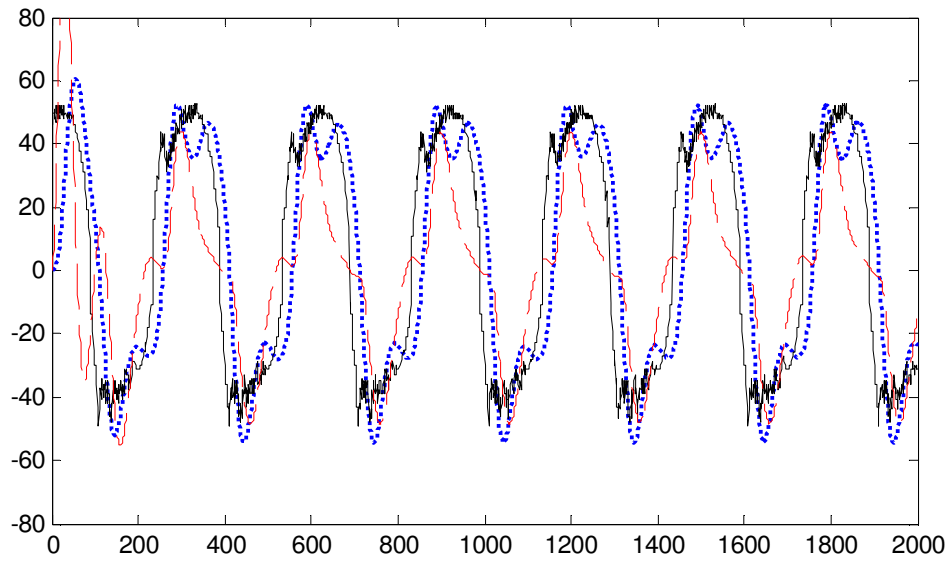


Figure 5.25 Disturbance Observer with 16Hz Q Filter. Actual input (solid), filtered input (dots) and estimated input with disturbance (dashed)

The cutoff frequency that is chosen is 30Hz for best noise rejection and estimation of input plus disturbance. The following transfer function was obtained for Q :

$$Q(s) = \frac{1.26 \times 10^9}{s^4 + 492.6s^3 + 1.2 \times 10^5 s^2 + 1.75 \times 10^7 s + 1.26 \times 10^9} \quad (5.29)$$

or the discrete-time equivalent for sampling time, $T_s = 0.001s$:

$$Q(z) = \frac{0.001 \cdot (0.0624 + 0.2495z^{-1} + 0.3743z^{-2} + 0.2495z^{-3} + 0.0624z^{-4})}{1 - 3.5078z^{-1} + 4.6409z^{-2} - 2.7427z^{-3} + 0.6105z^{-4}} \quad (5.30)$$

and the inverse plant transfer function multiplied with Q is given by,

$$Q(z)P^{-1}(z) = \frac{1 \times 10^6 (4.474 - 2.87z^{-1} - 3.493z^{-2} + 1.481z^{-3} + 0.409z^{-4})}{1 - 3.509z^{-1} + 4.645z^{-2} - 2.746z^{-3} + 0.6114z^{-4}} \quad (5.31)$$

To compare the disturbance observer estimation with the PI Observer estimation, the following estimations are from the same input-output data observed from Figure 5.10 and Figure 5.17 respectively. Figure 5.26 shows the comparison between the spring force estimated by the disturbance observer and the measured reaction force while Figure 5.27 shows the estimated force for user interaction. The disturbance observer estimated force showed similar results to the estimation with the PI Observer, but with slightly higher accuracy, due to the selection of the Q filter.

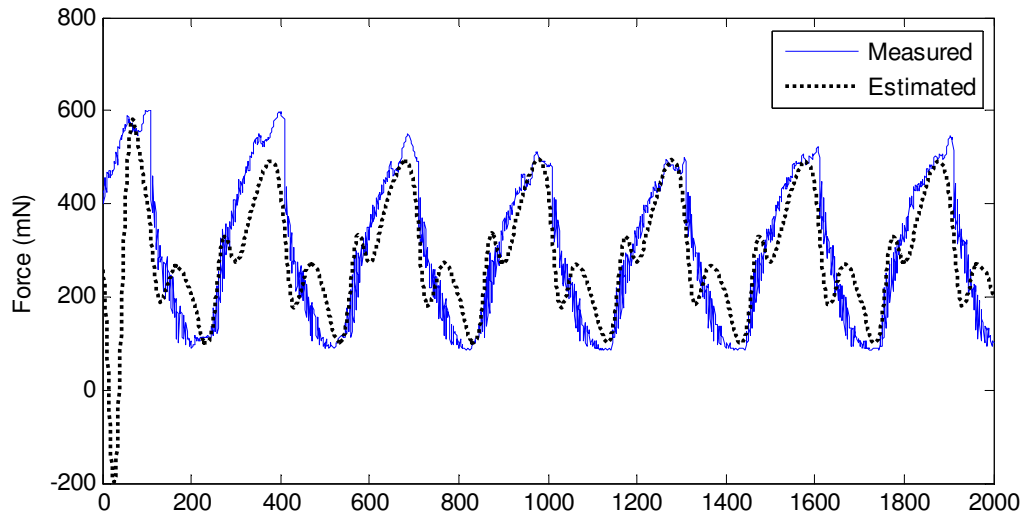


Figure 5.26 Estimated Spring Force Compared to Measured Force

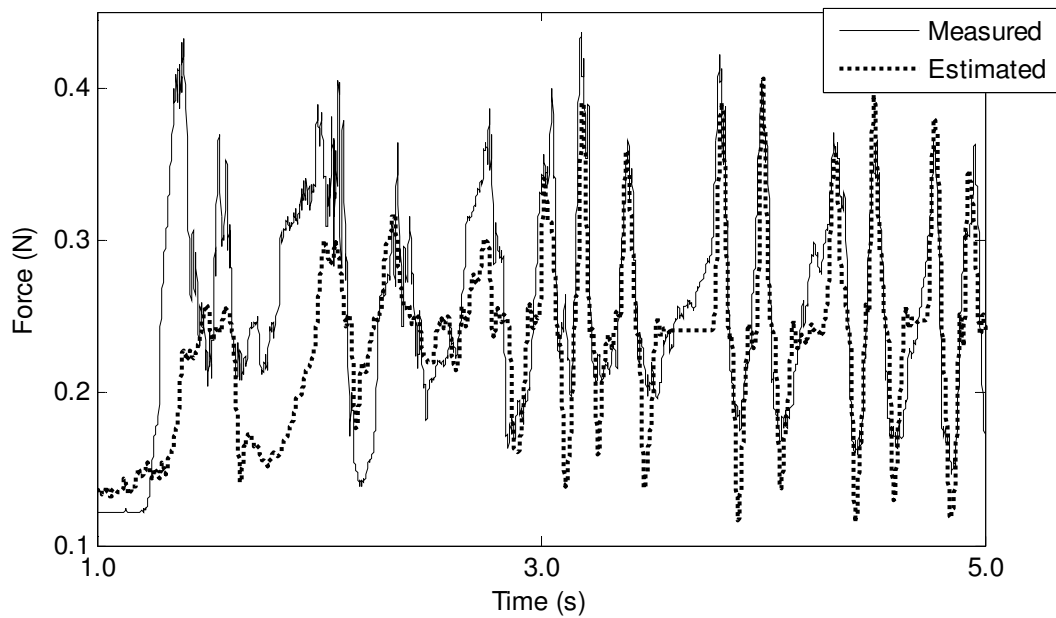


Figure 5.27 Estimated User Interaction Force Compared to Measured Force

5.5 Implementation of Discrete-time Observer on Digital Controller

To employ the observers in real-time on a digital controller, several important factors need to be addressed. For the Digital Clay prototype, the digital controller is essentially the Pentium 4 processor that is being run in real time under a Real Time Linux (RT Linux) operating system. Under RT Linux, the priority of the processor is modified to allocate all computing power to performing arithmetic, memory addressing, interrupt service routines and such. The object file that will be inserted into the operating system kernel is written in C language. Most basic arithmetic operations found in the *math.h* library of C can be performed. However, real time floating point operations is only available through the compiler and not supported by the hardware and as a result, the implementation of observer algorithm is not as straight forward as performing numerical

simulations offline. The disturbance observer from section 5.4 will be implemented in the host computer. From equations (5.30) and (5.31), the discrete-time transfer function can be written for computer algorithm in terms of time delays as follows,

$$Q(z) = \frac{0.001 \cdot (0.0624 + 0.2495z^{-1} + 0.3743z^{-2} + 0.2495z^{-3} + 0.0624z^{-4})}{1 - 3.5078z^{-1} + 4.6409z^{-2} - 2.7427z^{-3} + 0.6105z^{-4}} = \frac{x_f(k)}{x_v(k)} \quad (5.32)$$

$$\begin{aligned} & x_f(k) - 3.5078 \cdot x_f(k-1) + 4.6409 \cdot x_f(k-2) \\ & \quad - 2.7427 \cdot x_f(k-3) + 0.6105 \cdot x_f(k-4) \\ & = 0.001 \cdot (0.0624 \cdot x_v(k) + 0.2495 \cdot x_v(k-1) + 0.3743 \cdot x_v(k-2) \\ & \quad + 0.2495 \cdot x_v(k-3) + 0.0624 \cdot x_v(k-4)) \end{aligned} \quad (5.33)$$

$$Q(z)P^{-1}(z) = \frac{1 \times 10^6 (4.474 - 2.87z^{-1} - 3.493z^{-2} + 1.481z^{-3} + 0.409z^{-4})}{1 - 3.509z^{-1} + 4.645z^{-2} - 2.746z^{-3} + 0.6114z^{-4}} = \frac{x_d(k)}{y(k)} \quad (5.34)$$

$$\begin{aligned} & 1 \times 10^6 \cdot (4.474 \cdot x_d(k) - 2.87 \cdot x_d(k-1) - 3.493 \cdot x_d(k-2) \\ & \quad + 1.481 \cdot x_d(k-3) + 0.409 \cdot x_d(k-4)) \\ & = y(k) - 3.509 \cdot y(k-1) + 4.645 \cdot y(k-2) \\ & \quad - 2.746 \cdot y(k-3) + 0.6114 \cdot y(k-4) \end{aligned} \quad (5.35)$$

The variables $x_f(k)$, $x_v(k)$, $x_d(k)$ and $y(k)$ are the input and output of the transfer functions where $y(k)$ is the displacement measurement and $x_d(k)$ is the output of the plant inverse transfer function at sampling instance k . The transfer function for modeling the control valve dynamics is given by,

$$\frac{x_v(k)}{u(k)} = \frac{0.002175z^{-1}}{1-0.8187z^{-1}} \quad (5.36)$$

The PWM duty ratio input is $u(k)$. The estimate of unknown disturbance input, F_d is then given by the difference between filtered input, $x_f(k)$ and output of the plant inverse transfer function $x_d(k)$. The force estimate can then be obtained by using the relationship:

$$F_d = F_{\text{reaction}} + \text{sgn}(\dot{y}) \cdot f_{\text{coulombic}} + mg \quad (5.37)$$

The code of the observer algorithm is as follows:

```
// -----Disturbance Observer-----//
//Model valve saturation
if (Duty>90){Duty=90;}
else if(Duty<-90){Duty=-90;}

//if(Duty>-10 && Duty<10){Duty=0;}
u = 1000000*Duty;
//-----
y = (double)DSP[Y*5 +X]; // Displacement Measurement in um

//Simulated Valve Delay
xv = 0.8187*(double)xv1 + (0.002175)*(double)pwm1;
//Filtered Input x_v
xu_f = 3.5078*(double)xu_f1 - 4.6409*(double)xu_f2 +
2.7427*(double)xu_f3 - 0.6105*(double)xu_f4 + (0.0000624)*(double)xv
+ (0.0002495)*(double)xv1 + (0.0003743)*(double)xv2
+ (0.0002495)*(double)xv3 + (0.0000624)*(double)xv4;

//Plant Inverse*Filter
x_d = 3.509*(double)x_d1 - 4.645*(double)x_d2 + 2.746*(double)x_d3
- 0.6114*(double)x_d4 + 1000*( (4474)*y - (2870)*ym1 - (3493)*ym2
+ (1481)*ym3 + (409.3)*(double)ym4 );

//-----Storing parameters as delays-----
x_d4 = x_d3;
x_d3 = x_d2;
x_d2 = x_d1;
x_d1 = x_d;

ym4 = ym3;
ym3 = ym2;
ym2 = ym1;
ym1 = y;
```



```

xu_f4 = xu_f3;
xu_f3 = xu_f2;
xu_f2 = xu_f1;
xu_f1 = xu_f;

xv4 = xv3;
xv3 = xv2;
xv2 = xv1;
xv1 = xv;

pwm1 = u;
//-----Disturbance Force-----
Disturbance_est = 0.0000001*(double)xu_f - x_d;

```

It is inevitable that the coefficients of the filters have floating point values and only fixed point operation is supported. Thus the duty ratio term has to be scaled by 10^6 times to allow for more significant digits and reduce rounding off error. For the final calculation for disturbance estimate, the appropriate rescaling is performed to obtain meaningful values.

5.6 Remarks and Discussion

Similar to the PI Observer, the disturbance observer's ability to estimate force exerted on the actuator is limited to the following:

1. The input must not saturate when interacted by the user. When the input saturates, the only information available to the observer is actuator displacement. The information from the saturated input is not sufficient.
2. The observer is not able to estimate forces when there is no displacement change. As there is no pressure sensor available, the observer only relies on input and output for estimation.

3. The unmodeled dynamics of the system, such as Stiction (static friction), and leakage are assumed to be small and present negligible variation to the estimation.
4. The accuracy of the observer is limited by how much of the actual system states dynamics is modeled. The model is linearized and assumed to have time invariant parameters, while the actual system is nonlinear. Therefore for the Digital Clay device, it is best if as many nonlinear effects are kept to a minimum – leakage, stiction, unmodeled fluid restriction be reduced.
5. Although the model is able to provide good estimate for the system output – velocity (measured states) from measured displacement, the cylinder pressures (unmeasured states) are not available, thus there is no unique solution available. Estimated states are not unique to arrive at the same output as the actual system.

CHAPTER 6 SOURCE PRESSURE CONTROL BY FLOW CONTROL

From Chapter 5, it was shown that the force observer designed can estimate user exerted dynamic force to a certain degree of accuracy. The biggest limitation however, of the observer was the inaccuracy of force estimation if the velocity is zero and if valve dead band is present. Furthermore, for the application of Digital Clay, it is desirable for the actuator's displacements to be free to displace the surface while at the same time displaying force sensation to the user. The problem that arises from using only displacement sensor to estimate force is the difficulty or it is almost impossible to control force when at the same instance the user is pushing down on the pin - the displacement sensors will give a negative velocity. For the admittance mode of haptic display, it is possible to use the observer designed to estimate the force exerted and then control the motion of the actuators. If the impedance mode of haptic display is desired, the force estimation will be affected by motion of the user on the actuator; this method is still a limitation for Digital Clay. Therefore in this chapter, another method of displaying force/pressure to the user of Digital Clay such that the impedance mode can be realized will be explored. The proposed method will attempt to control or more precisely regulate the source pressure that actuates the actuators by flow control of inlet and outlet valves.

6.1 Two-valve Hydraulic Pressure Regulation/Control System

The current system employs a pair of on/off solenoid valves as a source selection mechanism to switch between high pressure fluid to drive the actuators and low pressure for the fluid to vent. This operation alternates between turning either valves on or both off to seal the fluid in the system. There is no purpose in turning both on as the high pressure fluid will just vent without going to the system. In Figure 6.1, the schematic summarizes this operation. From the pressurized tank, the line is first passed through the inlet valve and then the flow is split into the line going into the Fluid Channeling Block and another line to vent via the second outlet on/off valve. The pressure regulator is set to output 25 psi to pressurize the silicone oil reservoir. The fluid pressure in the actuator will quickly build up to equal ~25 psi when the first valve is turned on and vent valve is shut off, assuming minimal leakage.

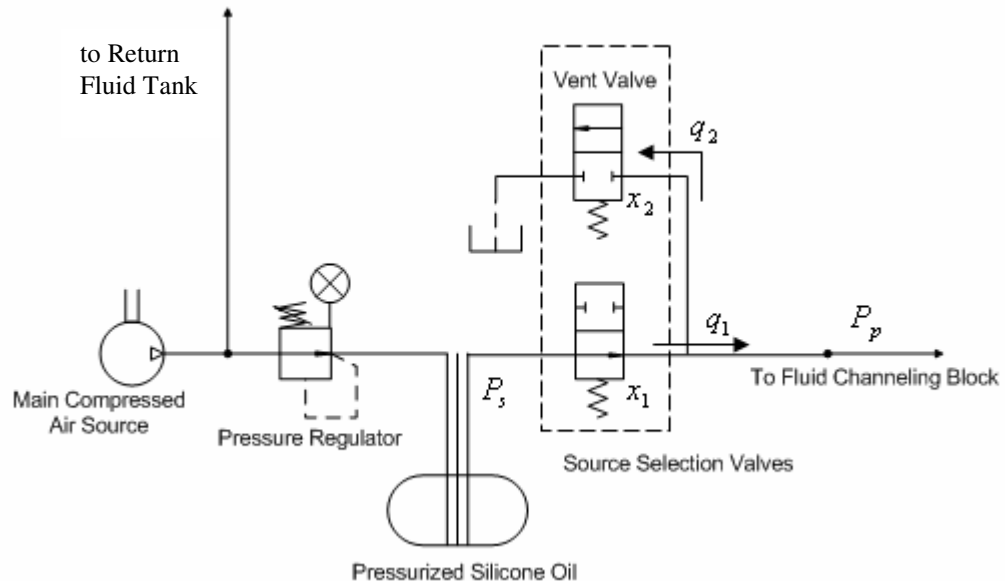


Figure 6.1 Pressure Source Selection System for Digital Clay

The idea is that perhaps there is a way to regulate the pressure in the line going to the actuators by controlling the input and output flow via the two on/off valves. Ideally, a closed loop system is desired, with at minimum, a pressure sensor to provide feedback on fluid line pressure so that appropriate control of the flows can be achieved. This of course is an over simplification of an electronic pressure regulator which has other integral components not available. First to be able to accomplish this with just two valves, it is best to look at how a typical pressure control valve (PCV) or a pressure relief valve works.

A relief valve works by limiting the pressure in the line. A mechanically predetermined pressure set point will control the valve to release or vent the pressurized fluid via a path of least resistance. The pressure in the line will drop as this happens and when the pressure is below the set point, the valve will close via a spring mechanism, and the pressure will build up again. Usually the valve will be forced open mechanically. This idea will be the starting point of the investigation here. Of course, the line pressure is not controlled this way and to maintain a somewhat constant pressure involves more than just relieving excess pressure. But assuming the flow in and flow out process is repeated fast enough without compromising the smoothness of transition, it will be a method to vary supply line pressure. A mathematical model of the fluid line and valves is derived and a simulation performed in Simulink to study the feasibility of this concept.

6.1.1 Derivation of System Equations

First, the flows, q_1 and q_2 through an orifice for both inlet and outlet source selection valves can be given by the following equations,

$$q_1 = c_d w x_1 \sqrt{\frac{2}{\rho} (p_s - p_p)} \quad (6.1)$$

$$q_2 = c_d w x_2 \sqrt{\frac{2}{\rho} (p_p)} \quad (6.2)$$

here, the coefficient of discharge, c_d and orifice area gradient, w are assumed to be identical for both valves. The controlled valve spool displacements are x_1 and x_2 respectively. Linearizing the two equations,

$$q_1 = K_{f,1} x_1 - K_{p,1} p_p \quad (6.3)$$

$$q_2 = K_{f,2} x_2 + K_{p,2} p_p \quad (6.4)$$

where the pressure and pressure sensitivities coefficients are,

$$K_{f,1} = c_d w \sqrt{\frac{2}{\rho} (p_s - p_{p0})} \quad (6.5)$$

$$K_{f,2} = c_d w \sqrt{\frac{2}{\rho} (p_{p0})} \quad (6.6)$$

$$K_{p,1} = \frac{c_d w x_0}{\sqrt{2\rho \cdot (p_s - p_{p0})}} \quad (6.7)$$

$$K_{p,2} = \frac{c_d w x_0}{\sqrt{2\rho \cdot (p_{p0})}} \quad (6.8)$$

The pipe flow continuity equation is given by,

$$q_1 - q_2 = \frac{V}{\beta} \frac{dp_p}{dt} \quad (6.9)$$

where $V = \frac{\pi \cdot d_{pipe}^2}{4} \cdot l_{total}$

The pressure control model, with two inputs, x_1 and x_2 and 1 output, y is given by the following first-order equation,

$$\frac{dP_p}{dt} = A \cdot P_p + B_1 x_1 + B_2 x_2 \quad (6.10)$$

$$y = P_p \quad (6.11)$$

where $A = \frac{-(K_{p,1} + K_{p,2})\beta}{V}$, $B_1 = \frac{K_{f,1} \cdot \beta}{V}$, $B_2 = -\frac{K_{f,2} \cdot \beta}{V}$, and $C = 1$

6.1.2 Simulation of Pressure Control Law

The simulation will help determine what type of control law is to be implemented that will produce the best pressure tracking. From experience, a feedforward proportional control and a proportional plus integral feedback controller are needed to track step reference with fast speed and low steady state error. This simulation is done with the assumption that the valves used are identical and with 20% dead band and 95% duty ratio saturation. The following block diagram was constructed in Simulink for the simulation.

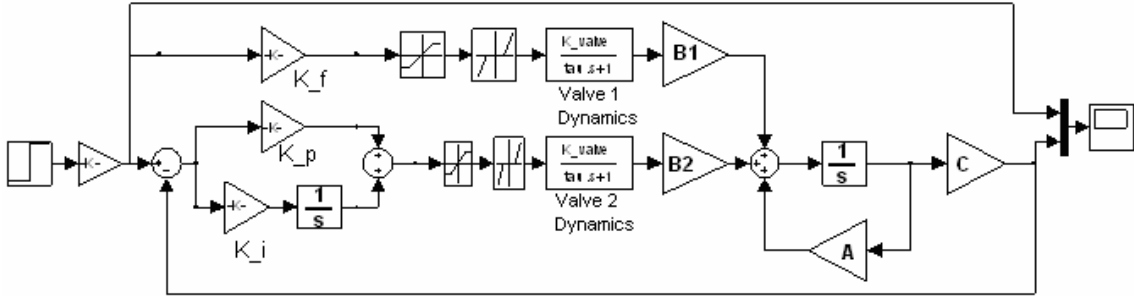


Figure 6.2 Simulink Block Diagram For Pressure Control Simulation

The feedforward proportional gain controls a proportional amount of flow into the line based on the desired pressure. This gain will determine the response of the pressure tracking. The feedback proportional and integral gains control the amount of flow out from the line to release the system pressure if it is higher than or close to the desired pressure and allow pressure to build if it is lower than the desired pressure. The goal is to find a perfect balance of in and out flow such that the system pressure could be maintained. The simulation results are shown in Figure 6.3 and Figure 6.4.

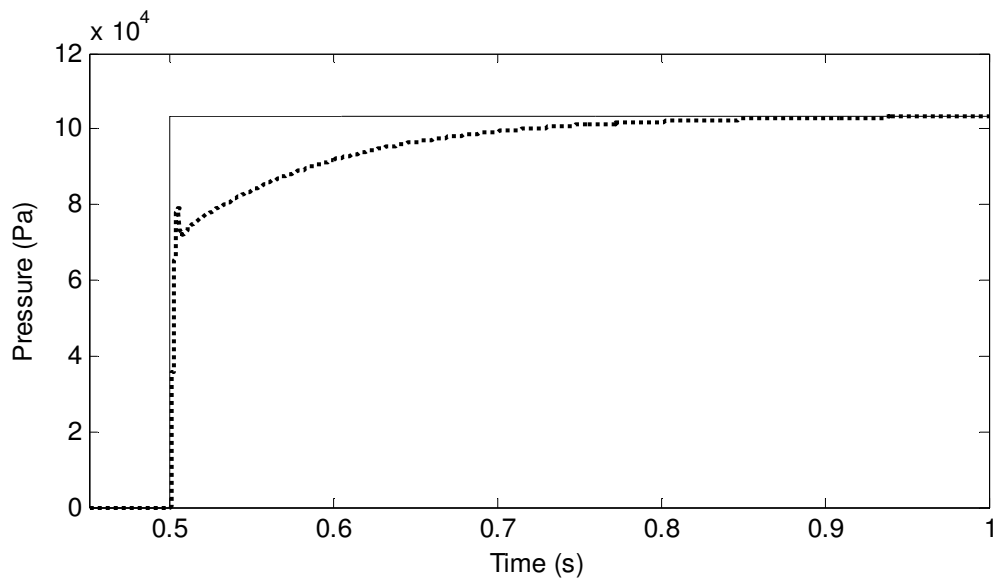


Figure 6.3 Simulation of System Pressure (····) Tracking of a Step Command (—)

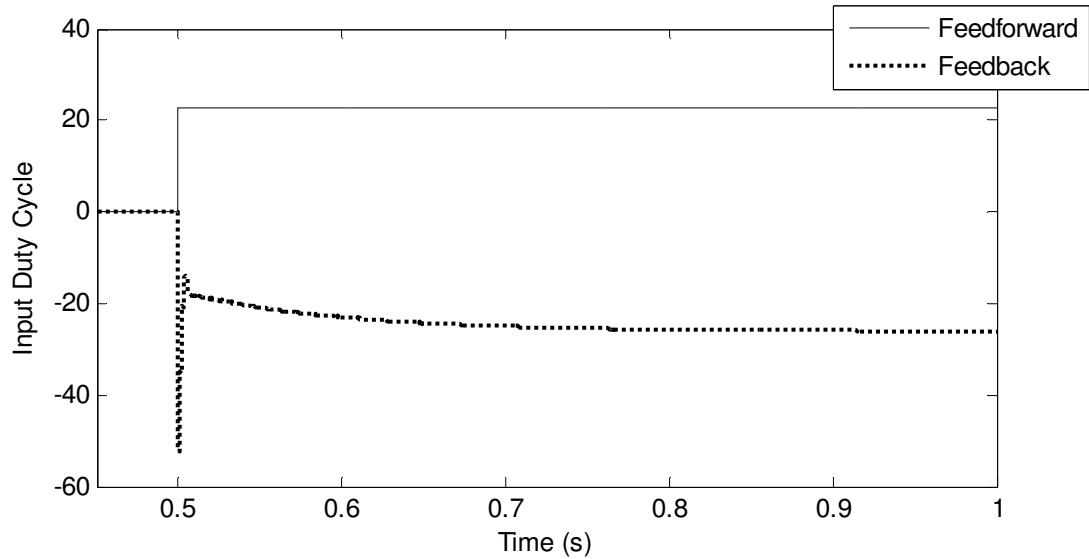


Figure 6.4 Simulation of Feedforward and Feedback Duty Cycle Input

From Figure 6.4, the inlet duty cycle was constant while the outlet duty cycle adjusts the flow to steady state value in less than 0.5 seconds. While the simulation is a simplified and linear system, the actual system is not. The inlet and outlet source selection valves are to be controlled via pulse width modulation and the flow behavior of the actual valves under PWM is not known. The next step is to perform some PWM vs. Flow experiments to obtain the best base frequency that will give the most linear flow-duty ratio relationship.

6.1.3 Flow-Duty Ratio Study of Inlet/Outlet Valves

Figure 6.5 shows the theoretical valve spool position at each cycle of on/off. The time delays for the spool to be fully open from closed position and to be fully closed from the open position are 5 milliseconds each. This means that the base period for the PWM has to be at least 10ms and in addition to the maximum desired opening time.

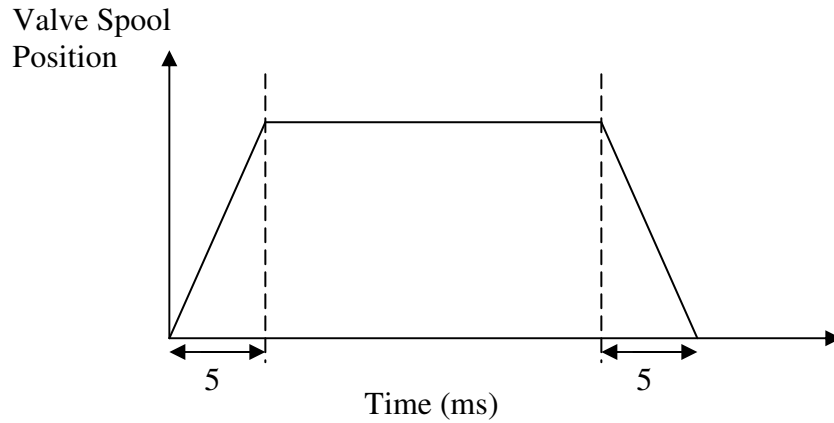


Figure 6.5 Theoretical Valve Spool Position At Each Cycle

The base frequency has to be chosen such that the valve dead band would not be too high (from 0% to 100% duty ratio). Furthermore, a longer base period has higher resolution. On the other hand, a higher base frequency (shorter period) would increase linearity. The following three figures show flow rate as function of duty ratio experiments for 50Hz, 40Hz and 20Hz base frequency respectively.

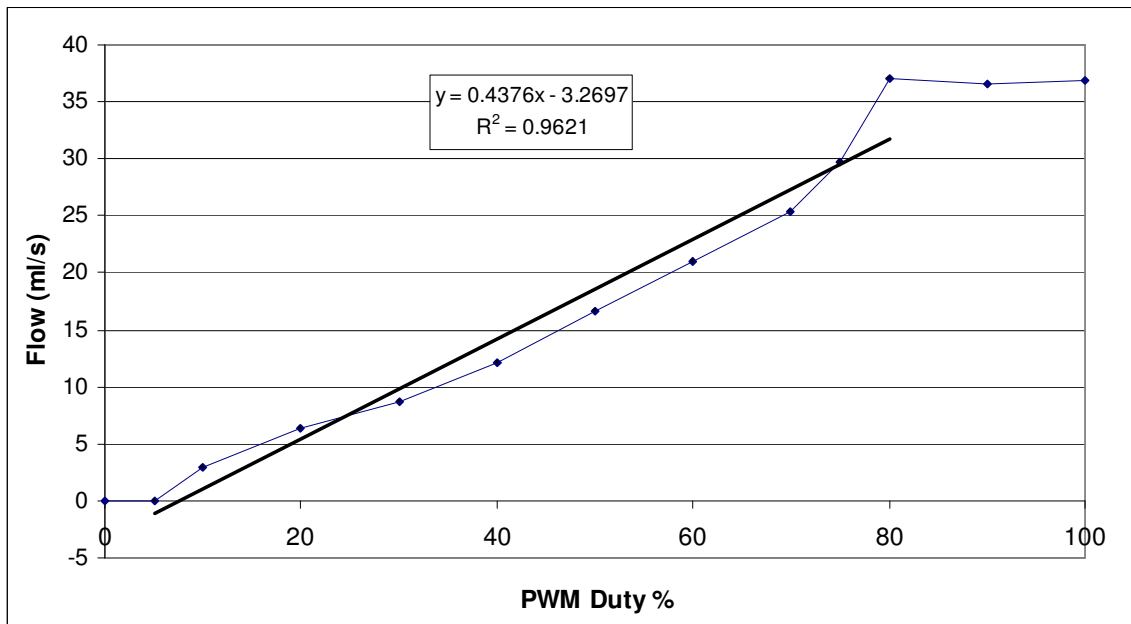


Figure 6.6 Flow Rate vs. PWM Duty Ratio for 50Hz Base Frequency

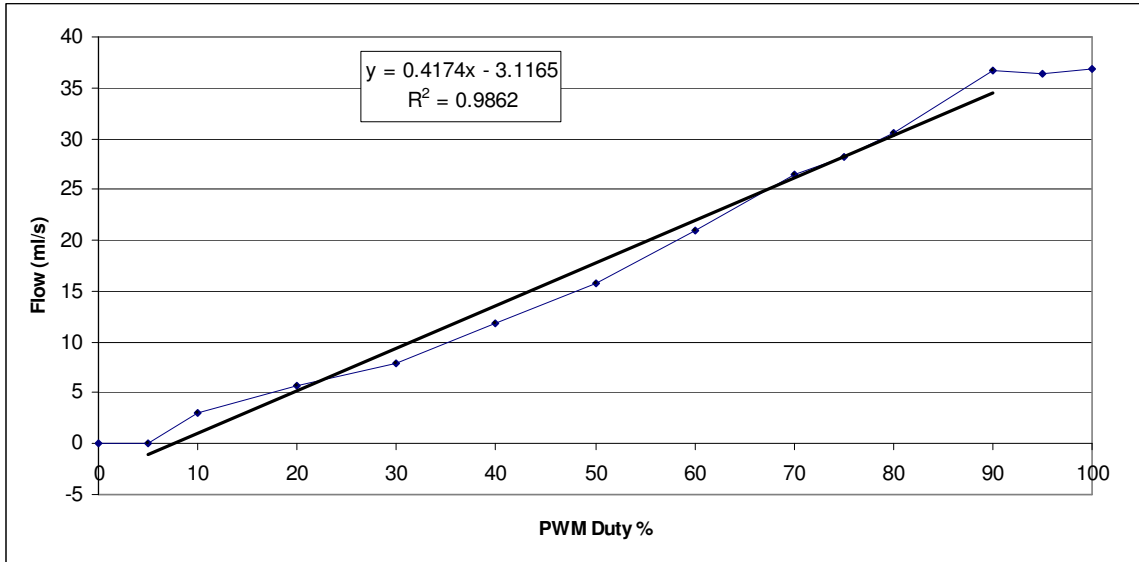


Figure 6.7 Flow Rate vs. PWM Duty Ratio for 40Hz Base Frequency

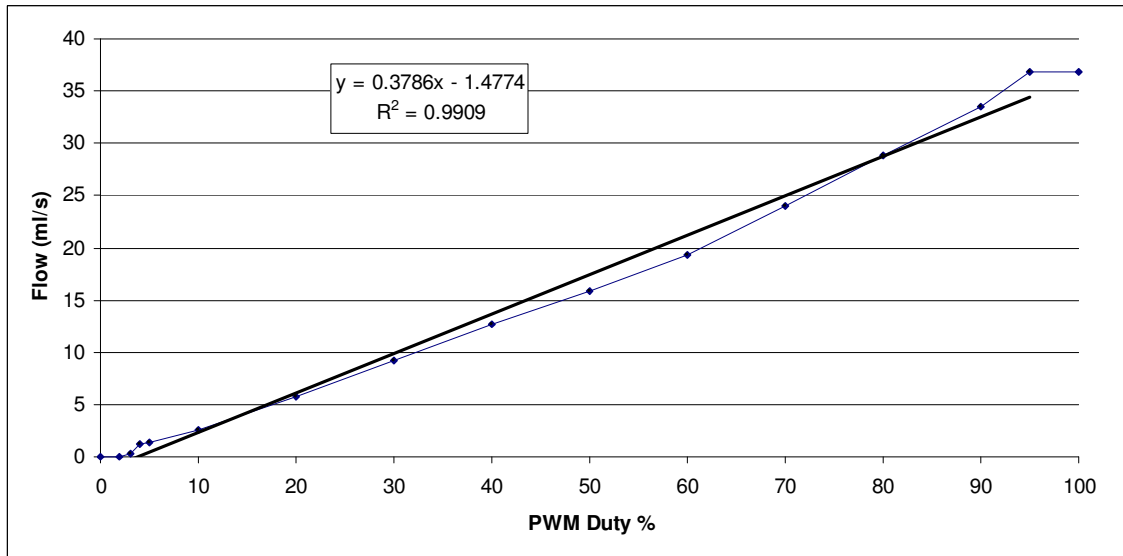


Figure 6.8 Flow Rate vs. PWM Duty Ratio for 20Hz Base Frequency

From the experiments performed, the flow rate vs. duty ratio with 20 Hz base frequency displays the most linear relationship compared to base frequency of 40Hz and 50Hz. The relationship is actually a linear function as instantaneous orifice size (duty

ratio) is related to flow linearly. This experiment serves two purposes, to determine the best base frequency for PWM control of valve and also for parameter identification of valve. Some observations during experiments are i) valves produced high frequency noise, ii) inevitability of system to be air-free when the valves are pulsed hence, iii) air in the system causes extreme vibration in the line and valve (water hammer effect), iv) valves start to heat up after prolonged period of modulating. Observations suggest that perhaps the valves are not fast enough and do not work effectively for this purpose. The usage in this way also causes the valves to overheat, implying that the fast on/off action is overloading them. Furthermore, when a pressure sensor was installed on the line to monitor the line pressure, undesirable pressure spikes and fluctuations are observed. Figure 6.9 and Figure 6.10 show the undesirable effect.

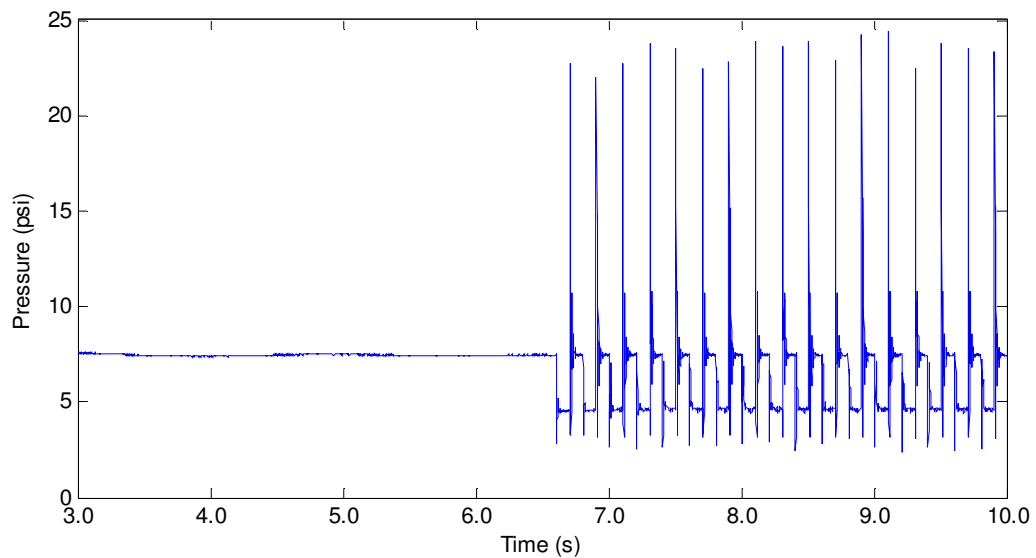


Figure 6.9 Line Pressure Spikes when Outlet Valves are pulse-width modulated

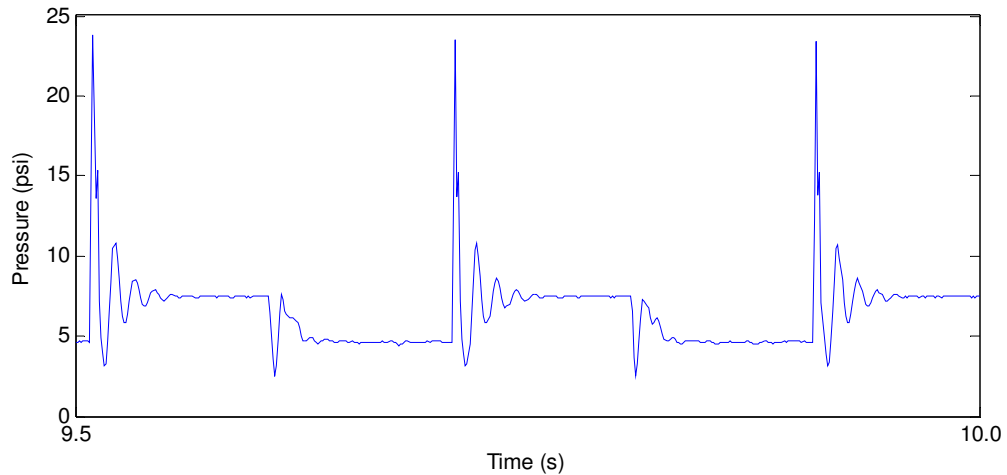


Figure 6.10 Line Pressure Spikes when Outlet Valves are pulse-width modulated (zoomed)

A force sensor was used to measure the actuator force when the inlet and outlet valves are pulse width modulated to observe if the fluctuations from the line have any similar undesirable effect that will be transferred. Figure 6.11 clearly shows that for several inlet/outlet duty ratios, the actuator forces show similar fluctuations. This effect is undesirable for haptic feedback as the feeling of realism is removed due to high frequency fluctuations.

From the experiments, when the outlet valve is pulsed, the water hammer effect will transfer to the actuator as shown in Figure 6.11, where the force sensor output clearly shows the fluctuations. When only the input valve is pulsed and outlet valve is shut, no fluctuations occurred. The conclusion is that the outlet valve causes massive pressure drop that transfers to force fluctuations that can be felt by the user.

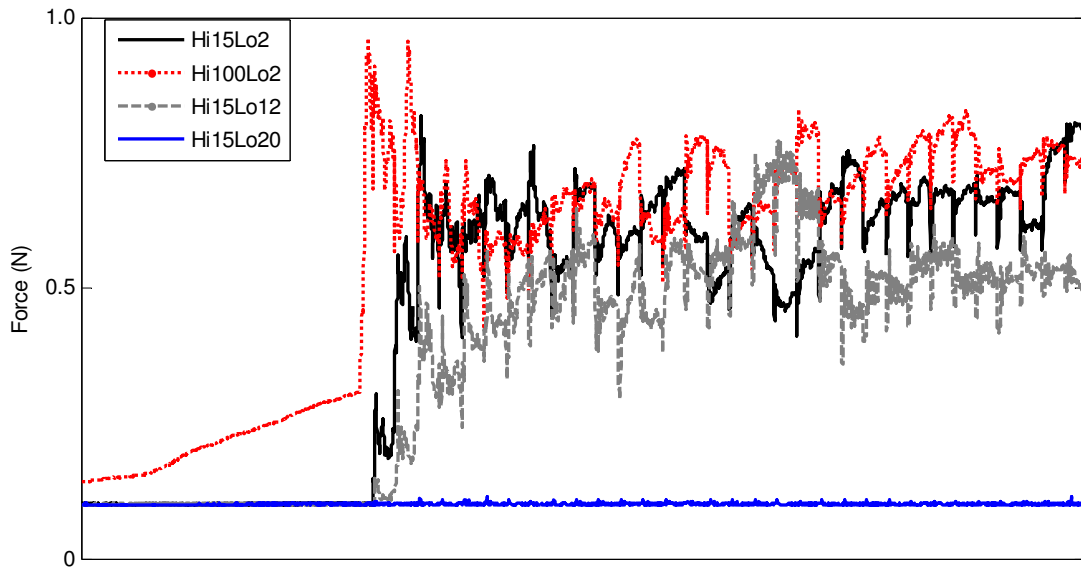


Figure 6.11 Actuator Force Subject to Inlet/Outlet Valves Under PWM

The most common solution is to increase the base frequency of the PWM to remove any water hammer effect, but as observed, any higher frequency would clearly exceed the operating limit of the inlet and outlet source selection valves by overheating the solenoid. Thus alternative to the valves currently used will be investigated.

6.1.4 Micro-miniature Valves for Pressure Control

The alternative solution investigated will be to replace the larger inlet/outlet source selection valves with the smaller micro-miniature valves currently used in Digital Clay for flow control of actuator array. These valves are made by the LEE Company and have a much faster response time of 1~2ms and higher bandwidth compared to the larger valves (>5ms). This will presumably solve the problem of pressure fluctuation by

operating at a higher base frequency (100Hz). However, as the smaller valves have a much lower flow rate of ~6 ml/s compared to the larger valves with larger flow rate of ~37ml/s, hence two of the same valves will be used in parallel for inlet flow and two for outlet flow respectively. To retain the capability of higher flow rate into and out of the system, the smaller valves for pressure control will be connected in parallel to the larger valves. The following figure will explain the concept in greater detail.

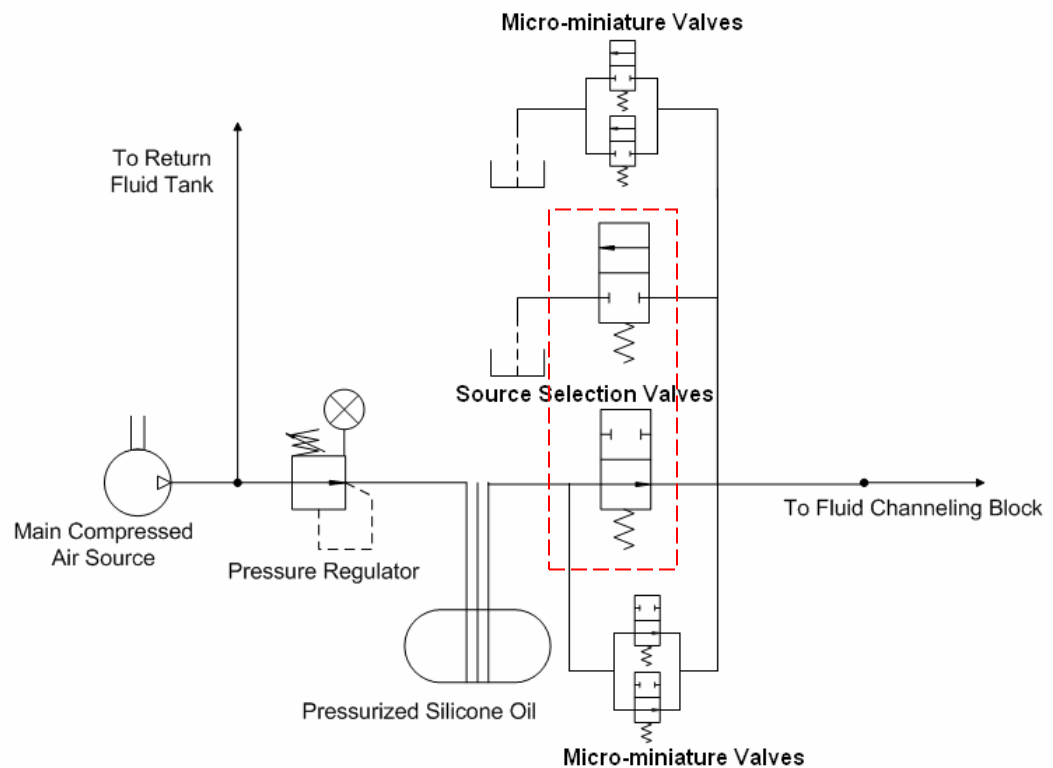


Figure 6.12 Micro-miniature Valves Placed in Parallel with Source Selection Valves

A set of two micro-miniature valves are mounted on a specialized mounting block and is made from aluminum that has channels to merge both the input and output of the two valves. This enables the two micro-miniature valves to be actuated simultaneously to

act as a single controllable flow orifice. One set is connected as an alternative inlet to the Digital Clay system via the fluid channeling block and a second set is connected as an alternative outlet from the system. So in total there are four valves that are connected in parallel to achieve this target. As mentioned, the source selection valves are retained for high inlet/outlet flow function, while the micro-miniature valves sets are especially for pressure regulation. Figure 6.13 shows the CAD model of the valves mounted on the specialized mounting block.

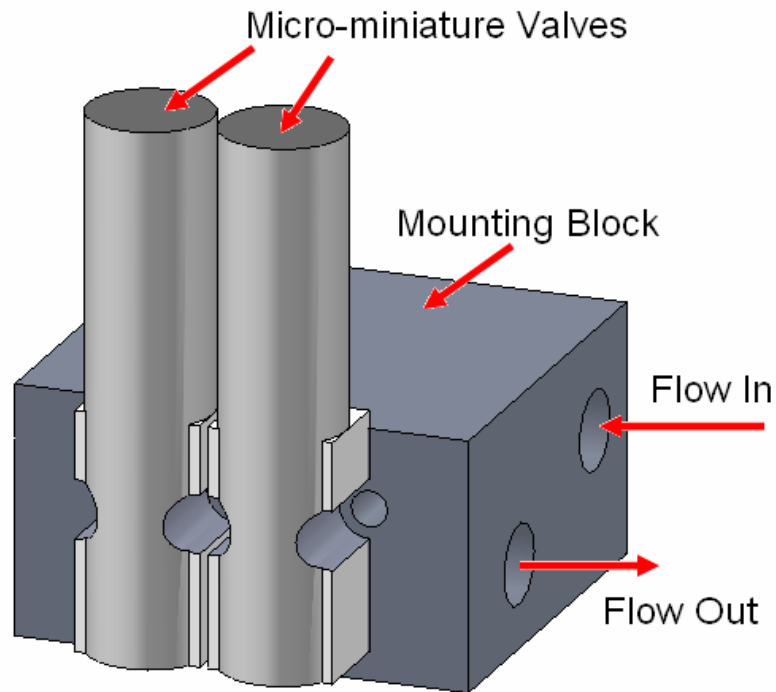


Figure 6.13 Micro-miniature Valves in Parallel Acting as a Single Variable Flow Orifice

To operate the valve digitally, a simple transistor circuit shown in Figure 6.14 was built to allow switching of the valve. The micro-miniature valves will be pulse-width modulated at 100Hz @ 12V to control flow. This base frequency is known to produce a linear PWM vs. Flow curve as shown from Chapter 4.

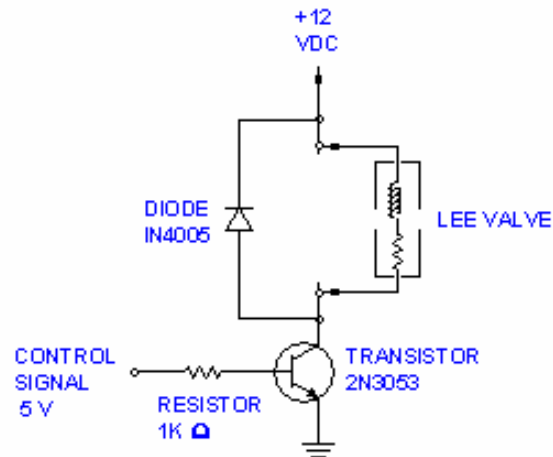


Figure 6.14 Transistor Switching Circuit for Micro-miniature Valves. Courtesy of LEE Company

To verify that the use of the micro-miniature valves reduces pressure fluctuations, the inlet and outlet are pulse-width modulated at 50% duty ratio and the line pressure monitored. Figure 6.15 shows that the amplitude of the pressure fluctuations is about 11psi, although still not satisfactory, is less than one half the pressure fluctuations when the larger source selection valves are used (27psi).

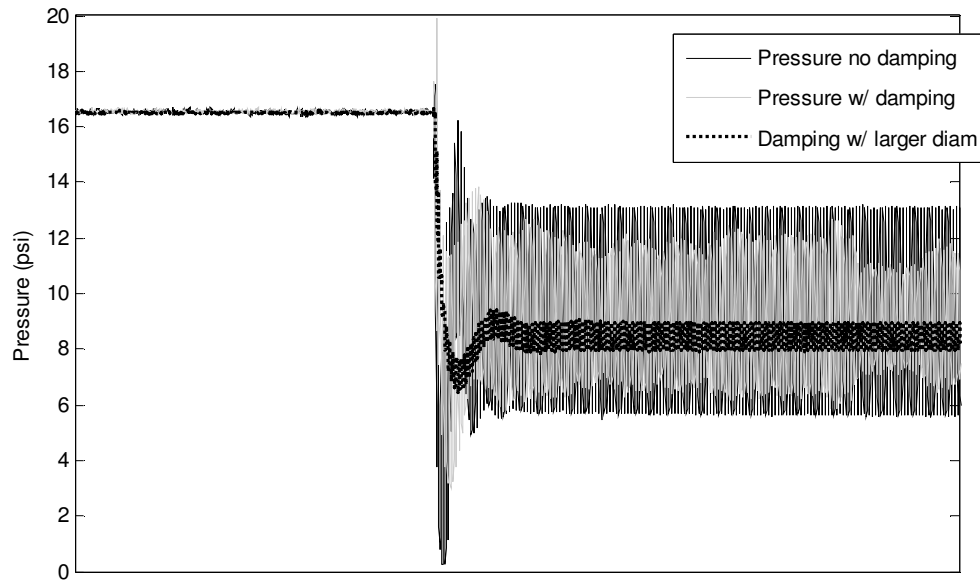


Figure 6.15 Line Pressure when Micro-miniature Valves Used as Flow Restrictor

To suppress the vibration amplitude even more, a simple and improvised fluid damper/accumulator is connected to the line. Typically in industry where systems are operating at a much higher pressure and the effects of pressure fluctuations is undesirable, a bladder type accumulator is used to dampen the pressure spikes. Figure 6.16 shows the construction of a simple fluid damper/accumulator adapted from a typical industrial pulse damper.

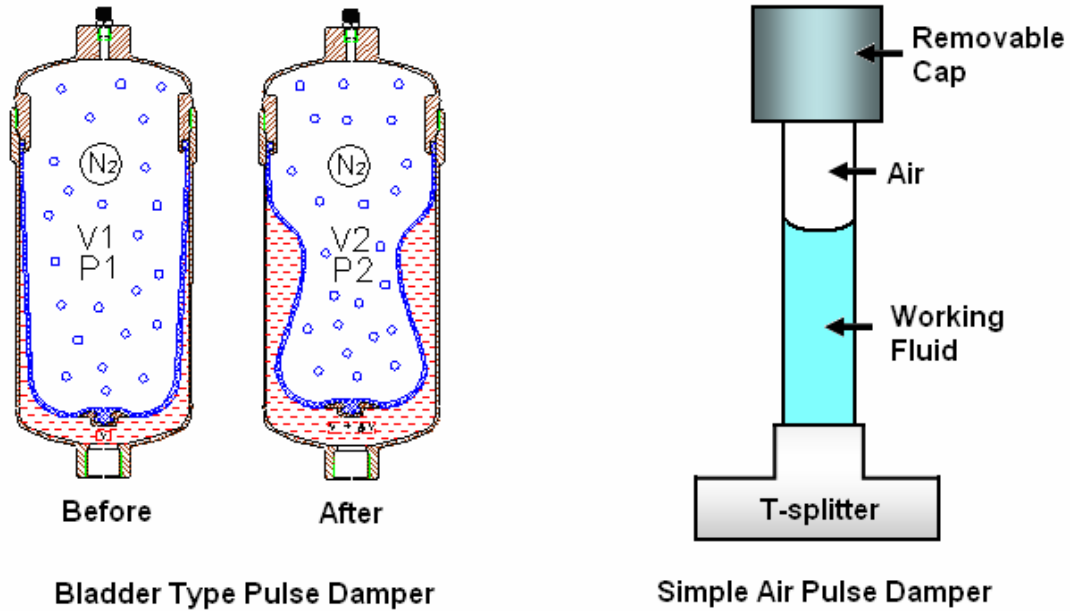


Figure 6.16 Bladder Type Pulse Damper (right) courtesy of HIDRACAR S.A. and Simple Air Pulse Damper (left)

The simple air pulse damper used for Digital Clay consists of a vertical rigid tube filled with working fluid except for a small amount of air trapped at the top. This is adapted from a typical bladder type pulse damper which uses Nitrogen gas and a layer of membrane to separate the gas from the working fluid. Looking back to Figure 6.15, the amplitude of pressure fluctuation with damper in the line was successfully reduces to less than 2psi. The use of a slightly larger inner diameter tube for pulse damper was able to reduce pressure fluctuation amplitude to about 1psi.

For feedback control purposes, a ten data point running average filter is applied to the pressure sensor output to obtain a smooth signal. Figure 6.17 shows the pressure signal for feedback control.

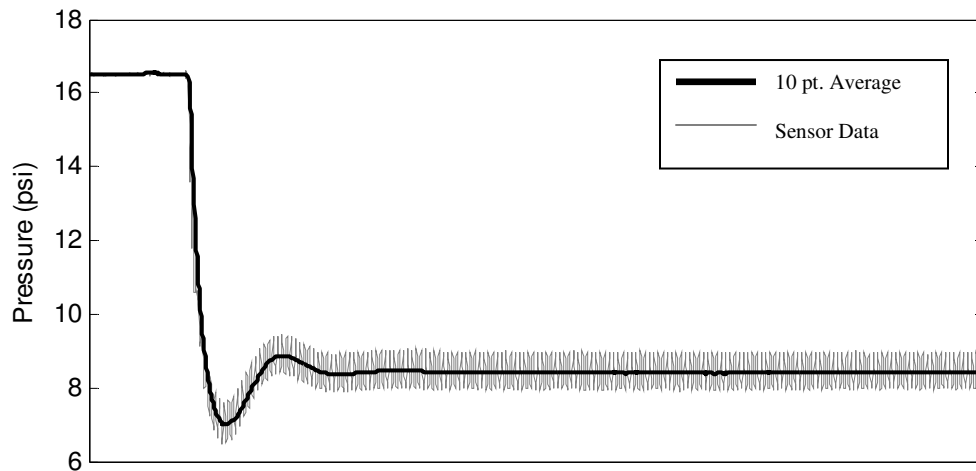


Figure 6.17 Ten Point Running Average to Smooth Pressure Feedback Signal

Figure 6.18 shows the pressure build up in the line has small pressure ripple but after applying the moving average filter, produces a smooth signal for feedback control.

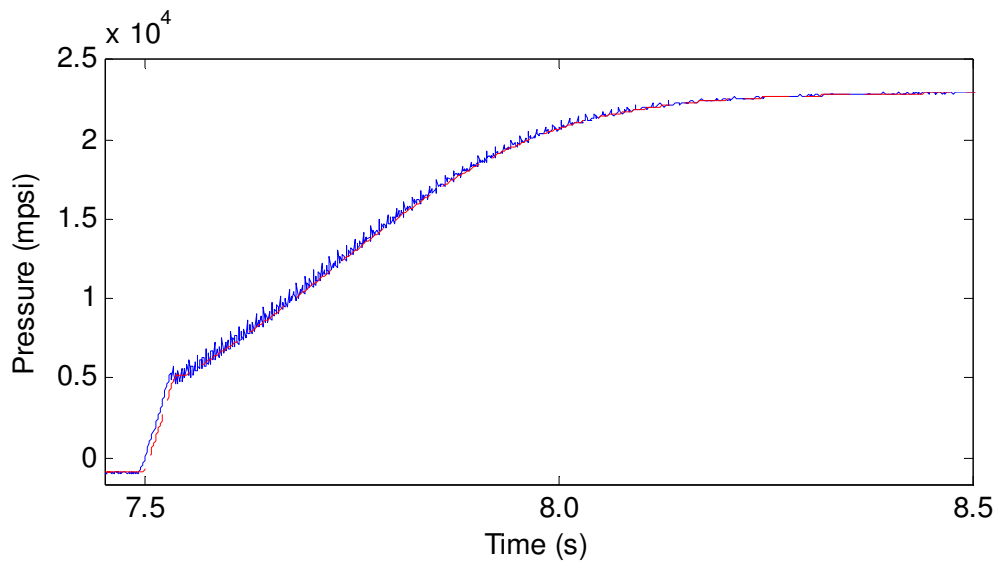


Figure 6.18 Line Pressure Build-up Before (Solid) and After (Dashed) Moving Average Filter

6.2 Pressure Control Law Design

Based on the simulation performed, the control law for closed-loop pressure regulation will have the following algorithm,

$$Duty_{\text{feedforward}} = K_{\text{ff}} \times \text{Desired Pressure} \quad (6.12)$$

$$Duty_{\text{feedback}} = K_p \times \text{Error} + K_i \times \int \text{Error} dt, \text{ if Error} \leq 0 \quad (6.13)$$

$$Duty_{\text{feedback}} = 0, \text{ if Error} > 0 \quad (6.14)$$

where Error = Desired Pressure – Pressure.

The inlet duty ratio is proportional to the desired pressure while a proportional-integral law determines outlet duty ratio. The outlet duty ratio is limited to the outlet duty ratio as, if

$$\begin{aligned} &\text{if } Duty_{\text{feedback}} \geq Duty_{\text{feedforward}} \\ &\text{then } Duty_{\text{feedback}} = Duty_{\text{feedforward}} \end{aligned} \quad (6.15)$$

This is to limit the outlet flow beyond what is necessary. If both the inlet and outlet flow rate is the same, the system pressure would stay at atmospheric pressure, or 0psi. If the system pressure is less than the desired pressure, the outlet flow would be shut off and allowing the system pressure to build.

This control law is applied to the experimental set up shown in Figure 6.12. Initially, only proportional feedback control is applied to examine the behavior of the system. The feedforward gain is $K_{ff} = 3.0$ while the proportional feedback gain is $K_P = 0.025$. Figure 6.19 shows the system pressure tracking a 15psi step desired pressure, the error and the outlet duty ratio.

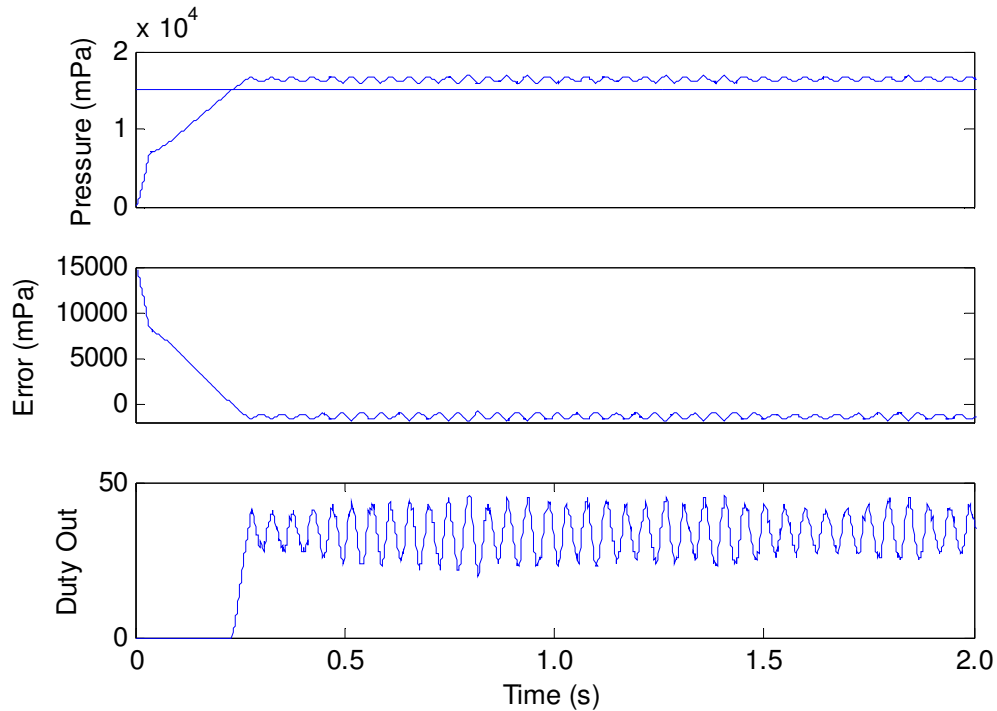


Figure 6.19 Closed-loop System Pressure Control with Proportional Feedback

For control law with only proportional feedback gain, the pressure tracking exhibits steady state error as expected. There was also slight oscillation observed. With the added integral gain, $K_I = 0.000015$ and reducing proportional gain, $K_P = 0.020$, the pressure oscillation was eliminated, while more importantly at the same time, reducing steady state error. Figure 6.20 shows the system pressure response. The rise time is ~ 0.25 seconds and settling time ~ 2.5 seconds. Although it is desirable to decrease both the rise

time and the settling time, the system pressure would become unstable if the feedforward gain is increased beyond 3.0. Also, the pressure control algorithm would lose its robustness. The trade-off between system performance and stability/robustness is dependent on the application, which in the case of Digital Clay, robustness has a higher priority.

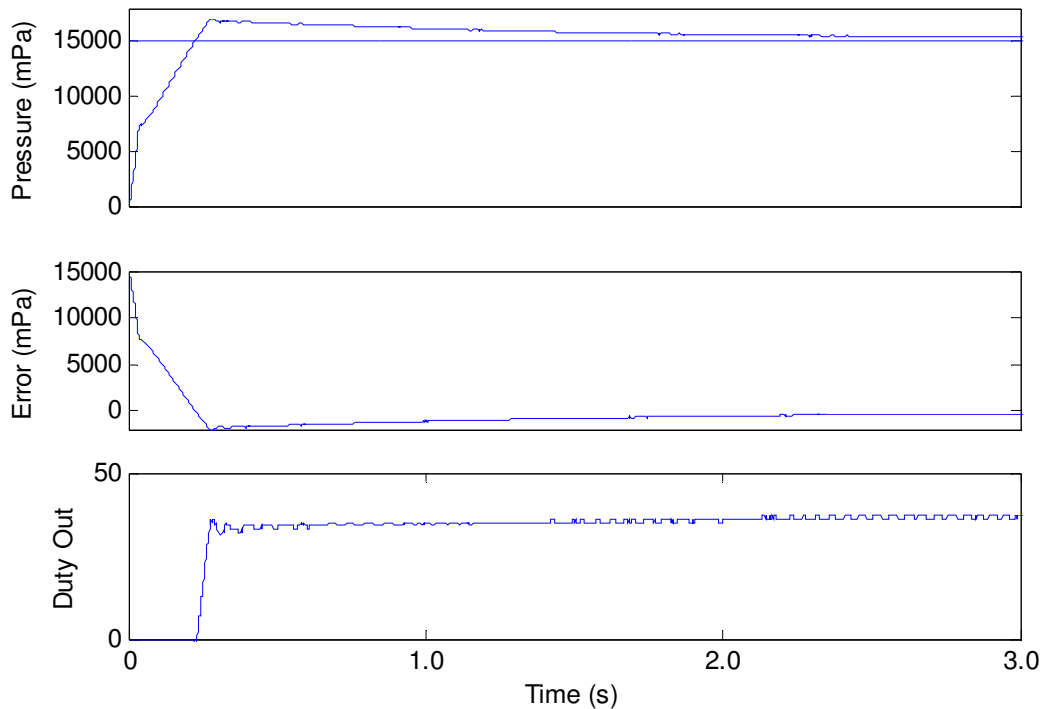


Figure 6.20 Closed-loop System Pressure Control with Proportional-Integral Feedback

Figure 6.21 shows the system pressure tracking of 15psi, 18psi, 21psi and 23psi step command, while Figure 6.22 shows performance for a 1Hz sine wave pressure the tracking. For a relatively simple control law such as the proportional feedforward and PI feedback used, the tracking of step profile and sine profile is satisfactory. The settling time of the step response is about 2 seconds which is slow for effective haptic feedback. This is due to the fact that the stability margin is low for the simple PI controller. If the

feedforward and feedback proportional gains are increased to reduce settling time, the controller is not able to stabilize the pressure tracking as shown in Figure 6.23 and Figure 6.24. The use of a more robust controller is therefore desired.

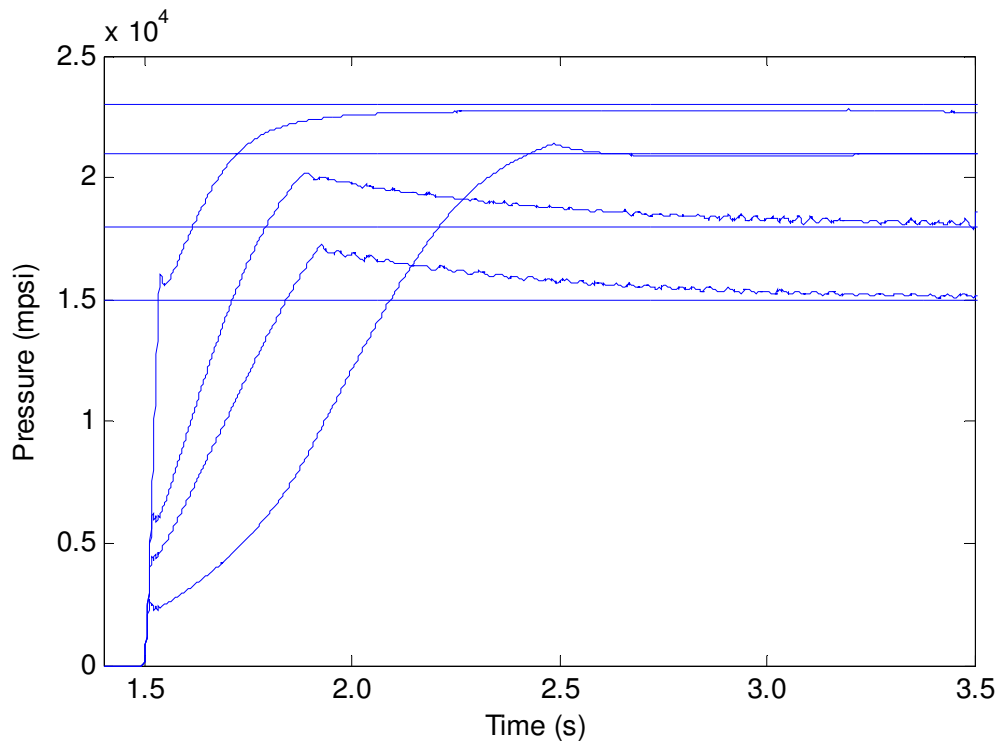


Figure 6.21 Closed-loop System Pressure Control for Various Desired Pressure (15psi, 18psi, 21psi and 23psi)

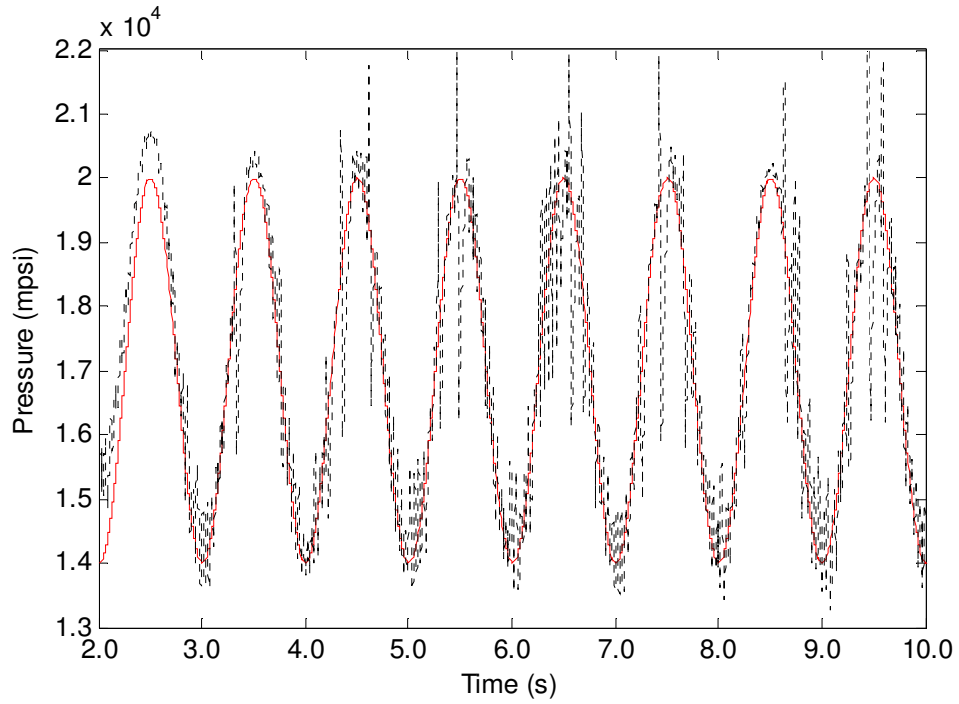


Figure 6.22 Closed-loop System Pressure Control for 1Hz Sine Wave Tracking

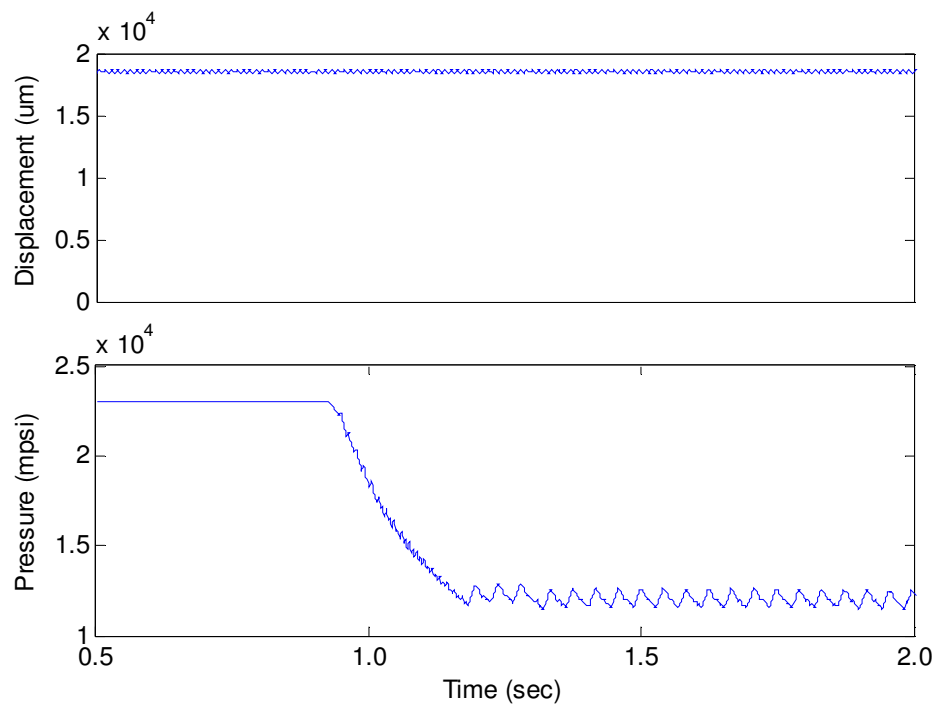


Figure 6.23 Closed Loop Pressure Control with Faster Settling Time but Unstable

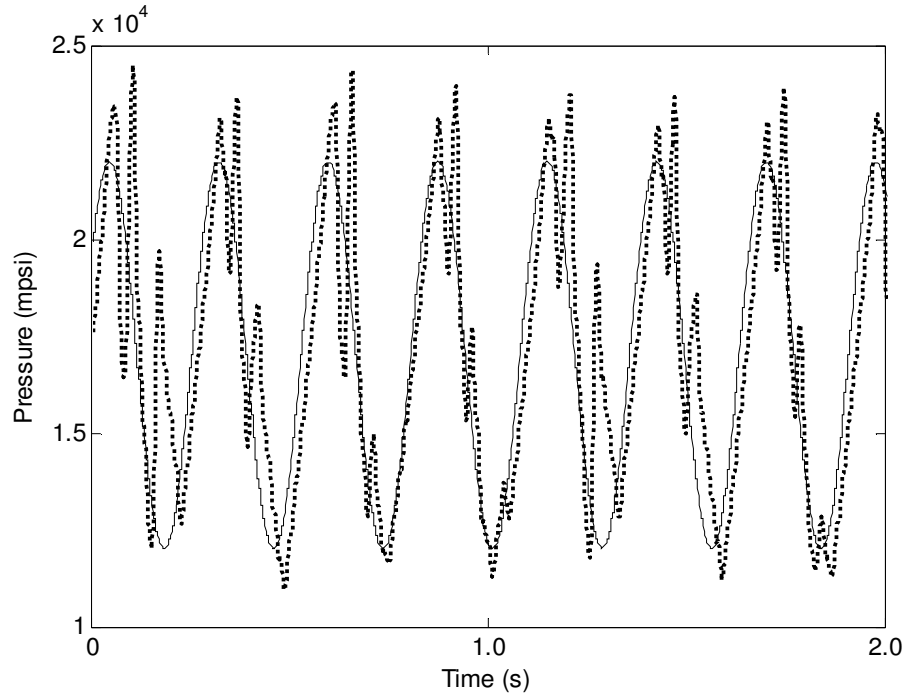


Figure 6.24 Closed Loop Pressure Control 4Hz Sine Wave Tracking but Unstable

6.3 Remarks and Discussion

In this chapter, the possibility of electronically controlling system pressure is investigated and a novel approach is presented. This method controls the flow in proportionally and the flow out of the system with a PI control using feedback signal provided by a pressure sensor connected just before the working fluid enters the channeling blocks. Only one pressure sensor is used in an attempt to maintain the low number of hardware and costs for the future product. The use of the existing inlet and outlet valves are found to be causing water hammer effect and pressure fluctuations due to the slow dynamics. Therefore two micro-miniature valves are connected in parallel via a custom fluid channeling block to form a single variable orifice; one for the inlet and one for the outlet respectively. This approach is able to provide pressure control that is low in

fluctuations and has a higher controller bandwidth. However, there is still physical limitation to the bandwidth of the PI controller, which is currently about 1Hz. Therefore future work could be done on designing and implementing a controller which would increase the system stability margin. Although this method only varies the system pressure, it will be shown in the next chapter that with a hot area processing ability, only one pressure feedback will be needed at a single time to provide haptic sensation to the user. With this, all the tools for admittance and impedance haptic control method are available.

CHAPTER 7 DIGITAL CLAY HAPTIC CONTROL REALIZATION

The works presented in the previous chapters are building blocks to the realization of Digital Clay as an effective haptic human machine interface. Unlike the more common point-like haptic devices such as PHANTOM for one, Digital Clay is potentially a haptic and visual surface. The displacement and velocity control presented in Chapter 3 together with the external force observer researched in Chapter 5 are tools to implement the admittance mode haptic capabilities. The novel system pressure regulation method presented in Chapter 6 offers another alternative solution of haptic interface, the impedance mode. The robust and accurate displacement sensor's embedded actuators are used to the advantage for both of these haptic modes. A more detail look into the two types of haptic modes will follow. This chapter will endeavor to first realizing both types of haptic modes on a single actuator case before proceeding with the 5x5 prototype case. The work done up to this chapter has only been focused on the single actuator case. Because the surface control is more complicated and has its own performance limitations compared to the simpler and more straightforward single actuator control, the approach will be slightly different, however still utilizing most of the tools and methods studied using the single actuator case. The limitations and challenges are discussed at the end of the chapter.

7.1 Overview of Haptic Modes

7.1.1 Admittance Mode Haptics

The admittance mode of haptic realization measures force exerted by the user on the master device, either estimated or with a sensor, and controls displacement and/or velocity of the device to give a virtual sensation. This haptic control mode is typically used in larger workspaces that require higher force. The user will feel as if the virtual environment is being interacted with “admits” with certain amount of displacement and rate depending on the force. For example, a point on the virtual environment that has a linear spring-like behavior would displace $x = F/k$, when subjected to a force F . To simulate free space, the device would have to move with very fast motion at low forces; which requires high control gain. Stability could be an issue if the virtual inertia is low. To simulate stiffness, the device would have to be passively much stiffer than user exerted force. For the case of Digital Clay, the advantages of using this method is the current ability to control actuator position and velocity accurately. The observer from Chapter 5 is used to estimate user force. Also, there is no need of extra pressure sensors to perform closed-loop control – hence reduce cost and complexity. And as will be shown later, the current strategy of controlling actuators in the 5x5 array will not require significant algorithm changes to implement admittance mode haptic control. Some of the disadvantages are the limitation of the current force observer in estimating force when velocity is near zero. Displacement and velocity control has to be performed independently of force estimation because of the dependence of both algorithms on displacement information. Furthermore, displacement control has to be performed separately from force estimation at any sampling instance; intermittently with time.

7.1.2 Impedance Mode Haptics

This mode of haptic realization measures displacement and/or velocity imposed by the user on the master device, either with a sensor or estimated and controls the force of the device that the user feels to give a virtual sensation. This type of haptic control is the most common for its cheap and easy implementation in smaller and lower cost devices. The user will feel the virtual environment being interacted with “impede” a certain degree of force dependent on the displacement. For example, a point on the virtual environment that has a linear spring-like behavior would exert a force $F = kx$, when subjected to displacement x . For a model of virtual environment with viscous damping added, the impedance force would be $F = kx + bv$, when subjected to displacement x and velocity v . To simulate free space, the device ideally needs to have very low actuator friction. The simulation of stiff environment would require that the device be able to exert a force much higher than the user exerted force. This requires high control gain at low displacement, and could be a stability issue. For the case of Digital Clay, the advantages of using this method is the current ability to measure displacement and estimate velocity of the actuator with high accuracy. As the pressure control from Chapter 6 is independent from displacement measurement, this type of control is continuous compared to the admittance type. This will result in a more realistic virtual sensation. The disadvantages are as there is essentially only one pressure sensor and the system pressure is controlled, the user can only feel a single pressure feedback. Essentially, a more sophisticated surface-level algorithm, called the hot area programming is needed to get around this limitation.

7.2 Digital Clay Single Actuator Case

7.2.1 Admittance Control

At the start of the admittance haptic control mode, the actuator will maintain its initial displacement from shape display mode. After the actuator has reached steady state displacement, the haptic control is activated. The program will loop with the following lines of code:

```
//-----Elastic Simulation-----  
k = 0.015; //Virtual Stiffness in N/mm  
b = 0.0006; //Virtual Damping in N/mm/s  
Displace = Eq - (double)F/(k); //Desired displacement  
VDesired = -(double)F/(b); //Desired velocity  
ttau = (Displace)/VDesired; //seconds  
tau = abs(tt)*1000000000; //nano seconds  
  
if(ve < -5000){  
    vcontrol = 1;  
    required.tv_sec = 0;  
    required.tv_nsec = tau; //Time Delay  
    nanosleep(&required, &remain);  
}  
else {vcontrol =-1;}
```

The force estimation, “ F ” is divided by the virtual stiffness parameter, “ k ” to obtain a desired change in displacement. The displacement command to the controller, “ $Displace$ ” is defined as the difference between the initial equilibrium position, “ Eq ” and the desired change in displacement from the virtual stiffness. A virtual damping, “ b ” is added by calculating the desired velocity, “ $VDesired$ ” from user exerted force. The actuator velocity will be controlled to track this desired velocity for a time period, “ tau ” obtained by the ratio of the desired displacement to the desired velocity. This will generate a triangular displacement profile at constant velocity that is dependent on the force exerted

by the user. If the user is not pushing down on the actuator, the control will switch to displacement control where it will always spring back to equilibrium position.

The implementation of this haptic control mode for two different virtual stiffness is shown by the plots of actuator displacement and estimated and measured force on the actuator in Figure 7.1 and Figure 7.2. A force sensing resistor is attached on the actuator pin to measure actual finger force.

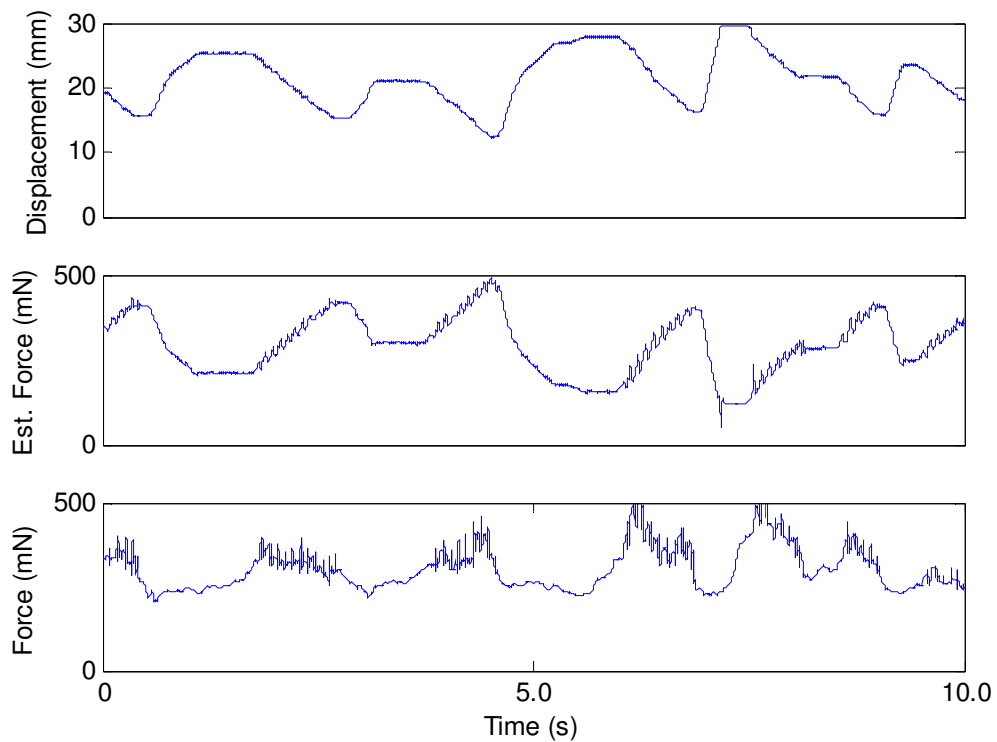


Figure 7.1 Admittance Haptic Control Simulation for Virtual Stiffness = 0.015N/mm

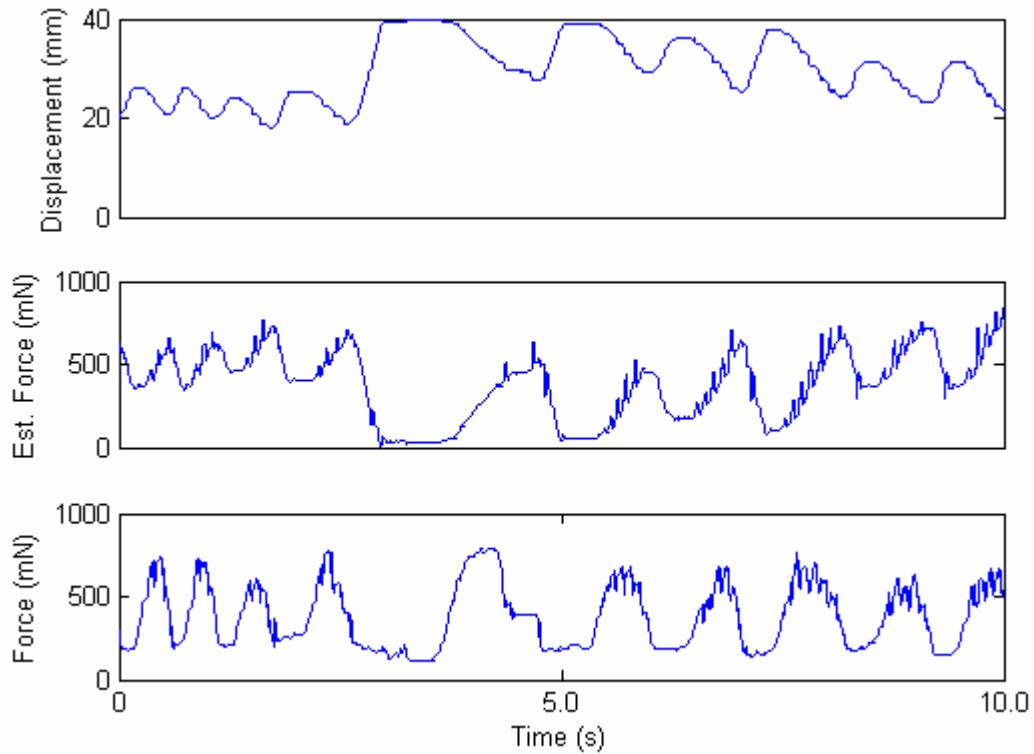


Figure 7.2 Admittance Haptic Control Simulation for Virtual Stiffness = 0.06N/mm

From the two figures, the actual force felt by the user finger is as expected to be, higher for the higher stiffness simulation. The limitation encountered for this haptic control mode is the discontinuity in actuator displacement due to the method of controlling actuator velocity and waiting for a time period and to allow for force estimation. As seen from Figure 7.3, the actual force that is felt by the user exhibits intermittent changes in between force estimation and motion control for both of the stiffness simulations. If the time delay is small enough in between force estimation and velocity control, the discontinuity effect can be eliminated and the user will perceive the movement of the actuator pin as relatively smooth.

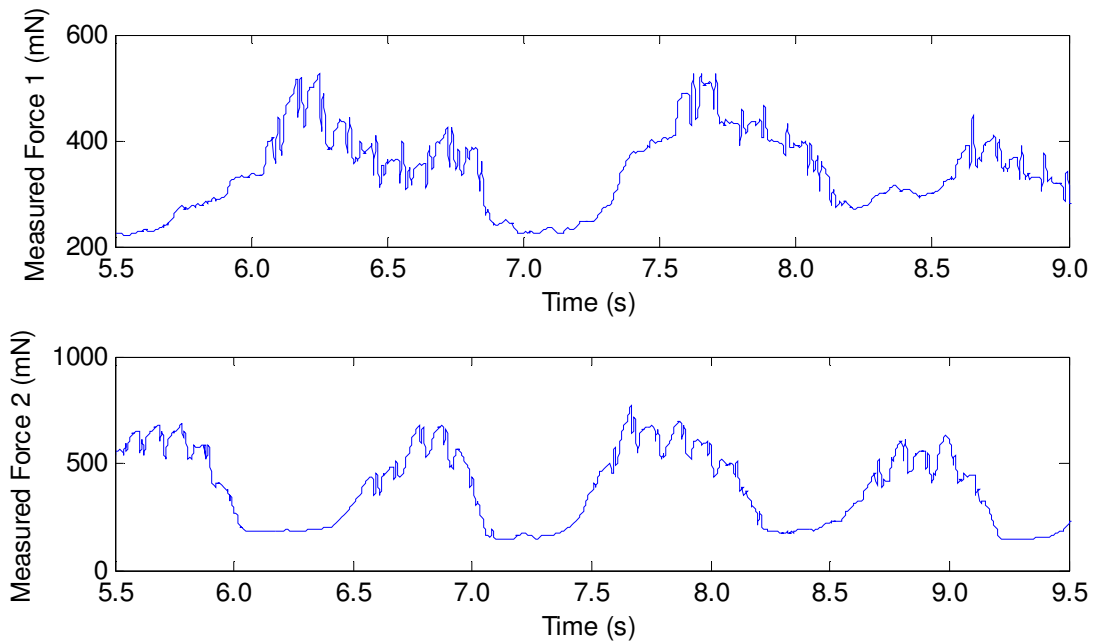


Figure 7.3 Measured Force on User Finger for both Stiffness Simulations (Zoomed In)

7.2.2 Impedance Control

At the start of the impedance haptic control mode, the actuator will maintain its initial displacement from shape display mode. It is important that at this stage, the pressure can be varied without error in the displacement of the actuator. The supply pressure at shape display is at the maximum of 25psi to obtain the fastest response to displacement control for shape display. When the haptic mode is activated, it is desirable that the actuator pressure be as low as possible to simulate free space or initial stiffness of a certain material property but at the same time still able to maintain the displacement; in other words, to maintain equilibrium of the actuator piston. As the control for displacement and pressure depends on different sets of valves, this can be achieved as long as static force equilibrium is maintained. The displacement control valves will

control the flow leading to the actuators independent of the valves that are controlling system pressure. As Figure 7.4 shows, when a sinusoidal pressure is being tracked by the system pressure controller, the displacement of the (0,0) actuator is being kept constant at 20mm.

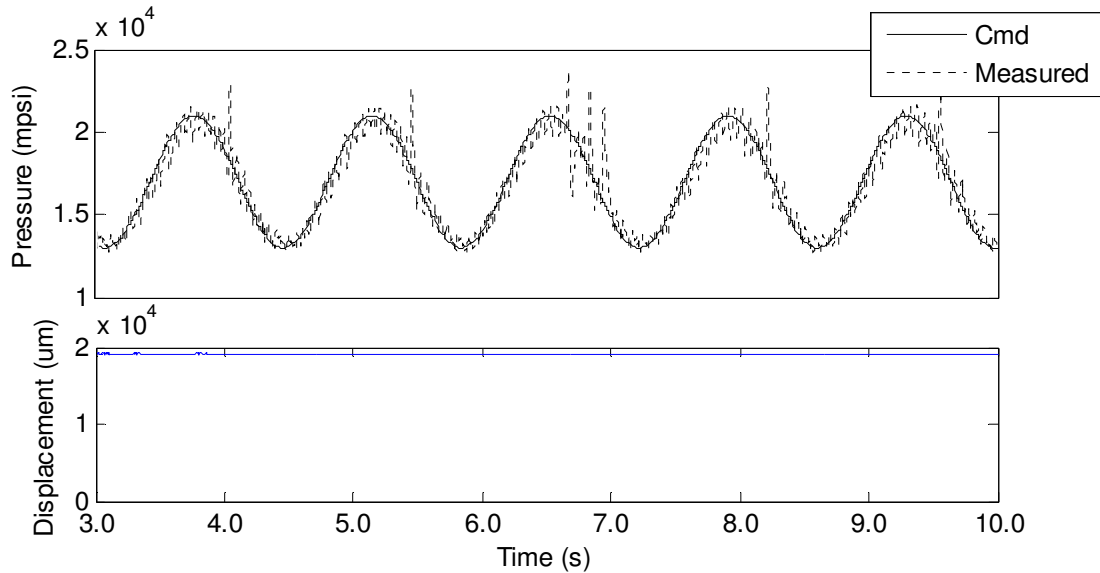


Figure 7.4 Sinusoidal Pressure Tracking Keeping Displacement Constant

Hence the impedance haptic control mode can be implemented on the single actuator of Digital Clay by controlling the force to be proportional to the displacement difference from equilibrium. For this prototype, the maximum actuator pressure is 23psi or about 1.3N. This proof of concept experiment sets the range of actuator force to be at 1.3N at maximum to 12psi or 0.7N at minimum. 12psi is the minimum pressure to maintain actuator equilibrium as the return pressure is 10psi and the weight of the actuator rod is 14.5g. Hence for a displacement range of 20mm, the virtual stiffness for this experiment is 0.03N/mm or 30 N/m.

The software code for the impedance mode of a single actuator is as follows:

```
Desired = 20*1000; //Initial Equilibrium Position (mm)
Error = Desired - DSP[x*5+y]; //Change from Equilibrium Position (mm)
k = 0.00055; //Virtual Stiffness mpsi/um
//-----Elastic Simulation-----
    Pcontrol = 1;
    UnfilteredP = 12000 + error*(double)k;

///-----2nd Order Butterworth Filter-----
    Desired_Pressure = 1.956*(double)pf1 - 0.957*(double)pf2 +
0.000241*(double)UnfilteredP + 0.000483*(double)p1 +
0.000241*(double)p2;
    pf2 = pf1;
    pf1 = Desired_Pressure;
    p2 = p1;
    p1 = UnfilteredP;
```

The actuator is first controlled to an initial equilibrium position, “*Desired*” with the displacement controller. A virtual stiffness parameter, “*k*” will be used to calculate the desired pressure in the system, “*UnfilteredP*” due to change from the equilibrium position, “*error*”. The initial pressure in the system is 12psi less the 10psi return pressure, thus the user will feel a simulation of “free motion” at low displacement error. To remove high frequency components from the desired pressure due to digitization in displacement measurement, a second order low pass filter is applied and the variable “*Desired_Pressure*” will be sent to the pressure controller thread. Figure 7.5 shows the displacement of the actuator as a user is pushing on it and the tracking of a pressure profile that is proportional to the displacement error. The equilibrium displacement of the actuator is 20mm.

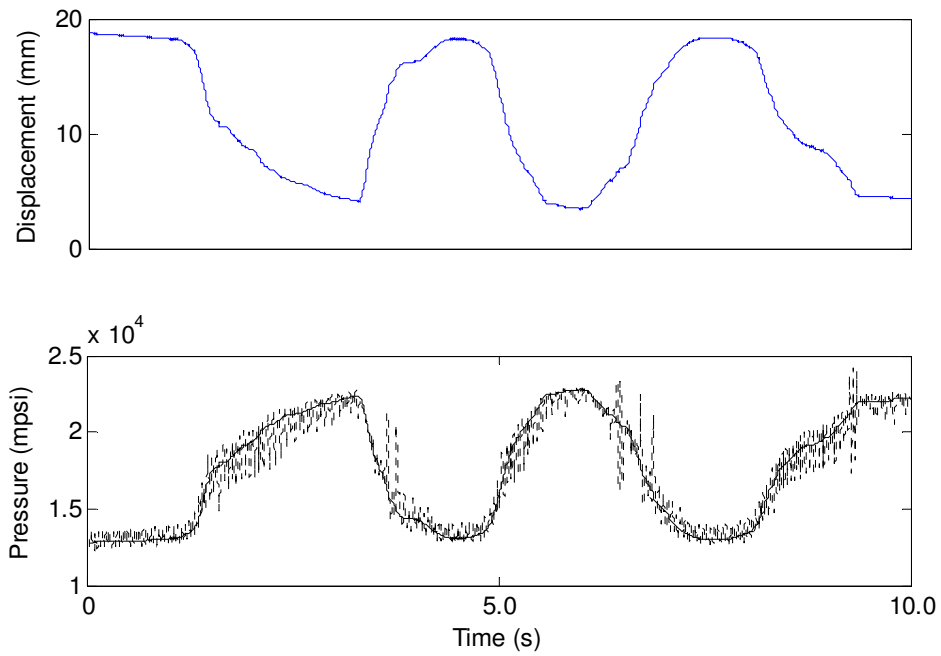


Figure 7.5 Impedance Haptic Control for Actuator with Virtual Stiffness of 0.03N/mm (Slow Rate)

If the user pushes on the actuator with a slow rate, the pressure tracking is relatively smooth. However as highlighted from the previous chapter that as the controller bandwidth is quite low, if the user pushes on the actuator with a faster rate the pressure tracking becomes marginally unstable as illustrated in Figure 7.6.

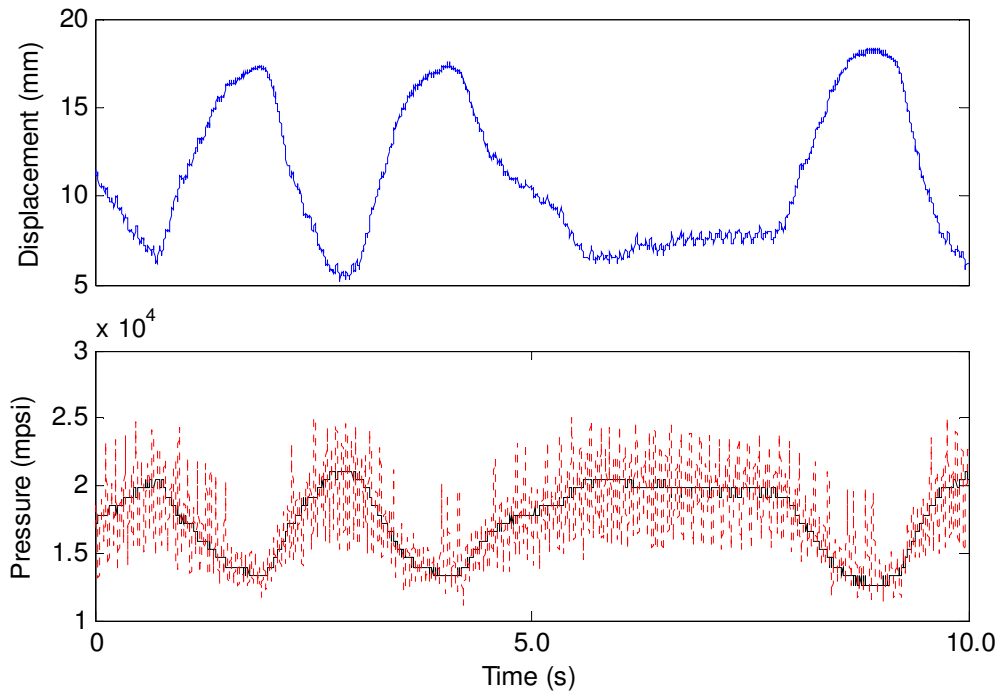


Figure 7.6 Impedance Haptic Control for Actuator with Virtual Stiffness of 0.03N/mm (Fast Rate)

A low pass filter is applied to the pressure profile to remove high frequency components (sharp edges) such that the system bandwidth is not exceeded. The result is a more stable pressure response, which is crucial to provide realistic haptic feedback to the user. Figure 7.7 shows the filtered profile pressure response. There is still marginal stability observed at higher desired pressure. This remains as the limitation to this feedback controlled system for now. The limitation is due to the simple nature of the controller and the difficulty of pressure control for hydraulic systems. In the future, a more advanced controller can be implemented to increase the stability margin of the feedback controlled system.

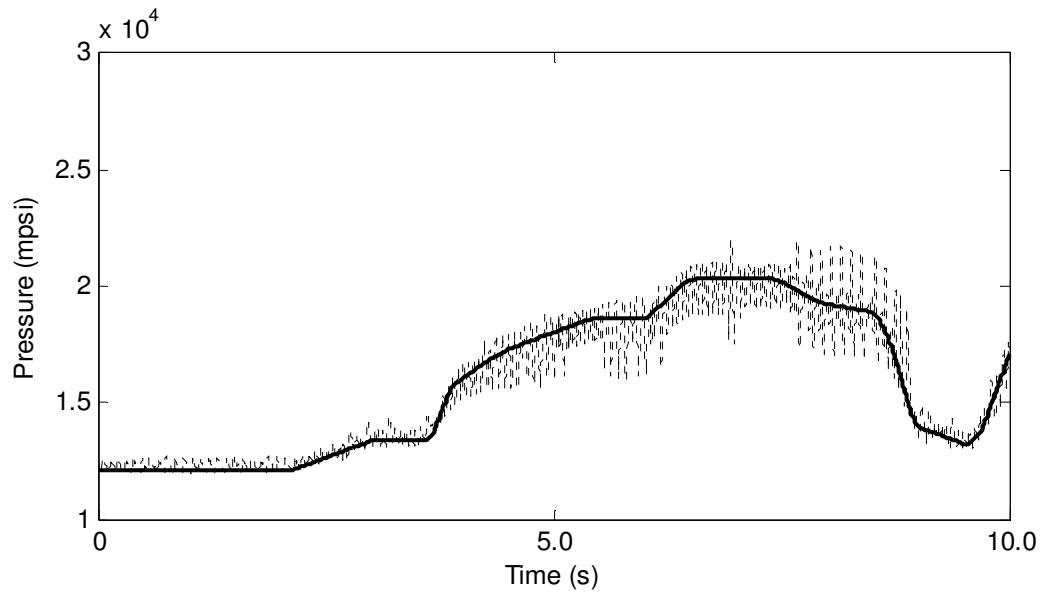


Figure 7.7 Impedance Haptic Control for Actuator (Filtered Profile)

7.2.3 Shaping Mode of Digital Clay

As a two-way haptic communication device, Digital Clay should have the capability to allow the user to haptically input desired shape. Therefore a shaping state can be added to provide that capability. As seen from both the haptic control methods, the impedance control provides a continuous feedback to the user as opposed to the admittance control. Therefore the shaping state will be based on the impedance control.

The general logic diagram of the shaping state is given as follows:

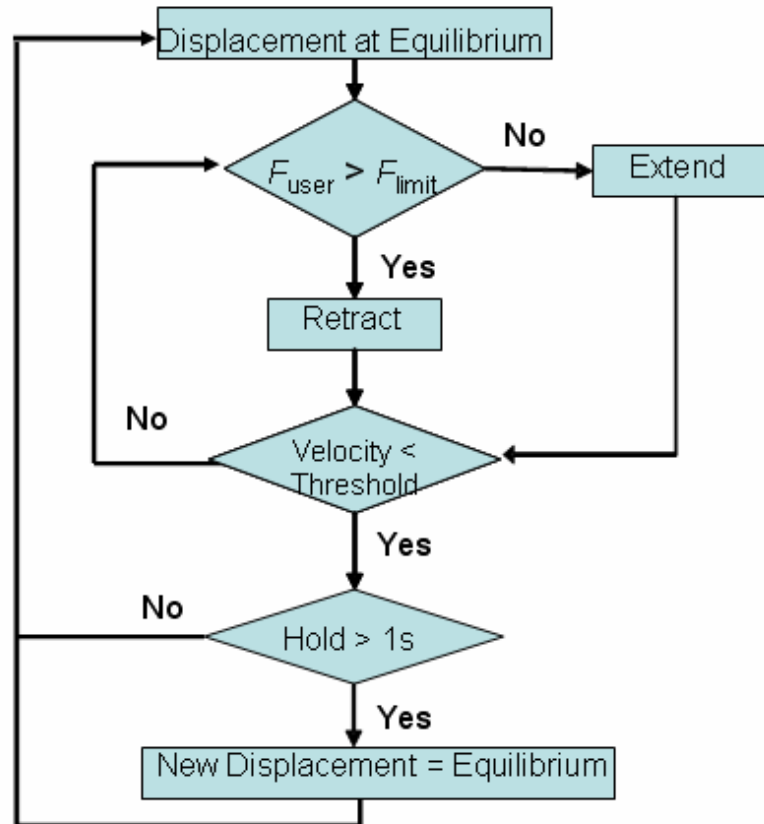


Figure 7.8 Digital Clay Actuator Shaping Algorithm

At the start of shaping mode, the actuator displacement is controlled to a preset equilibrium. Then the system pressure is controlled to 12psi or a low reference value. Naturally, if the user exerted force is greater than the actuator force, then the pin will retract or it will extend if a lower force is exerted. The program will start to count the time when user holds the actuator still. If the hold time is more than one second, a new equilibrium displacement equal to the last position of the actuator will be recorded as the new equilibrium. Then the process starts all over again. This mode enables setting and resetting of any actuator position on the array, similar to a clay, but with the added ability to “add” volume.

The software code for the shaping mode of a single actuator is as follows:

In the sampling thread,

```
if(ve<-5000) {Time1 = gethrtime();} //Save the time
at when the actuator velocity is less than treshold
else {Time0 = gethrtime();} //Initial Time before
the actuator velocity is less than treshold
Timediff = Time1 - Time0; //Time period when the actuator
Velocity is less than the treshold
```

The displacement and velocity of the pin are sampled every 1ms. The time duration when the pin velocity is less than 5mm/sec is recorded. This will enable the program to know when the user wants to fix the pin location. In the control thread, the displacement controller is actively controlling the current displacement to match desired displacement.

In the main thread,

```
//-----Shaping Of Pin-----
-
if(Shape<0){
    if(Timediff > 1000000000) {
        Desired = DSP[Y*5 +X]; //Read From Displacement Sensor
        //Set new position when holding finger for ~1 second
        Shape = 1;}
}
else if(Shape>0){
    if(ve<-10000){
        Desired = 20*1000;
        Shape = -1;} //Initial Equilibrium Position
}
```

When it is in shaping state, ($Shape = 1$), the program will check to see if user has fixed the pin for longer than ~1sec. If the time duration is $> 1s$, the pin displacement will be fixed at the last value. This value will be the new desired displacement for control. Now, in the shaping state, the program switches over to check if a velocity of user to the pin of greater than 10mm/sec is applied. This indicates that the user is moving the pin and would like to either add or subtract volume. When this happens, the desired displacement

will be reset to the initial equilibrium displacement to enable the user to add/subtract length to the pin. Figure 7.9 shows the shaping mode in action.

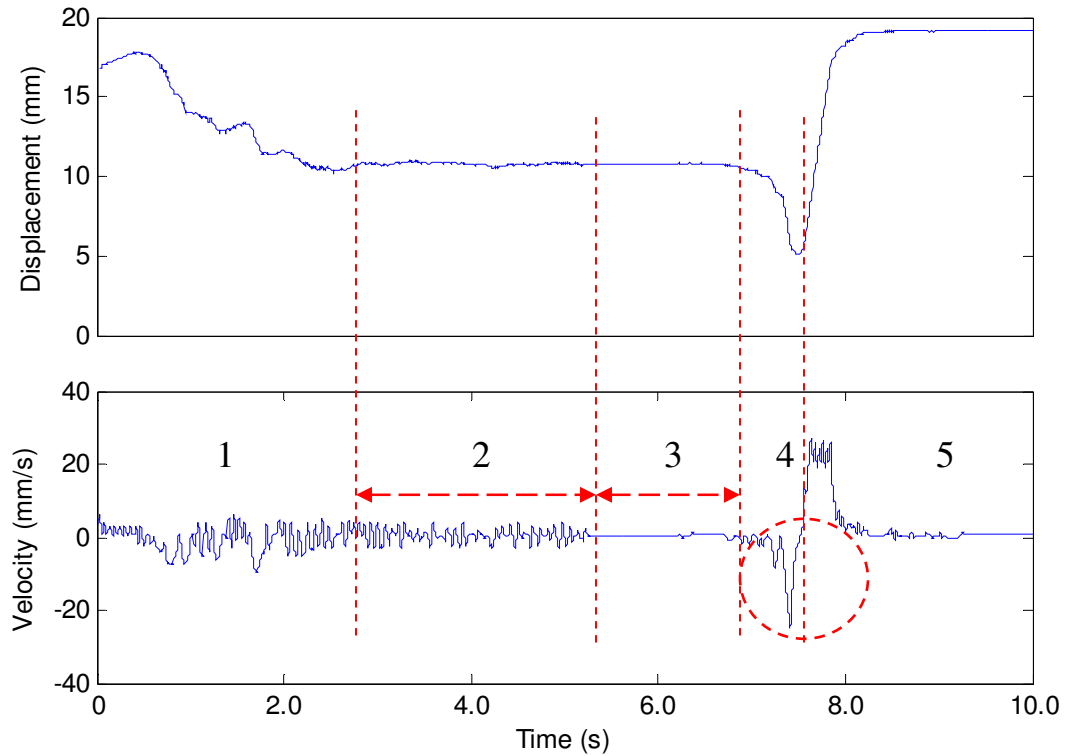


Figure 7.9 Actuator Displacement and Velocity Stages Before, During and After Shaping Mode

From the figure, the displacement and velocity of the actuator is shown before, during and after shaping state. In region 1, the user pushes the actuator pin downwards as indicated by the downward slope of displacement and the negative velocity. At region 2, the user tries to hold the actuator pin still to set the position as can be seen from the displacement of the actuator. Although the displacement seems to be constant, the velocity of the actuator in reality has an oscillation from finger vibration; therefore a dead-gap for zero velocity has to be defined to allow the actuator to be shaped. In region

3, the pin is set and the user finger is removed, as indicated by the constant displacement and zero velocity without oscillation. In region 4, the user tries to reset the actuator pin by pushing downwards on it, and in region 5, the user lets go of the actuator pin to reset to initial displacement.

7.3 Digital Clay 5x5 Array Case

7.3.1 Surface Generation Algorithm

As Digital Clay does not have a specific control valve for each actuator, a method of displaying the surface was developed by Zhu. It is dubbed the Surface Refresh Method. The refresh method consists of column refresh and row refresh stages. Figure 7.10 shows the location of both row and column control valves in the system relative to the actuators and control adapters.

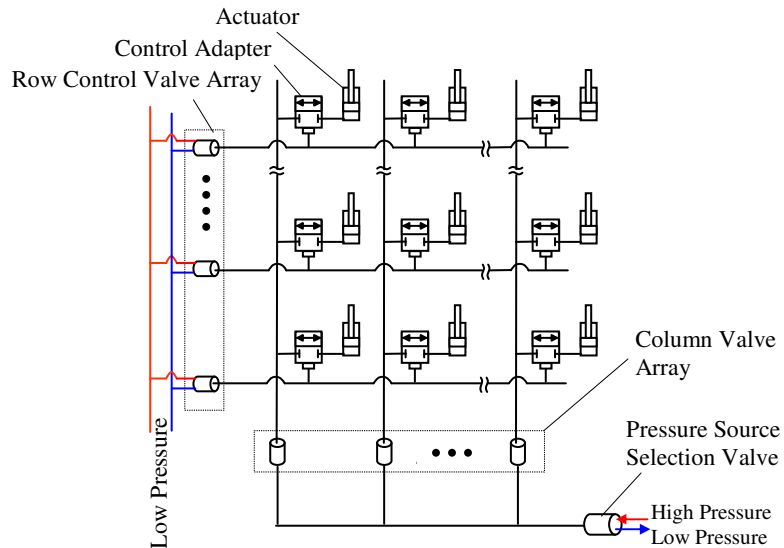


Figure 7.10 Locations of Row and Column Control Valves for Digital Clay Actuators Array

The column refresh method scans through the column control valves one at a time to enable the control adapters in each column. Again, the enabling of control adapters in each column allows the working fluid to access all the actuators in that column. Figure 7.11 shows the column refresh step during the first iteration.

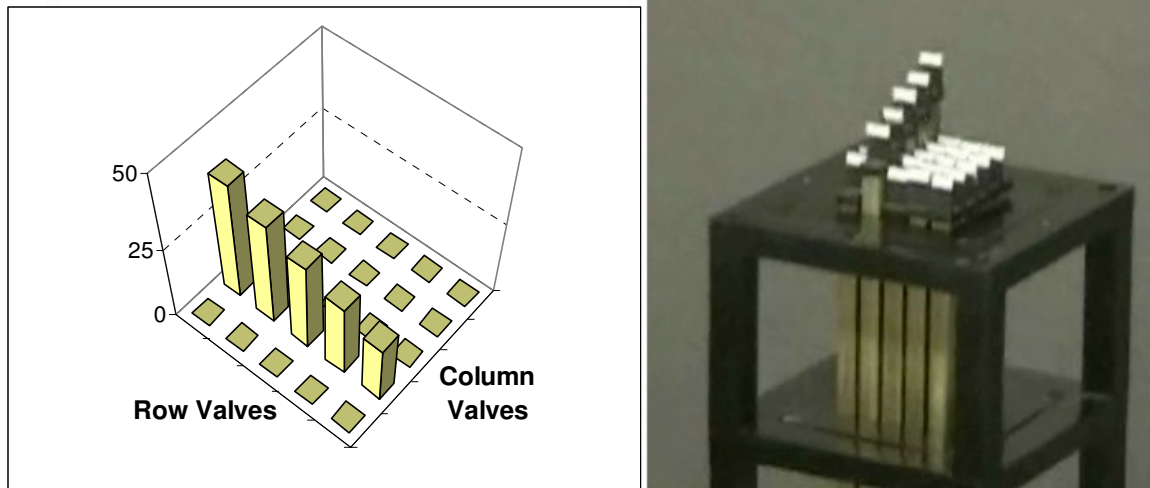


Figure 7.11 Surface Refresh Iteration 1. The first Column Control Valve is opened

As can be seen from the figure, during each column refresh step, only one column is enabled. All the other columns are disabled. During each column refresh step, an inner loop is running the row refresh steps. As this stage, the actuators in each row of the corresponding column will be monitored and displacement error recorded. The control law algorithm will calculate input duty ratio and save them in an array to be sent to the valve control circuit. At this time, the column refresh step will not proceed to the next column until all actuators in the column reach final steady state displacement. Figure 7.12 to Figure 7.15 show the row refresh step happens simultaneously during each column refresh step. After five steps, a complete surface is generated.

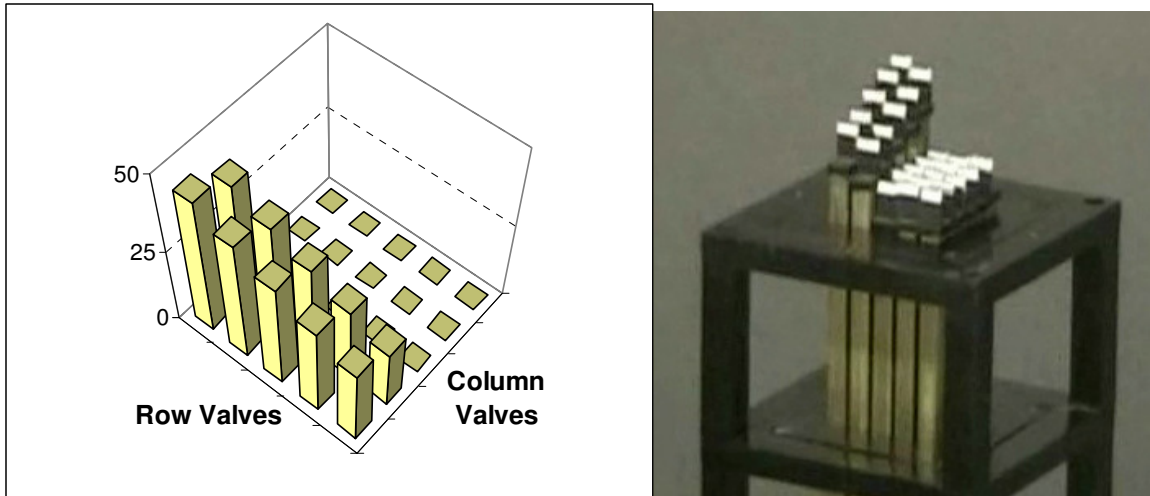


Figure 7.12 Surface Refresh Iteration 2. The second Column Control Valve is opened

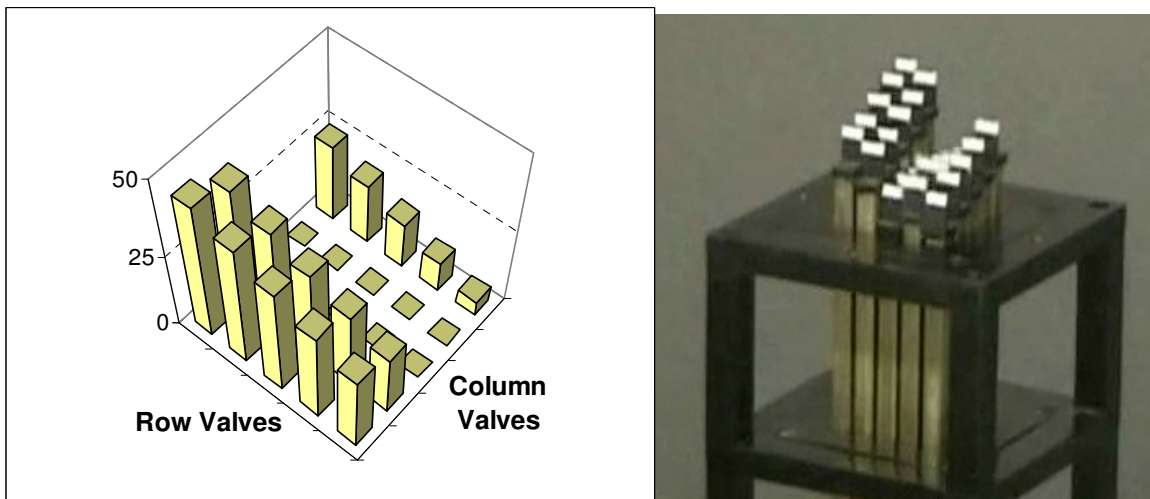


Figure 7.13 Surface Refresh Iteration 3. The third Column Control Valve is opened

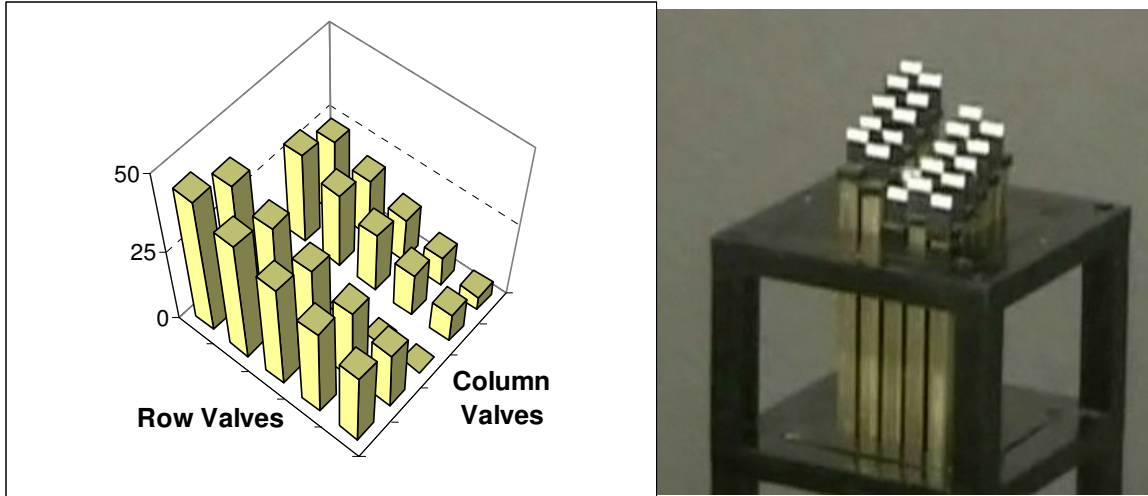


Figure 7.14 Surface Refresh Iteration 4. The fourth Column Control Valve is opened

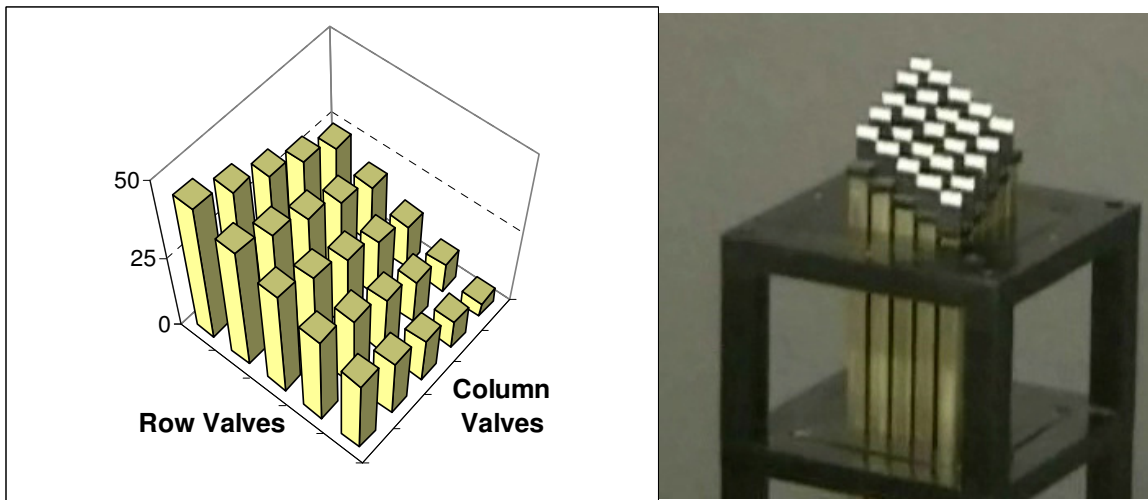


Figure 7.15 Last Surface Refresh Iteration. The fifth Column Control Valve is opened

The figures display a 5x5 array surface generation, but this algorithm is also applicable to larger array for future product. As it currently stands, the surface generation algorithm is done column by column and although it is the simplest method, does not

provide the best visual effect. Future work can be done on a more uniform and gradual surface refresh method for improved settling time and also visual effect.

7.3.2 Hot Area Processor Concept

As discussed from previous section, the surface refresh method for Digital Clay presents some limitations on applying single actuator haptic control to actuator array effectively without a specialized algorithm. From the single actuator method, when the user is pushing on the pin, effectively fluid in the cylinder is being forced out back to the supply line, or to the sink, depending on the haptic control method. However the surface refresh method does not monitor each actuator independently at every instance; only by column by column. Therefore if the user pushes on an actuator that is not being monitored, the fluid is being sealed in the cylinder at the particular instance; haptic effect is not activated. The user only feels a passive fluid restriction instead of active feedback. The time delay from when the surface refresh controller switches from its current active column to the column being interacted with by the user is very obvious and removes haptic realism. Furthermore, if the actuator is shut, the force observer breaks down as the system model does not take into account this behavior.

Therefore Zhu proposes a hot area processor concept, where the surface level controller will monitor any contact from the user on an area of the actuator array and allocate processing resources to the specific area so that haptic control can be applied. As the area to be contacted by the user finger is limited ($\sim 0.04\text{m}^2$), it is only necessary to enable haptic control for the small region of actuators, reducing computational resources. Figure 7.16 below shows the concept of hot area processor proposed by Zhu.

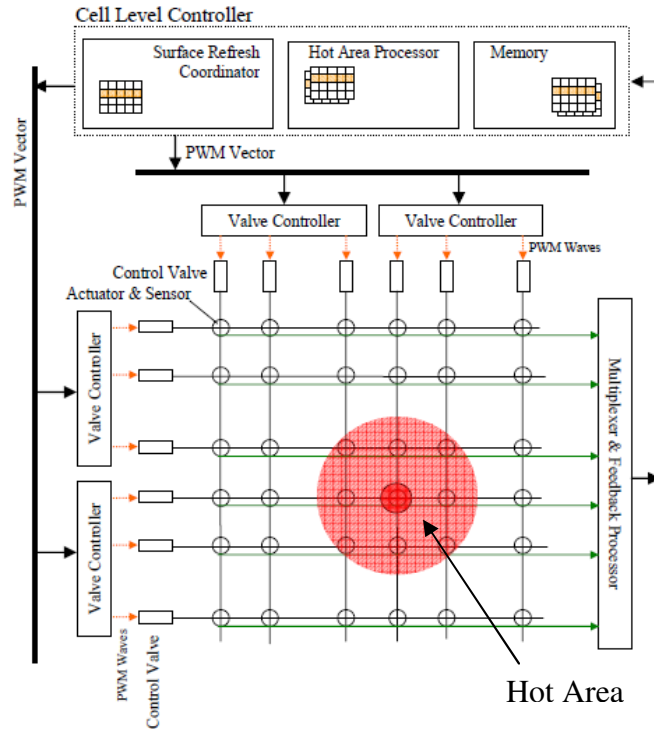


Figure 7.16 Hot Area Processing Concept for Digital Clay Surface

The concept is straightforward: after surface has reached steady state; monitor for contact on surface; define hot area and calculate centroid of the area; halts surface refresh algorithm; enable column valves and row valves for only the hot area and activate haptic control. The displacements of the actuators in the hot area will determine parameters for the haptic control or shaping state. After user removed contact from the surface, haptic control will be halted, and the surface refresh algorithm will restart. However as there are no pressure sensors present to monitor pressure changes in the actuators, an alternative contact detection method needs to be introduced.

As displacement is the only measurement that is available, there is little option but to take advantage of it. The algorithm will have the following flow: after surface has reached steady state, the displacement will have settled between a small error margin.

This margin will be declared as the percentage of uncertainty at steady state. As far as the current displacement control goes, the margin is $\pm 0.5\text{mm}$. Therefore a user contact will be defined as when the displacement error is larger than 0.5mm and having a negative velocity. As seen from displacement control response in Chapter 3, the displacement at steady state is stable; therefore this method of determining when a user is in contact with the actuator array can be used.

With hot area processing capability for Digital Clay available, haptic control mode developed for single actuator can be implemented on the actuator array with the only exception being all the actuators in the hot area are haptically controlled instead of one actuator. Figure 7.17 shows the hot area processor in action when a single column is opened. The red LED will light up to indicate the column(s) being enabled.

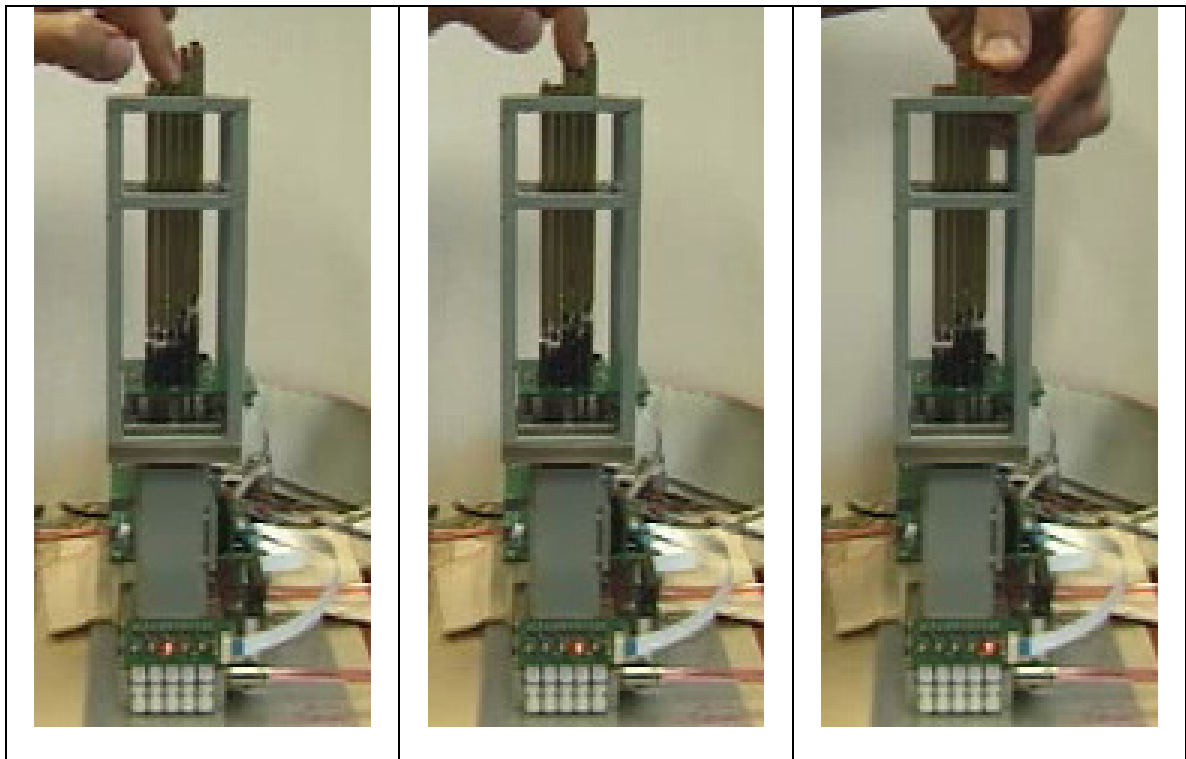


Figure 7.17 Hot Area Processor in Operation Opening Single Column

Figure 7.18 shows that the hot area processor functions correctly by enabling the corresponding columns when an area is being interacted with by the user.

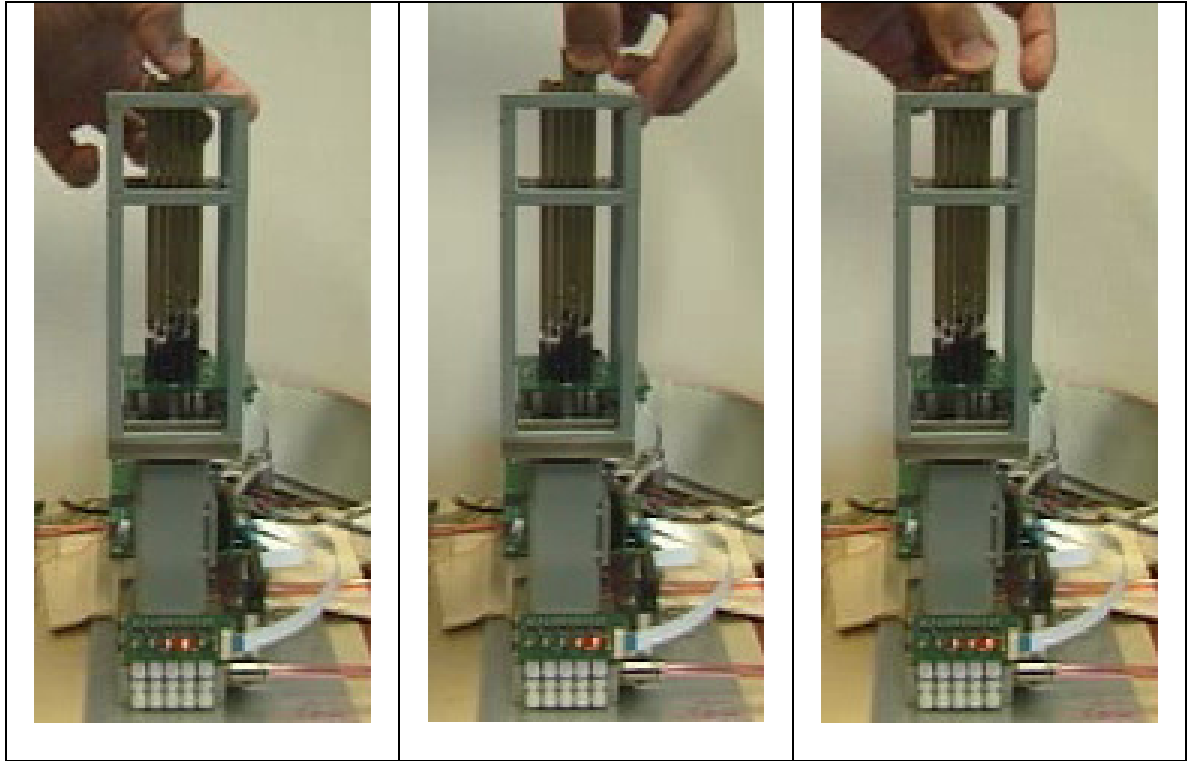


Figure 7.18 Hot Area Processor in Operation Opening Multiple Columns

7.4 Remarks and Discussion

In this chapter, the two most commonly used haptic control methods are successfully implemented on the current 5x5 Digital Clay prototype. The admittance haptic control utilized the displacement and velocity controller designed in Chapter 3 and the force observer designed in Chapter 5. A virtual stiffness with damping environment is simulated with the single actuator and it was observed that there exists a discontinuity in the motion of the actuator when the programming time delays for force estimation. It is suggested that a faster processor be used to increase sampling time to remove the

discontinuity. For the impedance haptic control, the pressure control technique designed in Chapter 6 is used to provide force feedback as a function of actuator displacement. An environment with virtual stiffness and the natural damping of the hydraulic actuator is simulated. It is noted that due to the closed-loop system limitation, marginal instability is observed when simulating high stiffness which requires high gains. For surface haptic realization, a hot area processing is needed to overcome the limitation posed by the matrix drive system. This method was first proposed by Zhu and now implemented to allow for the current haptic control methods.

CHAPTER 8 CONCLUSIONS AND RECOMMENDATIONS

8.1 Summary and Conclusions

The main goal of this research is to design and apply the two most commonly used haptic control methods to realize Digital Clay as a novel human machine interface device; the admittance control and the impedance control. The work is done on a 5x5 prototype currently available in the Intelligent Machine Dynamics Lab (IMDL) at the Georgia Institute of Technology. The current prototype was designed and built by Dr. Haihong Zhu in 2007. To be able to research the feasibility and apply both control methods to the current prototype, several tools had to be designed and the tools are: i) Displacement and velocity controller for single actuator, ii) Sensorless force estimation method, iii) Source pressure control technique and iv) Hot Area Processor for haptic surface.

The thesis starts with an introduction to the current Digital Clay prototype for readers who are not familiar with the hardware and concept. The main hardware of Digital Clay can be divided into the fluid matrix drive system and the actuators with embedded displacement sensors. To reduce the number of control valves in the system, a novel matrix drive system similar to LED array display is used. Instead of having N^2 control valves, the matrix drive only needs $2N$ valves to control N^2 actuators in the array. The actuator with embedded displacement sensor is also a novel technology developed by Zhu and further reduces size requirements without sacrificing sensing accuracy. The control scheme of Digital Clay is divided into top level, surface level and cell level control. The work in this thesis is mostly focused on cell level control; to control the

actuator independently, and surface level control for surface generation; which controls the actuators collectively. Control hardware of the Digital Clay consists of 12-bit analog-to-digital conversion and multiplexing function for the displacement sensors through a micro-controller unit dsPIC30F4013, a valve spike and hold circuit for each control valve and a main host computer on a Pentium 4 processor which is running on a real time operating system (RT Linux). A Measurement Computing PCI-DAS6402-16 data acquisition card on the host computer is used for digital and analog input/output (I/O) and analog-to-digital conversion functions. A micro-controller unit dsPIC30F6010 is used for interfacing and controlling the valves driver circuit with the host computer data acquisition card.

In Chapter 2, a comprehensive but not exhaustive review of past and current haptic devices and technologies is given. The importance of the sense of touch to human is sometimes overlooked, and while the majority of input output devices stimulates the human sight and hearing, the addition of haptic stimulus to human machine interface devices will add a new dimension of realism and perceiving information. While most haptic devices in use today are either point-based - to stimulate the human kinesthetic channel; or tactile - to stimulate the human touch channel, few attempt to combine the two stimuli. Digital Clay is a haptic device which attempts to provide both kinesthetic and tactile information and also visual information in the form of tangible surface. While attempting to emulate ordinary sculpture clay, Digital Clay has bidirectional information transfer; as an input or output device. Shape display has been achieved by the current prototype, but work needs to be done on the haptic display side of the device.

Chapter 3 presents the work on displacement and velocity control of the hydraulic actuator of Digital Clay. The work done here on the prototype is ultimately applicable to future versions of this device and completely scalable. To make Digital Clay responsive and effective as a haptic device, its motion control has to be simple and robust. The displacement controller is based on the feedback signal of the capacitively coupled resistive displacement sensor that is also the hydraulic actuator. From various experiments of sine wave and square wave displacement tracking, a proportional controller is the simplest and best method. The input effort is simply proportional to the displacement tracking error. For velocity control, accurate velocity information has to be obtained. Experiments show that finite differentiation of displacement amplifies noise and is phase shifted. The alpha-beta-gamma filter provides good velocity estimates but breaks down when acceleration of the actuator is not slowly-varying. Therefore, a linear estimator known as the low velocity and low acceleration estimator (LAE) was used. This estimator uses the integral of displacement signal in a feedback loop instead of the differential; which has the effect of attenuating measurement noise. In addition, the structure of the LAE is simpler than the alpha-beta-gamma filter. Finally, a PID controller is applied to control actuator velocity with good performance.

In Chapter 4, modeling of the single actuator system is presented. The work in this chapter is important not only for the design of a sensorless observer in Chapter 5, but also to understand the behavior, dynamics and limitations of a multi array and complicated system like the Digital Clay. As the system is hydraulic, the dynamics is nonlinear and needs to be linearized for the design of a linear observer. First, the frequency response of the system is investigated. From the Bode magnitude plot, the Digital Clay single

actuator plant has a bandwidth of 8Hz. Then, a 3rd order model is derived from differential equations commonly used in describing hydraulic behaviors. Common mathematical equations describing fluid flow through a variable orifice, fluid compressibility, and equilibrium of forces are combined to derive a more detailed model. The model was shown to estimate actual output with good accuracy. Parameter optimization was performed with MATLAB to reduce identification error.

In Chapter 5, the method of estimating user force without adding sensors to the system is investigated. First it was shown that actuator dynamic force is surprisingly linear compared to input flow and actuator static force will converge to system pressure in finite time. A linear observer with compensation of proportional and integral of estimation error known as the Proportional Integral Observer (PIO) was shown to estimate unknown system input with good accuracy. The user force is modeled as an unknown input and the observer was able to estimate dynamic forces exerted on the actuator with good accuracy. As the only information available is the displacement of the actuator, the fundamental limitation is static force estimation. A detailed procedure of selecting gains and conditions for error convergence is outlined. The second part of the chapter introduces the inverse plant dynamics disturbance observer, which yielded similar results to the PIO by choosing a stable and appropriate low pass Q filter.

In Chapter 6, a novel method to control system pressure was developed. The work in this chapter is motivated by the fact that impedance control mode is more widely applied; therefore a force/pressure control capability for Digital Clay is needed. Furthermore, the force estimator cannot be used to control actuator force when the displacement information is needed for the haptic controller. To simplify the method, only one pressure

sensor is used, thus only the system pressure can be controlled. The feedback control depends on the simultaneous control of inlet flow and outlet flow from the system. The use of inlet and outlet valves currently available for the prototype generates pressure fluctuations and is undesirable for haptic control; therefore a variable orifice consisting of two pulse width modulated micro-miniature valves is designed. The micro-miniature valves have higher bandwidth than the original valves and do not generate pressure fluctuations. Both inlet and outlet flow are controlled in this manner. From experiments, it is shown that a PI controller can provide adequate pressure control with zero steady state error and rise time of about 0.25sec. It is also noted that the bandwidth of the feedback control system is around 5Hz which is due to physical and controller limitation.

Finally in Chapter 7, all the tools are combined and two haptic control modes are implemented. For the admittance haptic mode, the actuator motion is controlled as the actuator force is estimated. The impedance haptic mode controls actuator pressure depending on actuator motion. Both haptic modes are feasible for implementation on Digital Clay as well as actuator shaping mode. For surface haptics, a hot area processor proposed by Zhu is implemented to enable haptic control for array of actuators in contact with the user finger. This method overcomes the limitation posed by the matrix drive system while at reduced computational cost. As such, the goal of this research has been met by successfully showing that both haptic control methods can be applied to Digital Clay with no additional hardware cost, with the exception of adding a pressure sensor and four micro-miniature valves to enable pressure control. The addition of the sensor and valves are a one-time modification, in that if the system is scalable, the same concept will apply.

8.2 Contributions

The major contributions of this research can be broken down into the following: A reliable velocity estimator to obtain actuator velocity from displacement measurement was implemented. Subsequently, a simple PID controller that has good tracking performance was designed and implemented on the digital controller. This work can be applied to future versions of Digital Clay. A first order, a second order and a detailed linearized model of the single actuator system were derived. These results presented on Digital Clay not been performed before and the development of the model is a first step. The dynamics of the system is now better understood and limitations on current prototype will provide invaluable information to improve future versions. A novel sensorless force estimation method for single actuator of Digital Clay was designed. Although this estimator has some limitations, it is able to estimate dynamic force exerted on the actuator with good accuracy. Very little research has been done on sensorless force estimation of hydraulic actuators because of the highly nonlinear dynamics. A novel method of controlling pressure in hydraulic line via flow control was conceived. This method can be applied to any hydraulic systems and not only to Digital Clay. For this application, the ability to control system pressure enables implementation of impedance haptic control. Finally, it was successfully shown that both admittance and impedance haptic control methods can be used by Digital Clay as an effective next-generation human machine interface. The limitation and possible improvements for both control methods were outlined.

8.3 Recommendations for Future Research

Though haptic control methods have been implemented on the current working prototype, there are a number of improvements and future works on both the software and hardware side of things before Digital Clay can be propelled as a true haptic device for human machine interface. The improvements on the works presented in the thesis are:

The PID gains for the velocity controller have to be specifically tuned for each actuators of Digital Clay as the parameters may vary by a great amount. For future research, an adaptive controller or a robust controller can be implemented, which will require higher computational costs. The linearized model of single actuator system is able to estimate actual output with good accuracy however as there is no full-state feedback it is difficult to fully reconstruct the state of the nonlinear systems, namely cylinder pressures. When the valve flow equations are linearized, the estimated cylinder pressures are not very useful for unknown input estimation. Hence the proportional integral observer (PIO) designed in Chapter 5 was limited to estimation of linear component of the unknown input, the dynamic forces. If the internal states are known, the estimation would improve greatly. Therefore future work needs to be done in deriving a nonlinear observer such as the Lyapunov based nonlinear observer for estimation of pneumatic actuator pressures by Gulati and Barth [44]. For the pressure control method presented in Chapter 6, the limitation was the low closed-loop system bandwidth. The PI controller designed is not able to increase stability margin of the pressure control, therefore limiting the system response to 0.25sec settling time. Therefore, a controller for controlling system pressure such as the Lyapunov based controller commonly used in force control of hydraulic system is needed. For both of the haptic control methods, future work could

be done in simulating more complex virtual environment such as plastic behavior, creep or buckling when certain yield force is exceeded. The hot area processor seems to be the most feasible solution for surface haptics at this moment but research could be done on an alternative method of driving the actuator arrays which will lead to some future work to be done on Digital Clay in general:

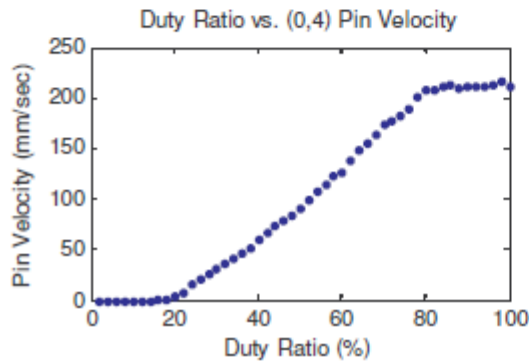
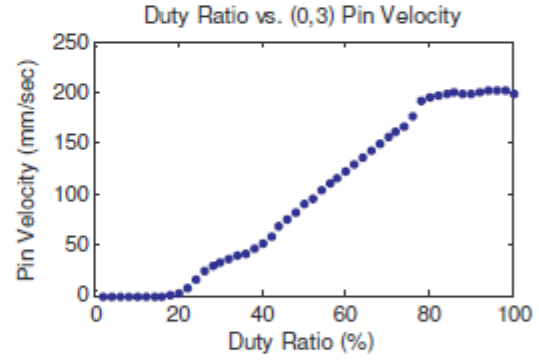
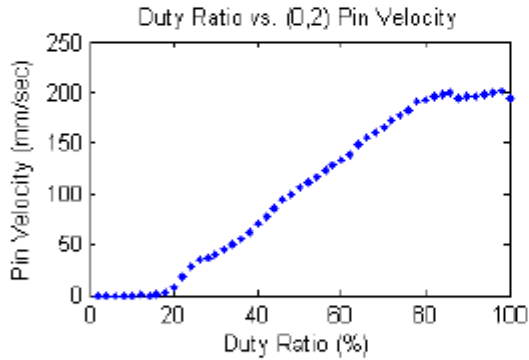
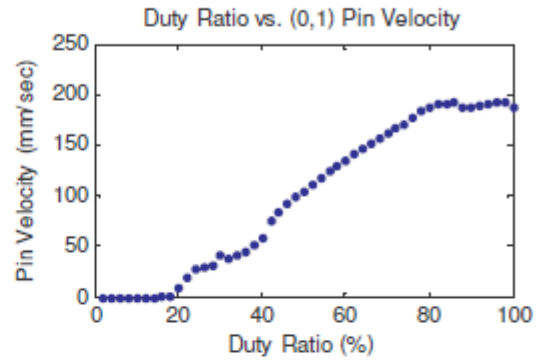
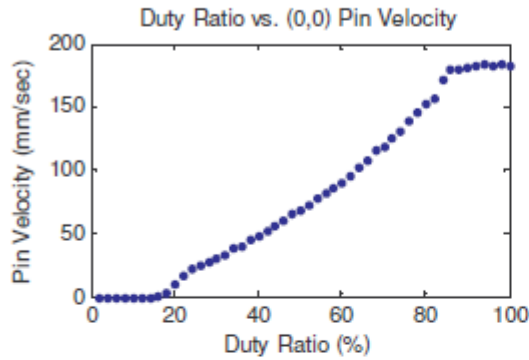
The sensor embedded in the hydraulic actuator architecture has been improved by Dr. Haihong Zhu and for future versions of Digital Clay, wireless sensor or sensor with hidden wiring will add to the durability of the device if used in harsher environments. With the advent of micro-electromechanical system (MEMs) technology, it is possible that the actuators in the array have individual controllable hydraulic valves to eliminate the matrix drive system. This will reduce the complexity of surface refresh method and increase haptic performance. For operation in a remote environment, Digital Clay needs to have a regenerative power supply, which means a fluid pump needs to be included to circulate the working fluid within the system. Currently, a new project is beginning with Digital Clay taking the role of a haptic interface for the operator of a remotely controlled manipulator. It will also function at the remote site as a sensor of the shape and compliance of the remote environment. Many new additional challenges will evolve from this application.

Finally, the resolution of the actuator array needs to be increased without increasing overall size; which means reducing the size of individual actuators and reduce the spacing in between actuators for improved haptic and visual effect.

APPENDIX A1

Actuator Velocity vs. Input Duty Ratio for Column 1

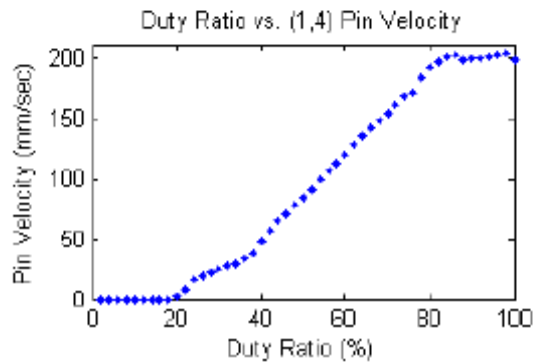
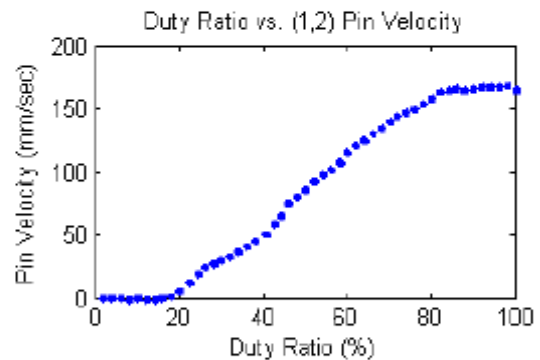
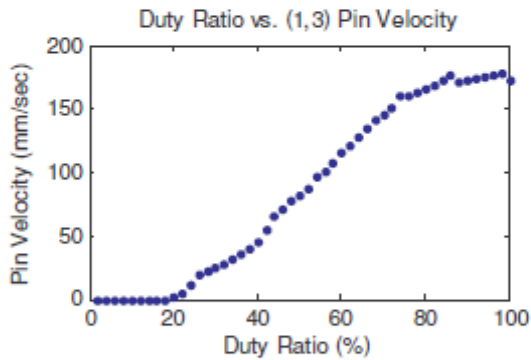
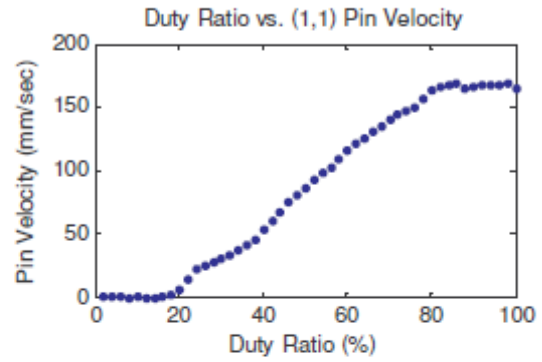
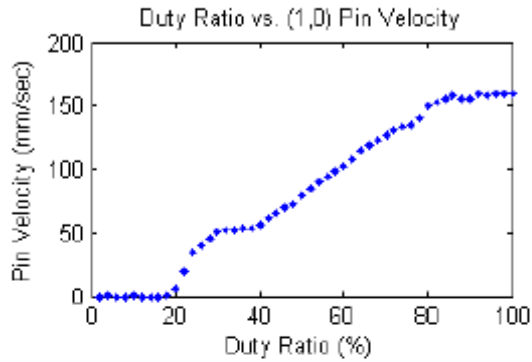
| | | | | |
|----|----|----|----|----|
| 21 | 22 | 23 | 24 | 25 |
| 16 | 17 | 18 | 19 | 20 |
| 11 | 12 | 13 | 14 | 15 |
| 6 | 7 | 8 | 9 | 10 |
| 1 | 2 | 3 | 4 | 5 |



APPENDIX A2

Actuator Velocity vs. Input Duty Ratio for Column 2

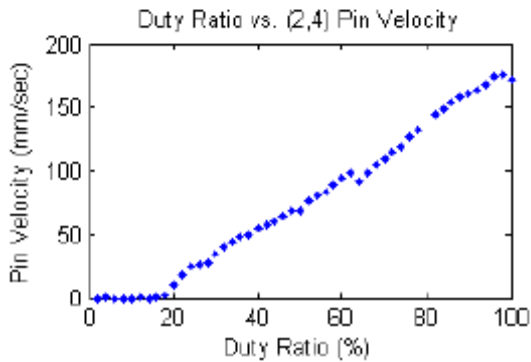
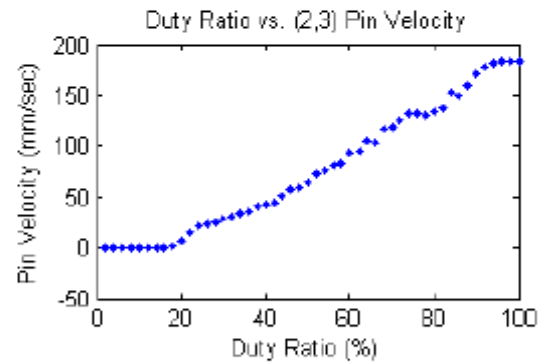
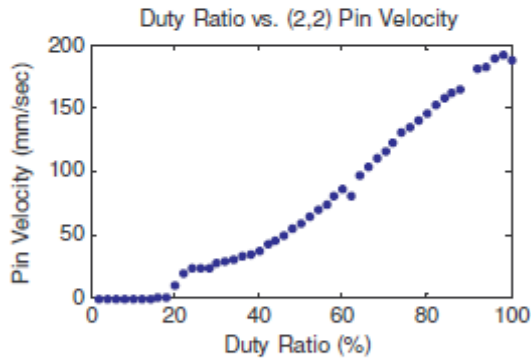
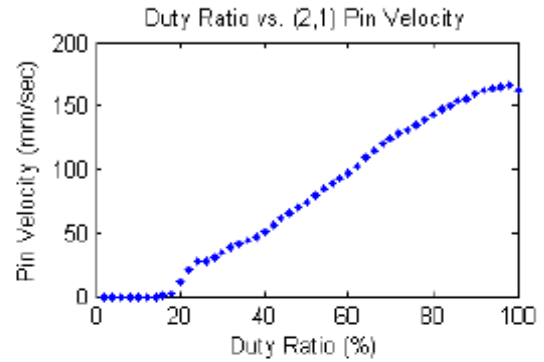
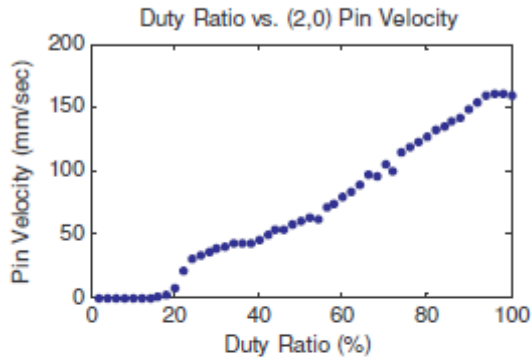
| | | | | |
|----|----|----|----|----|
| 21 | 22 | 23 | 24 | 25 |
| 16 | 17 | 18 | 19 | 20 |
| 11 | 12 | 13 | 14 | 15 |
| 6 | 7 | 8 | 9 | 10 |
| 1 | 2 | 3 | 4 | 5 |



APPENDIX A3

Actuator Velocity vs. Input Duty Ratio for Column 3

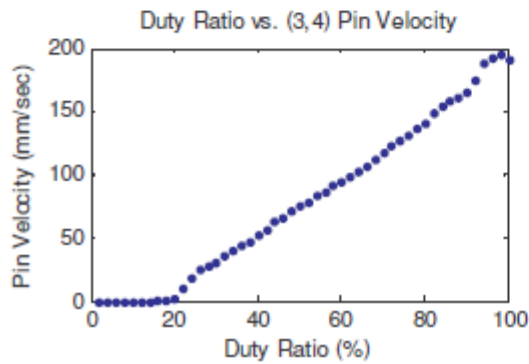
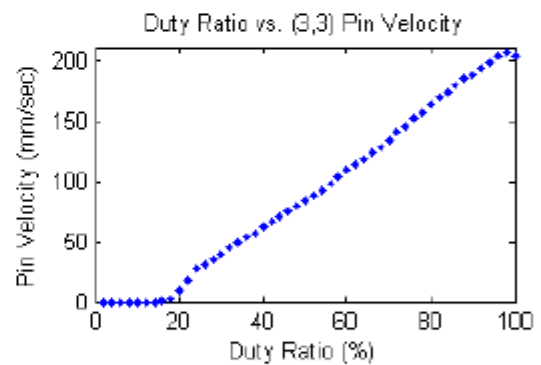
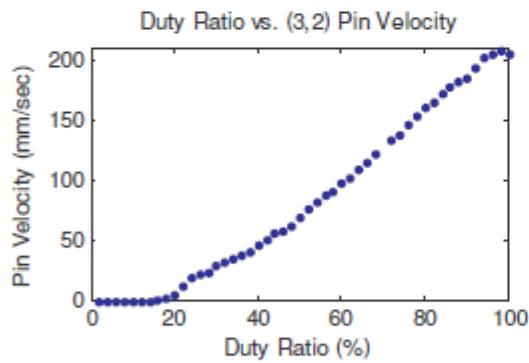
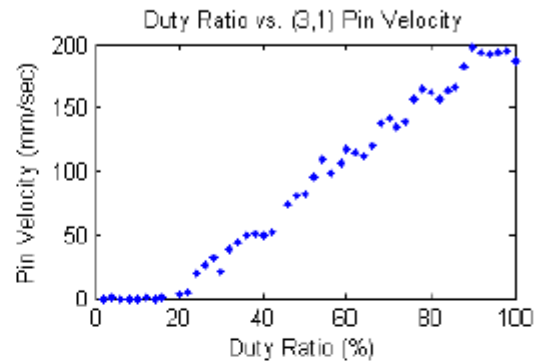
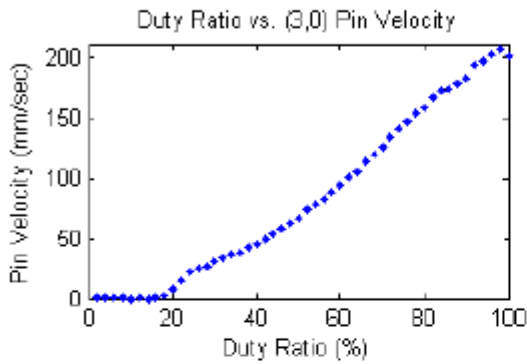
| | | | | |
|----|----|----|----|----|
| 21 | 22 | 23 | 24 | 25 |
| 16 | 17 | 18 | 19 | 20 |
| 11 | 12 | 13 | 14 | 15 |
| 6 | 7 | 8 | 9 | 10 |
| 1 | 2 | 3 | 4 | 5 |



APPENDIX A4

Actuator Velocity vs. Input Duty Ratio for Column 4

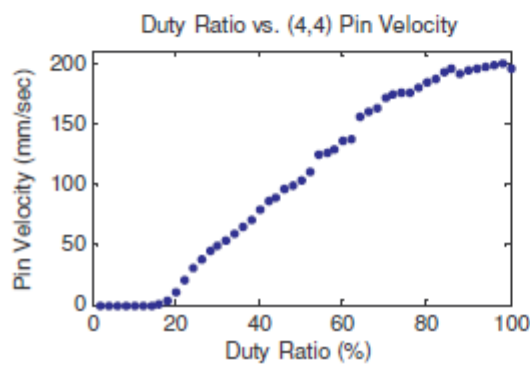
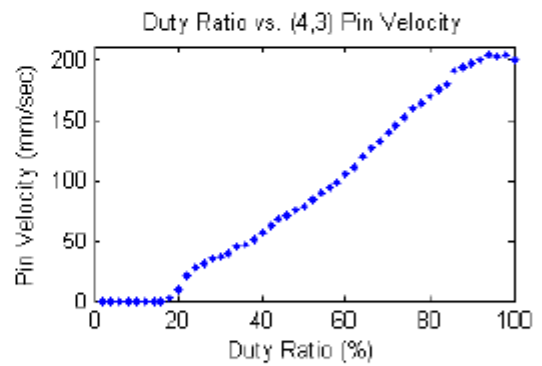
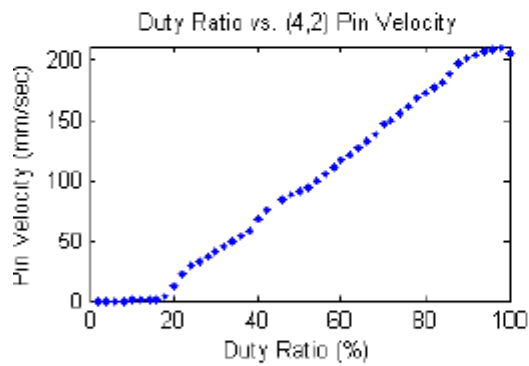
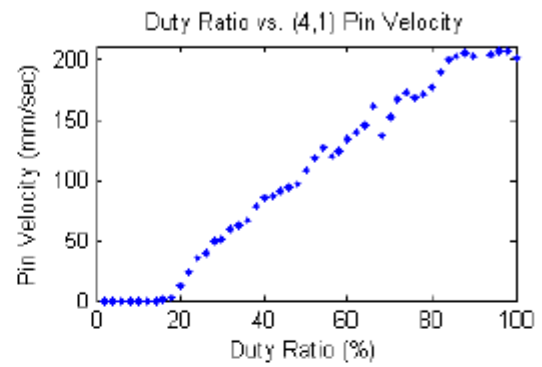
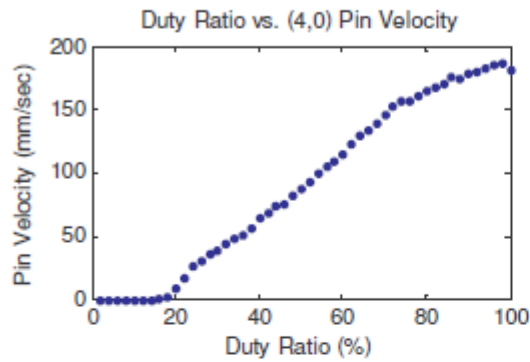
| | | | | |
|----|----|----|----|----|
| 21 | 22 | 23 | 24 | 25 |
| 16 | 17 | 18 | 19 | 20 |
| 11 | 12 | 13 | 14 | 15 |
| 6 | 7 | 8 | 9 | 10 |
| 1 | 2 | 3 | 4 | 5 |



APPENDIX A5

Actuator Velocity vs. Input Duty Ratio for Column 5

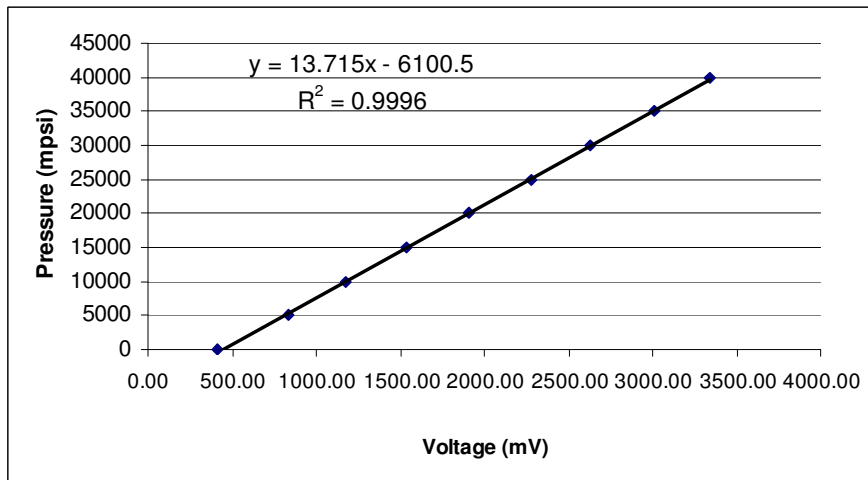
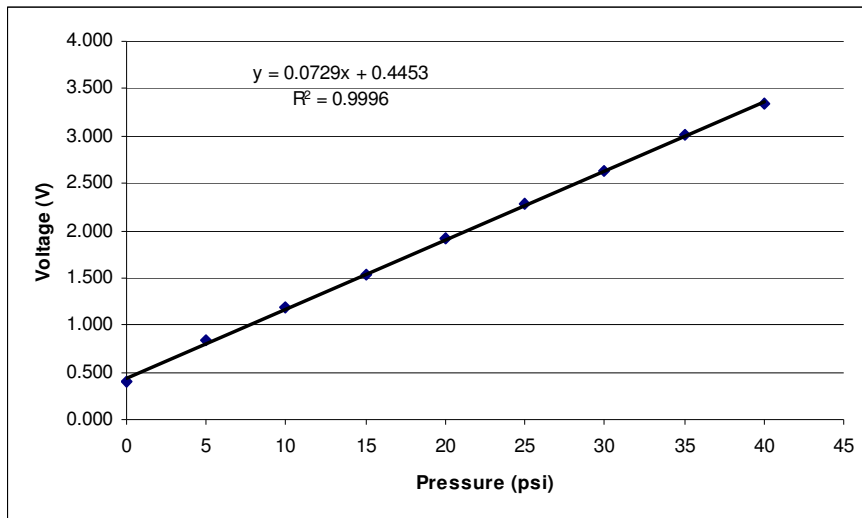
| | | | | |
|----|----|----|----|----|
| 21 | 22 | 23 | 24 | 25 |
| 16 | 17 | 18 | 19 | 20 |
| 11 | 12 | 13 | 14 | 15 |
| 6 | 7 | 8 | 9 | 10 |
| 1 | 2 | 3 | 4 | 5 |



APPENDIX B Honeywell ASCX100DN Pressure Sensor Calibration



Average Offset - 0.41 V

| Pressure (psi) | Voltage (V) | | | | | Average Voltage (V) |
|----------------|-------------|-------|-------|-------|-------|---------------------|
| | 1 | 2 | 3 | 4 | 5 | |
| 0 | 0.410 | 0.409 | 0.410 | 0.410 | 0.409 | 0.410 |
| 5 | 0.836 | 0.834 | 0.832 | 0.844 | 0.848 | 0.839 |
| 10 | 1.181 | 1.180 | 1.179 | 1.178 | 1.180 | 1.180 |
| 15 | 1.535 | 1.534 | 1.535 | 1.535 | 1.533 | 1.535 |
| 20 | 1.912 | 1.911 | 1.912 | 1.910 | 1.911 | 1.911 |
| 25 | 2.280 | 2.280 | 2.279 | 2.278 | 2.280 | 2.279 |
| 30 | 2.628 | 2.627 | 2.628 | 2.626 | 2.626 | 2.627 |
| 35 | 3.008 | 3.007 | 3.008 | 3.008 | 3.007 | 3.008 |
| 40 | 3.340 | 3.340 | 3.340 | 3.339 | 3.339 | 3.340 |



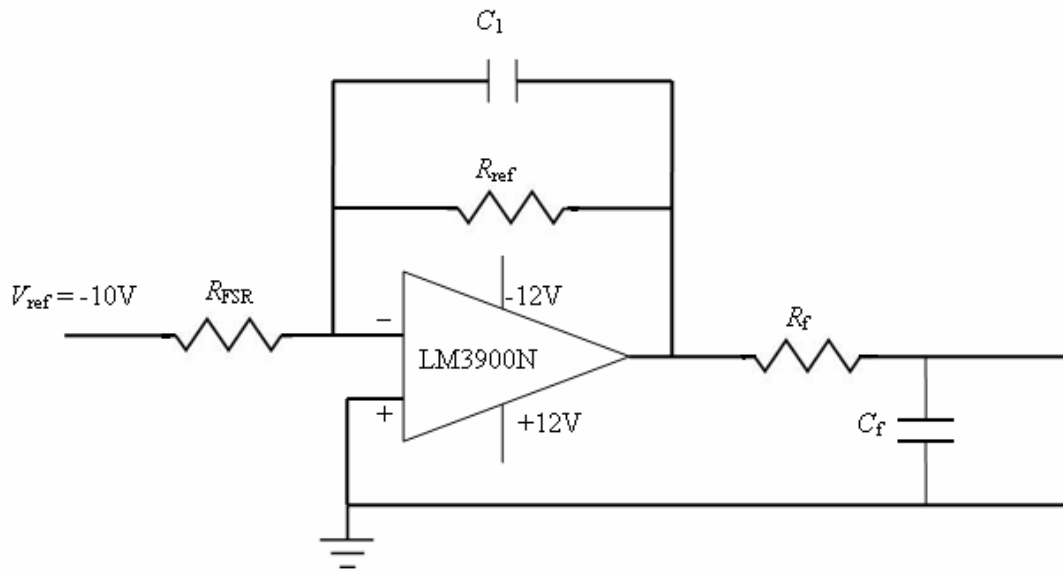
APPENDIX C

PCB Electronics 209C12 Force Sensor Data Sheet

| Model Number 209C12 | FORCE SENSOR, ICP® | | Revision E ECN #: 25168 | | | | | | | | | | |
|--|---|---|---|---------------|--------------|------------------|------------------|------------------|------------------|------|---|--|--|
| <p>Performance</p> <p>Sensitivity (±15%) Measurement Range (Compression) Measurement Range (Tension) Maximum Static Force (Compression) Maximum Static Force (Tension) Broadband Resolution (1 to 10000 Hz) Low Frequency Response (-5%) Upper Frequency Limit</p> <p>Environmental</p> <p>Temperature Range Temperature Coefficient of Sensitivity</p> <p>Electrical</p> <p>Discharge Time Constant (at room temp) Excitation Voltage Constant Current Excitation Output Impedance Output Bias Voltage Spectral Noise (1 Hz) Spectral Noise (10 Hz) Spectral Noise (100 Hz) Spectral Noise (1000 Hz) Output Polarity (Compression)</p> <p>Physical</p> <p>Stiffness Size (Hex x Height) Weight Housing Material Sealing Electrical Connector Electrical Connection Position Mounting Thread Mounting Torque (Recommended)</p> | <p>ENGLISH</p> <p>2200 mV/lb 2.2 lb 1.0 lb 11.0 lb 1.0 lb 0.00002 lb-rms 0.05 Hz 30 kHz</p> <p>-65 to +250 °F -50.05 %/°F</p> <p>≥10 sec 18 to 30 VDC 2 to 20 mA ≤100 ohm 8 to 12 VDC 0.0000123 lb-√Hz 0.000009 lb-√Hz 0.000004 lb-√Hz 0.000001 lb-√Hz Positive</p> <p>2 lb/in 0.372 in x 0.83 in 0.29 oz Stainless Steel Hermetic 10-32 Coaxial Jack Side 10-32 Female 15 to 20</p> | <p>SI</p> <p>49460.4 mV/kN 0.00879 kN 0.00445 kN 0.0489 kN 0.00445 kN 0.00009 N-rms 0.05 Hz 30 kHz</p> <p>-64 to +121 °C -50.09 %/°C</p> <p>≥10 sec 18 to 30 VDC 2 to 20 mA ≤100 ohm 8 to 12 VDC 0.0000548 N-√Hz 0.0000042 N-√Hz 0.0000017 N-√Hz 0.0000003 N-√Hz Positive</p> <p>0.35 kN/mm 9.53 mm x 21.08 mm 8.2 gm Stainless Steel Hermetic 10-32 Coaxial Jack Side No Metric Equivalent 169 to 226</p> | <p>Optional Versions (Optional versions have identical specifications and accessories as listed for standard model except where noted below. More than one option may be used.)</p> <p>M - Metric Mount S - Supplied Accessory: Model M081A05 Mounting Stud replaces Model 081A05 N - Negative Output Polarity W - Water Resistant Cable Electrical Connector Electrical Connection Position</p> <p>Notes</p> <p>[1] Typical. [2] Calculated from discharge time constant. [3] Estimated using rigid body dynamics calculations. [4] See PCB Declaration of Conformance P3023 for details.</p> <p>Supplied Accessories</p> <p>081A05 Mounting stud, 10-32 to 10-32 x 0.27" long, BeCu (#1800), no shoulder (1) 084438 Thermal boot (for Series 209) (1)</p> | | | | | | | | | | |
|  | | | | | | | | | | | | | |
| <p>All specifications are at room temperature unless otherwise specified. In the interest of constant product improvement, we reserve the right to change specifications without notice. ICP® is a registered trademark of PCB group, Inc.</p> | | | | | | | | | | | | | |
| <table border="1" style="width: 100%; border-collapse: collapse;"> <tr> <td>Entered: BLS</td> <td>Engineer: DMB</td> <td>Sales: RVM</td> <td>Approved: BLS</td> <td>Spec Number:</td> </tr> <tr> <td>Date: 10/20/2006</td> <td>Date: 10/20/2006</td> <td>Date: 10/23/2006</td> <td>Date: 10/24/2006</td> <td>6863</td> </tr> </table> | Entered: BLS | Engineer: DMB | Sales: RVM | Approved: BLS | Spec Number: | Date: 10/20/2006 | Date: 10/20/2006 | Date: 10/23/2006 | Date: 10/24/2006 | 6863 |  <p>PCB PIEZOTRONICS™ FORCE / TORQUE DIVISION</p> <p>3425 Walden Avenue Depew, NY 14043 UNITED STATES Phone: 888-684-0004 Fax: 716-684-8877 E-mail: force@pcb.com Web site: www.pcb.com</p> | | |
| Entered: BLS | Engineer: DMB | Sales: RVM | Approved: BLS | Spec Number: | | | | | | | | | |
| Date: 10/20/2006 | Date: 10/20/2006 | Date: 10/23/2006 | Date: 10/24/2006 | 6863 | | | | | | | | | |

APPENDIX D

TEKSCAN FlexiForce A201 Force Sensor Circuit



$$R_{ref} = 100k\Omega$$

$$C_1 = 47pF$$

$$R_f = 5600\Omega$$

$$C_f = 680nF$$

Passive Low Pass Filter Cutoff Frequency:

$$f_c = \frac{1}{2\pi RC} \text{ Hz} = \frac{1}{2\pi \cdot 5600 \cdot 680 \cdot 10^{-9}} \approx 41.8 \text{ Hz}$$

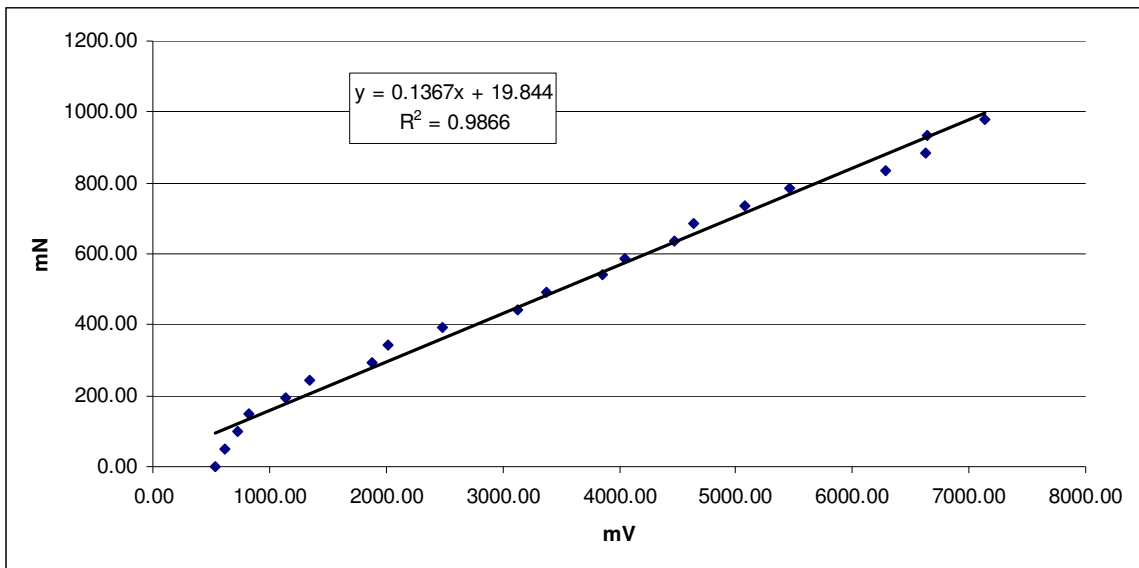
Sensor resistance to output voltage:

$$V_{sensor} = -\frac{R_{ref}}{R_{FSR}} \cdot V_{ref}$$

APPENDIX E

TEKSCAN FlexiForce A201 Force Sensor Calibration

| Weight (g) | Force (N) | Force (mN) | Voltage (V) | | | | | Average (mV) |
|------------|-----------|------------|-------------|------|------|------|------|--------------|
| | | | 1 | 2 | 3 | 4 | 5 | |
| 0 | 0.0 | 0.00 | 0.54 | 0.54 | 0.54 | 0.54 | 0.54 | 540.00 |
| 5 | 0.0 | 49.05 | 0.61 | 0.62 | 0.61 | 0.61 | 0.61 | 612.00 |
| 10 | 0.1 | 98.10 | 0.71 | 0.71 | 0.72 | 0.75 | 0.72 | 722.00 |
| 15 | 0.1 | 147.15 | 0.82 | 0.82 | 0.81 | 0.82 | 0.82 | 818.00 |
| 20 | 0.2 | 196.20 | 1.14 | 1.14 | 1.14 | 1.14 | 1.15 | 1142.00 |
| 25 | 0.2 | 245.25 | 1.33 | 1.35 | 1.34 | 1.35 | 1.35 | 1344.00 |
| 30 | 0.3 | 294.30 | 1.86 | 1.86 | 1.88 | 1.9 | 1.89 | 1878.00 |
| 35 | 0.3 | 343.35 | 2.03 | 2.02 | 2.01 | 2.01 | 2 | 2014.00 |
| 40 | 0.4 | 392.40 | 2.45 | 2.55 | 2.48 | 2.51 | 2.42 | 2482.00 |
| 45 | 0.4 | 441.45 | 3.1 | 3.12 | 3.13 | 3.14 | 3.14 | 3126.00 |
| 50 | 0.5 | 490.50 | 3.32 | 3.35 | 3.37 | 3.41 | 3.44 | 3378.00 |
| 55 | 0.5 | 539.55 | 3.91 | 3.86 | 3.84 | 3.85 | 3.84 | 3860.00 |
| 60 | 0.6 | 588.60 | 4.16 | 4.02 | 4.03 | 3.98 | 4.06 | 4050.00 |
| 65 | 0.6 | 637.65 | 4.54 | 4.55 | 4.52 | 4.56 | 4.23 | 4480.00 |
| 70 | 0.7 | 686.70 | 4.66 | 4.65 | 4.63 | 4.62 | 4.61 | 4634.00 |
| 75 | 0.7 | 735.75 | 5.09 | 5.04 | 5.1 | 5.09 | 5.08 | 5080.00 |
| 80 | 0.8 | 784.80 | 5.51 | 5.46 | 5.44 | 5.45 | 5.42 | 5456.00 |
| 85 | 0.8 | 833.85 | 6.28 | 6.32 | 6.24 | 6.26 | 6.35 | 6290.00 |
| 90 | 0.9 | 882.90 | 6.62 | 6.66 | 6.63 | 6.62 | 6.58 | 6622.00 |
| 95 | 0.9 | 931.95 | 6.67 | 6.64 | 6.66 | 6.65 | 6.62 | 6648.00 |
| 100 | 1.0 | 981.00 | 7.12 | 7.11 | 7.14 | 7.17 | 7.13 | 7134.00 |



REFERENCES

- [1] Zhu, H., "Practical Structural Design and Control for Digital Clay," Ph.D. Thesis, Georgia Institute of Technology, Atlanta, GA., 2005.
- [2] Hayward, V., Astley, O. R., Hernandez, M., Grant, D., Robles-De-La-Torre, G., "Haptic interfaces and Devices", *Sensor Review*, vol. 24(1), pp. 16-29, 2004.
- [3] Zhu, H., Book, W.J., "Construction and Control of Massive Hydraulic Miniature-Actuator-Sensor Array", 2006 IEEE International Conference on Control Applications, 2006 IEEE International Symposium on Intelligent Control, p. 6, 2006.
- [4] Zhu, H., and Book, W. J., "Practical Structure Design and Control for Digital Clay", 2004 ASME International Mechanical Engineering Congress and Exhibition, p. 1051, 2004.
- [5] Zhu, H., Book, W. J., "Digital Clay: Concept and Prototype", *Proceedings of 2006 Conference on International Robotics and Automation*, pp. 4449-4451, 2006.
- [6] Zhu, H., Book, W. J., "Embedding and Multiplexing Large Scale Sensor Arrays for Digital Clay", *Proceedings of ASME-IMECE ASME International Mechanical Engineering Congress and Exposition, Orlando FL, November 5-11, 2005*.
- [7] Shen, X, Goldfarb, M., "On the Enhanced Passivity of Pneumatically Actuated Impedance-type Haptic Interfaces", *IEEE Transactions on Robotics*, vol. 22 (3), pp. 470-480, 2006.
- [8] Wen, K., Neculescu, D., Sasiadek, J., "Haptic Force Control Based on Impedance/Admittance Control Aided by Visual Feedback", *Multimedia Tools and Applications*, vol. 37 (1), pp. 39-52, March 2008.
- [9] Tan, H. Z., Eberman, B., Srinivasan, M., Cheng, A., "Human Factors for the Design of Force-Reflecting Haptic Interfaces", *American Society of Mechanical Engineers, Dynamic Systems and Control Division*, vol. 55(1), pp. 353-359, 1994.
- [10] Robles-De-La-Torre, G., "The Importance of the Sense of Touch in Virtual and Real Environments", *International Society for Haptics*, 2006.

- [11] Isdale, J. "A Taxonomy of Virtual Reality", <http://vr.isdale.com/WhatIsVR/noframes/WhatIsVR4.1-A.html> (Accessed October 27, 2009).
- [12] Massie, T. M., Salisbury, J. K., "The Phantom Haptic Interface: A Device for Probing Virtual Objects", Proc. of ASME Haptic Interfaces for Virtual Environment and Teleoperator Systems, Vol. 1, pp. 295-301, 1994.
- [13] Hasser, D., "Tactile Feedback with Adaptive Controller for a Force-Reflecting Haptic Display", Proceedings of Southern Biomedical Engineering Conference pp. 530-533, 1996.
- [14] Liu, J., Song, A., and Zhang, H., "Research on Stiffness Display Perception of Virtual Soft Object", Proceedings of the 2007 International Conference on Information Acquisition, ICIA, pp. 558-562, 2007.
- [15] Casiez, P., "Elastic Force Feedback with a New Multi-Finger Haptic Device-Digihaptic", Proceedings of Eurohaptics, pp. 121—134, 2003.
- [16] Yoshikawa, T., Nagura, A., "A Touch/Force Display System for Haptic Interface", Presence, vol. 10 (2), pp. 225-35, April 2001.
- [17] Moy, G., Singh, U., Tan, E., Fearing, R.S., "Human Psychophysics for Teletaction System Design," Haptics-e., vol. 1 (3), February, 18, 2000.
- [18] Bliss, J. C., "A Relatively High-Resolution Reading Aid for the Blind", IEEE Trans. on Man-Machine System, vol. 10, pp. 1-9, 1969.
- [19] Cohn, M. B., Lam, M., Fearing, R.S., "Tactile Feedback for Teleoperation", SPIE Telemanip. Tech., vol. 1833, pp. 240-254, 1993.
- [20] Kyung, K., Ahn, M., Kwon, D., Srinivasan, M., "A Compact Broadband Tactile Display and its Effectiveness in the Display of Tactile Form", Proceedings of Eurohaptics Conference and Symposium on Haptic Interfaces for Virtual Environment and Teleoperator Systems, pp. 600-601, 2005.
- [21] Howe, R. D., Peine, W. J., Kontarinis, D. A., Son, J. S., "Remote Palpation Technology", IEEE Eng. in Med. and Bio. Mag., pp. 318-323, 1995.

- [22] Killebrew, J. H., Bensaïa, S. J., Dammann, J. F., Denchev, P., Hsiao, S. S., Craig, J. C., Johnson, K. O., "A Dense Array Stimulator to Generate Arbitrary Spatio-Temporal Tactile Stimuli", *Journal of Neuroscience Methods*, vol. 161, pp. 62-74, 2007.
- [23] Qi, W., Hayward, V., "Compact, Portable, Modular, High-Performance, Distributed Tactile Transducer Device Based on Lateral Skin Deformation", *Proceedings of 14th Symposium on Haptics Interfaces for Virtual Environment and Teleoperator Systems*, pp. 67-72, 2006.
- [24] Cohn, M. B., Lam, M., Fearing, R. S., "Tactile Feedback for Teleoperation", *SPIE Telemanipulator Tech.*, vol. 1833, pp. 240-254, Boston, MA, November 15-16, 1992.
- [25] Caldwell, D. G., Tsagarakis, N., Giesler, C., "An Integrated Tactile/Shear Feedback Array for Stimulation of Finger Mechanoreceptor", *IEEE Int. Conf. Rob. And Auto.*, vol. 1, pp. 287-292, Detroit, MI, May 1999.
- [26] Wagner, C. R., Lederman, S. J., Howe, R. D., "A Tactile Shape Display Using RC Servomotors", *Proceedings 10th Symposium on Haptic Interfaces for Virtual Environment and Teleoperator Systems HAPTICS*, pp. 354-5, 2002.
- [27] Sarakoglou, I., Tsagarakis, N., Caldwell, D. G., "A Portable Fingertip Tactile Feedback Array - Transmission System Reliability and Modeling", *Proceedings of First Joint Eurohaptics Conference and Symposium on Haptic Interfaces for Virtual Environment and Teleoperator Systems*, pp. 547-548, 2005.
- [28] Fischer, H., Neisius, B., Trapp, R., "Tactile Feedback for Endoscopic Surgery", *Interactive Technology and New Paradigm for Healthcare*, pp. 114-117, IOS Press 1995.
- [29] Ikei, Y., Shiratori, M., "TextureExplorer: A Tactile and Force Display for Virtual Textures", *Proceedings 10th Symposium on Haptic Interfaces for Virtual Environment and Teleoperator Systems*, pp. 327-334, 2002.
- [30] Iwata, H., Yano, H., Kawamura, R., "Array Force Display for Hardness Distribution", *Proceedings 10th Symposium on Haptic Interfaces for Virtual Environment and Teleoperator Systems*, pp. 165-171, 2002.
- [31] Nakatani, K., Sekiguchi, K., "3D Form Display with Shape Memory Alloy", *Proc. of International Conference on Artificial Reality and Telexistence*, vol. 8, pp. 247-248, 2003.

- [32] Garth, J., Fluidic Driven Digital Clay, Master's Thesis, Georgia Institute of Technology, Atlanta, GA., 2006.
- [33] Blair, W.D., Gray, J.E., Boyd, M.D., 1991, "Design Analysis for the Two-Stage Alpha, Beta, Gamma Estimator". IEEE Proceedings of Southeastcon '91, New York, NY, 2, pp.1050-1054, 1991.
- [34] Lee, S. H., Song, J. B., "Acceleration Estimator for Low-Velocity and Low-Acceleration Regions Based on Encoder Position Data", IEEE/ASME Transactions on Mechatronics, vol. 6 (1), pp. 58-64, March 2001.
- [35] Watton, J., Fluid Power Systems: Modeling, Simulation, Analog and Microcomputer Control, 1st Ed., Prentice-Hall, Troy, NY, Chap. 2, pp. 43, 44., Chap. 3, pp. 102,103, 1989.
- [36] Franklin, G., Powell, J., Emami-Naeini, A., Feedback Control of Dynamic Systems, 3rd Ed. Prentice Hall, December 29, 1997.
- [37] Luenberger, D.G., "Observers for Multivariable Systems," IEEE Transactions on Automatic Control, vol. AC-H (2), pp. 190-197, April 1966.
- [38] Hacksel, P. J., Salcudean, S. E., "Estimation of Environment Forces and Rigid-Body Velocities Using Observers", Proceedings 1994 IEEE International Conference on Robotics and Automation, vol. 2, pp. 931-936, 1994.
- [39] Ohishi, K., Miyazaki, M., Fujita, M., Ogino, Y., "Force Control without Force Sensor Based on Mixed Sensitivity H^∞ Design Method", Proceedings 1992 IEEE International Conference on Robotics And Automation vol. 2, pp. 1356-1361, 1992.
- [40] Ohishi, K., Miyazaki, M., Fujita, M., Ogino, Y., " H^∞ Observer Based Force Control without Force Sensor", Proceedings IECON '91 International Conference on Industrial Electronics, Control and Instrumentation vol. 2, pp. 1049-1054, 1991.
- [41] Ohishi, K., Miyazaki, M., Fujita, M., "Hybrid Control of Force and Position without Force Sensor", Proceedings of the 1992 International Conference on Industrial Electronics, Control, Instrumentation, and Automation. Power Electronics and Motion Control vol. 2, pp. 670-675, 1992.

[42] Ahn, K. K., Yokota, S., “Design of a Robust Force Control System for an Automatic Live-Line Maintenance Robot Using a Force Disturbance Observer”, Proceedings of the Institution of Mechanical Engineers. Part I: Journal of Systems and Control Engineering, vol. 218 (7), pp. 545-556, November 2004.

[43] Katsura, S., Matsumoto, Y., Ohnishi, K., Modeling of Force Sensing and Validation of Disturbance Observer for Force Control”, IEEE Transactions on Industrial Electronics, vol. 54 (1), pp. 530-538, February 2007.

[44] Gulati, N., Barth, Eric J., “Non-linear Pressure Observer Design for Pneumatic Actuators”, IEEE/ASME International Conference on Advanced Intelligent Mechatronics AIM, vol. 1, pp. 783-788, 2005.

[45] Koontz, J.W., Tasch, U., Ignatoski, M. A., Geselowitz, D. B., “An Adaptive Aortic Pressure Observer for the Penn State Electric Ventricular Assist Device”, IEEE Transactions on Biomedical Engineering, vol. 37 (4), pp. 374-383, Apr 1990.

[46] Hahn, J., Hur, J., Cho, Y., Lee, K., “Robust Observer-Based Monitoring of a Hydraulic Actuator in a Vehicle Power Transmission Control System”, Control Engineering Practice, vol. 10 (3), pp. 327-335, 2002.

[47] Kashi, K., Soffker, D., “Model-Based Estimation of Force and Displacement of a Hydraulic Cylinder”, Proc. 7th International Symposium on Advanced Vehicle Control KIVI-NIRIA, Arnheim, Netherlands, 2004.

[48] Soffker, D., Yu, T., Muller, P., “State Estimation of Dynamical Systems with Nonlinearities by Using Proportional-Integral Observer”, International Journal of Systems Science, vol. 26(9), pp. 1571-1582, Sept.1995,

[49] Chang, J.L., “Applying Discrete-Time Proportional Integral Observers for state and Disturbance Estimations”, IEEE Transaction on Automatic Control, vol. 51 (5), pp. 814-817, May 2006.

[50] Smith, C., Tomizuka, M., “Shock Rejection for Repetitive Control Using a Disturbance Observer”, Proceedings of the 35th IEEE Conference on Decision and Control, vol. 3, pp. 2503-2504, 1996.

[51] White, M. T., Tomizuka, M., Smith, C., “Rejection of Disk Drive Vibration and Shock Disturbances with a Disturbance Observer”, Proceedings of the 1999 American Control Conference, vol. 6, pp. 4127-4131, 1999.

[52] Semba, T., "A Disturbance Observer to Suppress Vibration Effects of a HDD in a Disk Array System", Proceedings of the American Control Conference, vol. 2, pp. 1362-1367, 2003.

[53] Kempf, C. J., Kobayashi, S., "Discrete-Time Disturbance Observer Design for Systems with Time Delay", Proceedings 1996 4th International Workshop on Advanced Motion Control, vol. 1, pp 332-337, 1996.

[54] Schrijver, E., van Dijk, J., Nijmeijer, H., "Equivalence of Disturbance Observer Structures for Linear Systems", Proceedings of the 39th IEEE Conference on Decision and Control vol. 5, pp. 4518-4519, 2000.